NASA CONTRACTOR REPORT

NASA CR-1137

SEISMIC EFFECTS OF SONIC BOOMS

by Tom T. Goforth and John A. McDonald

Prepared by
TELEDYNE COMPANY
Garland, Texas
for Langley Research Center

NATIONAL AERONAUTICS AND SPACE ADMINISTRATION • WASHINGTON, D. C. • SEPTEMBER 1968

NASA CR-1137

SEISMIC EFFECTS OF SONIC BOOMS

By Tom T. Goforth and John A. McDonald

Prepared under Contract No. NAS 1-6342 by
TELEDYNE ~~COMPANY~~
Garland, Texas

for Langley Research Center

NATIONAL AERONAUTICS AND SPACE ADMINISTRATION

For sale by the Clearinghouse for Federal Scientific and Technical Information
Springfield, Virginia 22151 – CFSTI price $3.00

ABSTRACT

Earth particle velocities produced by sonic booms were recorded at Edwards Air Force Base, California, the Tonto Forest Seismological Observatory near Payson, Arizona, and the Uinta Basin Seismological Observatory near Vernal, Utah. Analysis of the field data indicates that the seismic effects of sonic booms are largely confined, laterally, to the boom pressure envelope and vertically to the upper few meters of the earth's surface. The maximum particle velocity associated with a sonic boom is in response to the rapid pressure changes of the leading and trailing edges of the acoustic N-wave. Comparison of peak particle velocities recorded at Edwards Air Force Base show good agreement with theoretically-predicted values. Empirical relations developed from the recorded data indicate that peak particle velocity is linearly related to the maximum positive overpressure of the N-wave. On hard, well-consolidated rock, each pound per square foot of overpressure produces about 75 microns per second peak particle velocity. On more loosely-consolidated rock, each pound per square foot of overpressure produces about 100 microns per second peak particle velocity.

CONTENTS

CONTENTS, Continued

ILLUSTRATIONS

ILLUSTRATIONS

ILLUSTRATIONS, Continued

ILLUSTRATIONS, Continued

ILLUSTRATIONS, Continued

ILLUSTRATIONS, Continued

ILLUSTRATIONS, Continued

ILLUSTRATIONS, Continued

TABLES

SEISMIC EFFECTS OF SONIC BOOMS

By Tom T. Goforth and John A. McDonald
Teledyne Industries, Geotech Division

1. INTRODUCTION

This is a report of the experimental and theoretical work accomplished under Contract NAS 1-6342, entered into on 28 June 1966, and Modification 2 to the contract, dated 23 May 1967. The overall period of the contract, including the modification, was from 1 July 1966 to 30 September 1967.

The contract was for a research study of the seismic effects of sonic booms. The objective of the study was to measure and interpret the vibrations of the ground produced by sonic booms.

1.1 SUMMARY OF THE EXPERIMENTS

Field measurements of earth particle velocities produced by sonic booms were made at Edwards Air Force Base (EAFB), California, the Tonto Forest Seismological Observatory (TFSO) located near Payson, Arizona, and the Uinta Basin Seismological Observatory (UBSO) located near Vernal, Utah. Portable seismograph systems were used for the measurements at EAFB. At TFSO and UBSO, modified observatory seismograph systems were utilized in addition to the portable systems. Geologic studies, including seismic refraction surveys, were conducted at each of the three test sites. The particle velocity data were analyzed visually and automatically, and the results were correlated with the geologic data and with NASA-furnished overpressure, flight parameter, and meteorological data. Theoretical estimation techniques were developed to predict maximum particle velocities to be expected for the passage of a known N-wave at a particular geological location.

1.2 GENERATION OF THE SONIC BOOM

Sonic booms are caused by a conical shock wave doublet (N-wave) oriented as shown in figure 1. For simplicity, only the initial compressional shock front is shown. The boom is generated by a sudden compression of air by the bow of the moving aircraft. A rarefaction immediately follows and continues until a final recompression, associated with the tail of the aircraft, concludes the N-wave. Each half of the shock wave doublet produces a relative pressure variation ($\Delta P/P$) at large ray distances R given (Ferri, 1961) approximately for steady, level flight by

$$\frac{\Delta P}{P} = \frac{M^{5/2}}{M^2-1} \frac{F(\xi)}{2R} \tag{1}$$

where $M = \dfrac{\text{speed of aircraft}}{\text{speed of sound in air}}$

and $F(\xi)$ depends upon the size and configuration of the aircraft.

The cone defining the front of the pressure wave doublet intersects a flat earth's surface in a hyperbolic trace. The intersection of each pressure wave with a point on the ground exerts a force on the point directed into the ground at an angle to the vertical equal to the Mach angle (μ). The force may be resolved into vertical and horizontal components shown in figure 1. The horizontal components will couple seismic energy into the ground where the surface is rough or has topographic irregularities. The vertical component of the force creates a hyperbolic arc of elastic depression in the ground, which moves forward with the speed of the aircraft.

This study investigates the resulting seismic effects of this impingement of the boom on the ground.

2. FIELD EXPERIMENTS

2.1 GENERAL

Seismic measurements of sonic booms were made at EAFB, TFSO, and UBSO; the locations of the three test sites are shown in figure 2. The great majority of the measurements were made at EAFB where 183 separate missions were monitored. Measurements were made of 8 missions at TFSO and of 3 missions at UBSO in order to obtain data from different geologic environments and to utilize the seismometer arrays at the observatories for focusing, lateral propagation, and depth attenuation studies.

2.2 INSTRUMENTATION

The mobile equipment consisted of five identical seismograph systems, each of which could be used to measure either horizontal or vertical ground particle velocities. A block diagram of one of the seismograph systems is shown in figure 3. Each seismograph consisted of a Seismometer, Model 18300; an Amplifier and Signal Conditioner, Model 25031; a Visicorder Oscillograph, Honeywell Model 1406; a Magnetic-Tape Recorder, Model 17373; and the associated power supplies and cabling. This equipment provided for the simultaneous recording of seismic data on both paper records and on frequency-modulated magnetic tape. The tape recorder had a greater dynamic range than the visual recorder and was used as the primary recording system, although the paper records provided a useful visual monitor. Also, during analysis of the sonic boom seismograms the paper records provided a useful check on the accuracy of the data played back from the magnetic-tape seismograms.

The magnetic-tape seismograms were recorded on half-inch, 7-channel tape which consisted of 5 channels of seismic data, 1 channel of timing data, and 1 wow-and-flutter compensation channel. The tape speed was 15/16 inches per second. Commonly, 5 channels of seismic data and 1 channel of timing data were recorded on the Visicorder, and intermediate timing lines for the visual records were provided by a built-in timer. The National Bureau of Standards Radio Station, WWV, Fort Collins, Colorado, was recorded on the magnetic tape as a time base.

Calibration of the seismograph systems was accomplished by a Calibration Control, Model 20136. This unit produced a sine wave of known but variable amplitude at a frequency of 5 Hz. The sine wave was used to drive the seismometer coils at known equivalent ground velocities. In general, the seismograph systems were calibrated twice daily on those dates upon which seismic data were recorded.

The velocity response of each seismograph system was flat in the frequency range of 1 to 100 Hz within ±1 dB. Because both the data and calibration signals were transmitted between the recording van and the seismometer over a single four-conductor cable, calibration currents at frequencies above about 30 Hz showed crosstalk between the data and calibration lines.

Therefore, frequency response calibrations were made by injecting the high-frequency calibration currents directly into the system at the seismometer. The frequency response of each seismograph was measured soon after the installation of each seismometer. Also, at least one additional frequency response calibration was made at each location.

Six vertical, short-period seismometers in the TFSO array and three vertical, short-period seismometers in the UBSO array were used for the observatory experiments. These systems were modified to produce an output proportional to ground particle velocities. The systems consisted of Johnson-Matheson Seismometers, Model 6480, feeding Solid-State Amplifiers, Geotech Model 25220. The data were recorded on a 1-inch, 14-channel magnetic tape at a speed of 0.6 inches per second by a Tape Recorder, Minneapolis Honeywell, Model LAR 7460. The frequency responses of the modified seismograph systems were also flat from 1 to 100 Hz.

2.3 DATA ACQUISITION AT EDWARDS AIR FORCE BASE

The major part of the data was collected at EAFB in the period from October 1966 to January 1967. Geotech was one of several contractors of the USAF and of NASA involved in the experiments at EAFB, and the missions were flown, in general, to meet other contractural requirements.

Missions were flown in five general patterns at EAFB:

a. Flights on a 245° magnetic heading over, and at specified off-set distances from, an experimental house designated E2 (see figure 4).

b. Flights over an 8000 ft array of microphones on East Dry Lake (see figure 4). No seismometers were located on this lake bed.

c. Flights over South Base (see figure 4). At times, both a seismometer and pressure gauges were located on this lake bed, providing a lateral separation of between 2 and 3 miles from the location of the other seismometers.

d. Data from more than 30 missions flown by SR-71 aircraft were recorded. These data were used to augment the other sonic boom data whenever adequate flight parameter data were available.

e. Numerous subsonic low level flights producing engine noise rather than sonic booms. These were flown as part of a psycho-physiological study being made by Stanford Research Institute and were recorded at the request of NASA. Some of these data were used in comparisons of ground motions generated by sonic booms and those generated by various forms of cultural noise (see section 4.8).

A complete listing of those flights from which seismic data were recorded at EAFB is given in appendix A.

The locations of the four seismometer positions occupied at EAFB are shown in figure 5 in relation to the most frequently used flight trace over E2. These positions were designated 1, 4, 4R, and 5. Positions 1 and 4 correspond to microphone positions 1 and 31 in a crossed linear array of microphones installed by NASA on the small lake bed to the west of Rogers Dry Lake. Seismometer position 5 corresponds to the most easterly microphone in a small cruciform just to the north of E2. Position 4R was chosen to be remote from the remaining seismometers.

Positions 1 and 5 were the "permanent" seismometer locations at EAFB; a vertical seismometer was located at each position, and data were recorded from them for every mission monitored. Two horizontal seismometers were also located at position 1, one measuring ground particle velocities along the flight path (245°) and the other oriented perpendicular to the flight path. The three seismometers were buried to a depth of about 1 meter in the lake bed material.

The seismometer at position 5 rested on a quartz monzonite basement which at this point was within about 2 meters of the surface.

The seismometer at position 4, position 31 in the lake bed crossed-linear microphone array, measured only vertical particle velocities. It was buried to a depth of about 1 meter in the layer of playa clay over the quartz monzonite basement. This seismometer was moved several times during the experiments and was also used at position 1 and at position 4R.

2.4 DATA ACQUISITION AT THE TONTO FOREST SEISMOLOGICAL OBSERVATORY

Eight missions were flown over TFSO. Seven of the flights were made by B-58 aircraft and one by an SR-71 aircraft.

The B-58 missions were flown specifically for the seismic effects program according to a predetermined pattern. However, ground based radar plotting facilities were not available for verification of flight parameter data; therefore, the pilot's data were used for these flights. Similarly, the observatory and local meteorological station data were used in lieu of Rawindsonde measurements.

The seismometer array used in the experiments at TFSO is shown in figure 6. The five seismometers located at positions 1 through 5 and arranged in a circle were the five seismometers of the mobile system. The data from these seismometers were recorded in the same manner as the data were recorded at EAFB. These data were used to study the focusing effects of the sonic boom hyperbola. All of the portable seismometers were oriented to measure vertical ground particle velocities, and each was buried to a depth of between 0.5 and 1 meter. The overpressure was not measured at these five seismometer locations because only a limited amount of overpressure monitoring equipment was available and overpressure measurements at the other seismometer locations were considered to be more critical.

One of the overflights each day was planned so that some of the seismometers were located inside of the boom envelope and some were located outside of the envelope. Six observatory seismometers, the locations of which were designated 63, 64, 66, 67, 70, and 72, were used in systems having the modified response. Four NASA acoustic recording vans were used to monitor overpressures at locations 63, 64, 66, and 67 on the first day of flights and at locations 63, 64, 67, and 72 on the second day of flights. As shown in figure 6, locations 63, 64, and 72 lay on the flight path for overhead flights on the first day, and locations 64 and 67 lay on the overhead flight path on the second day.

2.5 DATA ACQUISITION AT THE UINTA BASIN SEISMOLOGICAL OBSERVATORY

Three B-58 missions were flown over UBSO. The flight paths of these missions are shown in figure 7. As was the case at TFSO, no ground-based radar data or Rawindsonde weather data were available. These missions were flown for the specific requirements of the seismic effects program.

The locations of the seismometers used in the experiments at UBSO are shown in figure 7.

The mobile equipment used at EAFB and at TFSO was also used at UBSO. Three of the seismometers forming part of the mobile equipment were placed on a concrete pier in a sealed steel vault at a depth of about 15 meters. They were arranged in a three-component system measuring vertical, north-south horizontal, and east-west horizontal ground particle velocities. A Seismometer, Model 18300, in a borehole pressure case was placed on the surface of the ground some 6 meters from the three-component system. This seismometer measured particle velocities at the surface of the ground. The fourth mobile seismometer was placed on a pier at the bottom of a sealed vault 13.4 meters deep measuring vertical particle velocities almost directly below the single vertical seismometer. These locations are designated A and B and are also shown in figure 7.

The other five seismometers were part of the normal observatory instrumentation. Ordinarily, the observatory seismograph systems measure ground displacements rather than ground velocities. The seismometers used were Johnson-Matheson Seismometers, Model 6480, enclosed in sealed steel vaults at the surface; a Model 18300 seismometer in a shallow borehole at a depth of 76 meters; and three Model 11167 deep-hole seismometers at depths of 1190 meters, 1490 meters, and 1790 meters. These locations were designated Z1, SZ1, and DH, respectively (see figure 7).

The seismometers at locations Z1 and SZ1 were used as velocity seismographs, their outputs being proportional to the ground particle velocities. These data were amplified by Solid-State Amplifiers, Model 25220, and were recorded on the tape recorder belonging to the mobile equipment. In the time available, it was not possible to modify the three deep-hole seismographs to have responses identical to the mobile recording equipment and to eliminate 60 Hz noise from these systems (normally, 60 Hz noise is not a problem on these systems because this frequency is outside of the band of interest). Therefore, it was not possible to produce outputs from these seismographs that were proportional to particle velocities with sufficient sensitivity in the range of interest for this program.

2.6 DATA ACQUISITION FOR COMPARATIVE EXPERIMENTS

To compare the magnitudes of the ground motions generated by sonic booms to more familiar "culturally" generated seismic noise, some other examples of culturally-generated seismic noise were recorded. "Cultural noise" in this context means ground motion induced by means other than naturally occurring phenomena (e.g., earthquakes). Typical sources of cultural noise are human activity, motor vehicles, aircraft, heavy construction, etc.

Among the examples of cultural noise that were recorded at EAFB were ground motions caused by a man walking toward a seismometer, an automobile being driven past the seismometer, and the ground motion caused by the operation of aircraft. These seismograms are discussed in section 4.8.

2.7 EFFECT OF PRESSURE VARIATIONS ON THE SEISMOMETER

Extrapolation of unpublished results of tests made by Geotech in 1965 to determine the response of the Model 18300 seismometer to pressure variations indicate that a sonic boom of 2 pounds per square foot overpressure would induce a movement of the seismometer frame of less than 0.4 μ/second at 10 Hz and less than 0.2 μ/second at 100 Hz. This level of pressure-induced velocity is insignificant when compared to the ground velocities observed in this study in the frequency range of 1 to 100 Hz. However, to eliminate this small pressure effect, all seismometers were buried to a depth of at least 1 meter at EAFB and 0.5 meter at TFSO and UBSO. Several tests were conducted at EAFB in which sonic boom pressure changes (N-waves) were simultaneously recorded by a surface microphone and a microphone buried at a depth of 1 meter. The buried microphone showed attenuation of the N-wave by a factor of from 7 to 18 relative to the surface. We conclude that the seismograms produced in this study represent particle velocity of the ground and show no significant effects of the acoustic wave acting directly on the seismometer mass.

3. GEOLOGIC PARAMETERS OF THE TEST AREAS

Data regarding the general geologic environment of each at the test areas were obtained from reports of previous studies made by Geotech (Geotech TR 65-28; TR 66-17), from publications by the United States Geological Survey (Dibblee, 1960; Roller, et al, 1964), and the United States Corps of Engineers (Miscellaneous Paper No. 4-365). In addition, seismic refraction surveys were conducted in each of the test areas to provide information on local near-surface seismic velocities. The geologic information was obtained for the purpose of correlation with the flight parameter and boom-measurement data.

3.1 TOPOGRAPHY, GEOLOGY, AND SEISMIC VELOCITIES

3.1.1 Edwards Air Force Base

Edwards Air Force Base is in the west-central part of the Mojave Desert block about midway between the bounding Garlock and San Andreas faults. It is centered about 110 kilometers east of their junction. This block is cut by numerous high-angle faults, most of which trend north-westward parallel to the San Andreas fault. The rocks in the area can be grouped into three main divisions: granite and metamorphic rocks of pre-Tertiary age; volcanic, pyroclastic, and sedimentary rocks of Tertiary age; and alluvial sediments of Quaternary age.

The topographic features of the area reflect the geologic structure and the relative hardness and coherence of the many different rock strata. Hard, weather-resistant carbonate and chert layers, dike-forming pegmatite-aplite and quartz latite, and quartz basalt crop out as conspicuous ledges, ridges, and hills. The granite in the northwestern quarter of the Rogers Lake quadrangle weathers to low relief, whereas that east of northern Rogers Lake crops out prominently to form steep-sided, jagged hills.

The sediments, chiefly clays, of the dry lake beds in the area were deposited during the Pleistocene age and were derived from the igneous and metamorphic rocks that form the numerous buttes and mountains in the region. Appreciable quantities of windblown sand have accumulated as dunes along the margins of the lake beds. The natural drainage of the Edwards environs flows from all directions towards the Rogers, Buckhorn, and Rosamond Dry Lake lowlands. However, most of the surface flow is absorbed in granular alluvial deposits which form the major portion of the airbase terrain, and only limited drainage reaches the playa lowlands except after heavy storms. There is no surface flow out of the lake bed basins. The lake bed materials are alluvial in origin, and in many instances have been transported considerable distances, their deposition occurring under different environmental conditions. The lake beds are predominately silty clays with many layers of fine, medium, and course sand. The clay content of the lake bed materials ranges from 30 to 80 percent.

The seismic measurements at EAFB were made on a small, shallow, dry lake less than a mile from the western edge of Rogers Dry Lake, and on an adjacent outcrop of quartz monzonite, the same type of rock which underlies the lake beds. The wave propagational velocities of the lake bed and the underlying quartz monzonite were determined by a refraction survey in which twelve geophones were aligned in an approximately northeastern direction across the small lake bed. Dynamite charges were detonated at each end of the geophone line, and arrival times of the compressional wave were recorded by the geophones. Analysis of the refraction data indicates that: (1) the playa clay - quartz monzonite interface is relatively horizontal and averages a depth of 8 to 12 meters below the surface; (2) the average compressional velocity in the clay layer is 600 meters/second; and (3) the average compressional velocity along the top of the quartz monzonite is 2000 meters/second.

3.1.2 Tonto Forest Seismological Observatory

The Tonto Forest Seismological Observatory is located in the Basin and Range Province about 25 kilometers south of the southern boundary of the Colorado Plateau. This boundary is marked by the Mogollon Rim, a 450-meter erosional escarpment of Paleozoic and Mesozoic sediments. Either granite or a thin sedimentary section covers the seismometer array area. The granite is highly decomposed, and weathering extends to a depth of as much as 30 meters. Its decomposed character supports only subdued topography, but numerous granite and diabasic dikes of a more resistant nature support ridges trending in an east-west direction across the array area. The sedimentary section consists of Cambrian and Devonian sandstones and limestones. The maximum thickness of sediments under any seismometer site probably does not exceed 60 meters. Of the 46 seismometer sites, 28 are situated on pre-Cambrian granite, 17 are on a thin veneer of Paleozoic sediments, and 1 is on basalt. Weathered granite probably exists below the sedimentary section in the northern half of the array.

Figure 6 shows the location and code designation of the seismometers of the TFSO array which were utilized in the supersonic flights measurements program, and also the orientation of the refraction survey line. The refraction survey showed a layer with a compressional wave velocity of 1215 meters/second overlying a layer with a compressional wave velocity of 2860 meters/second. The average depth to the interface is 29 meters.

3.1.3 Uinta Basin Seismological Observatory

The Uinta Basin Seismological Observatory is located on the north flank of the Uinta Basin, a broad asymmetrical syncline trending east-west and lying to the south of the Uinta uplift in northeastern Utah. The outcrop within the array area consists of the Duchesne River formation, which is overlain locally by thin Quaternary terrace deposits. The Duchesne River formation consists of fluviatile, friable, cross-bedded sandstones.

Sonic and formation density logs made in several 60-meter holes in the array area show the average compressional velocity along the 60 meters to be 3060 meters/second and the average density to be 2530 kilograms/meter^3 (2.53 grams/cm^3).

Figure 7 shows the location of the seismometers used in the measurements program and the orientation of the refraction survey line. The results of the survey indicate a 6-meter layer of weathered material with a velocity of 660 meters/second overlying sandstone with a velocity of 2500 meters/second.

Figure 8 is a hypothetical cross-section of the Uinta Uplift and Uinta Basin showing the subsurface formations beneath UBSO.

3.2 DETERMINATION OF GEOLOGIC PARAMETERS

The basic technique used in the seismic refraction surveys conducted at each location was to arrange a line of geophones separated by known distances on the surface of the area to be studied. The orientation of the refraction lines with respect to the seismometer positions at EAFB, TFSO, and UBSO are shown in figures 5, 6, and 7, respectively. Data from these geophones were amplified and filtered and were recorded photographically on an oscillograph. A time base was supplied by an interval timing system. An explosive charge was fired at a known distance from one end of the line of geophones, and the instant of detonation and the arrival time of energy at each geophone was recorded. A typical refraction record is shown in figure 9. From the arrival time of the seismic energy at each geophone, the velocity of the compressional wave in the medium can be calculated. In the case of layered media (see figure 10), the higher velocity in the lower layer enables energy traveling in this layer to arrive at the more distant geophones earlier than energy propagated through the surface layer. Plotting arrival times against distance, as in figure 11, resulted in two straight lines, the reciprocal of the slope of each line giving the compressional wave velocity in each layer. Also, from the graph it was possible to make an estimate of the depth of the surface layer.

In addition to the explosive refraction surveys, measurements at each recording position at TFSO were made using a Seismic Timer, Dyna Metric Model 117. The seismic timer is essentially a sledge hammer which starts a timer when it strikes the ground. The timer is shut off when the first burst of seismic energy reaches a geophone located at a known distance from the point of impact. This technique gave a more detailed measure of the near-surface velocity distribution in the immediate vicinity of each seismometer than did the more general explosive surveys. It was desired to obtain the shear as well as the compressional velocities in the refraction surveys, but no accurate method of timing the arrival of the slower-moving shear wave could be devised with the equipment available. Shear wave velocities were estimated on the basis of published values of compressional/shear velocity ratios for various types of rocks. A summary of the refraction results is given in table 1, and the depths at which the seismometers were buried are shown in table 2.

Table 1. Compressional wave velocities and layer depths

A. Edwards Air Force Base - two explosive surveys

West-east profile

Velocity in surface layer	600 meters/second	(1970 ft/second)
Velocity in second layer	2000 meters/second	(6567 ft/second)
Thickness of surface layer (drilling)	10.6 meters	(34.8 ft)
Thickness of surface layer (refraction)	7.8 meters	(25.6 ft)

East-west profile

Velocity in surface layer	532 meters/second	(1740 ft/second)
Velocity in second layer	1986 meters/second	(6515 ft/second)
Thickness of surface layer	6.4 meters	(21 ft)

B. Tonto Forest Seismological Observatory - one explosive survey

Velocity in upper layer	1215 meters/second	(3980 ft/second)
Velocity in second layer	2860 meters/second	(9380 ft/second)
Thickness of surface layer	29 meters	(95 ft)

Hammer surveys

Location 63

Velocity in surface layer	268 meters/second	(910 ft/second)
Velocity in second layer	1001 meters/second	(3300 ft/second)
Thickness of surface layer	1.07 meters	(3.5 ft)

Location 64

Velocity in surface layer	235 meters/second	(770 ft/second)
Velocity in second layer	763 meters/second	(2500 ft/second)
Thickness of surface layer	0.82 meters	(2.7 ft)

Location 66

Velocity in surface layer	235 meters/second	(770 ft/second)
Velocity in second layer	830 meters/second	(2710 ft/second)
Thickness of surface layer	1.46 meters	(4.8 ft)

Table 1. Compressional wave velocies and layer depths, Continued

Location 67

Velocity in surface layer	183 meters/second	(600 ft/second)
Velocity in second layer	548 meters/second	(1800 ft/second)
Velocity in third layer	1020 meters/second	(3340 ft/second)
Thickness of surface layer	0.43 meters	(1.4 ft)
Thickness of second layer	2.92 meters	(9.6 ft)

Location 72

Velocity in surface layer	191 meters/second	(625 ft/second)
Velocity in second layer	731 meters/second	(2400 ft/second)
Thickness of surface layer	1.58 meters	(5.2 ft)

C. Uinta Basin Seismological Observatory - two explosive surveys

Location 1

Velocity in surface layer	660 meters/second	(2000 ft/second)
Velocity in second layer	2500 meters/second	(8440 ft/second)
Thickness of surface layer	6.0 meters	(19.7 ft)

Location 2

Velocity in surface layer	Not determined	
Velocity in second layer	3430 meters/second	(11220 ft/second)
Thickness of surface layer	Not determined	

Table 2. Seismometer depths and site altitudes

A. Seismometer depths (to seismometer bottom)

1. Edwards Air Force Base

Location 1 - three component	1.1 meters (3.6 ft)
Location 1 - pressurized case	0.89 meters (2.92 ft)*
seis	1.37 meters (4.5 ft)
Location 4 - vertical	1.2 meters (4 ft)
Location 4R - vertical	1.1 meters (3.6 ft)
Location 5 - vertical	2.1 meters (6.9 ft)

2. Tonto Forest Seismological Observatory

Location 1 - vertical	0.76 meters (2.5 ft)
Location 2 - vertical	1.07 meters (3.5 ft)
Location 3 - vertical	1.07 meters (3.5 ft)
Location 4 - vertical	0.76 meters (2.5 ft)
Location 5 - vertical	0.91 meters (5.0 ft)
Location 63 - vertical	1.37 meters (4.5 ft)
Location 64 - vertical	1.13 meters (3.7 ft)
Location 66 - vertical	1.52 meters (5.0 ft)
Location 67 - vertical	2.14 meters (7.0 ft)
Location 72 - vertical	1.68 meters (5.5 ft)

3. Uinta Basin Seismological Observatory

Location 1 - three-component	1.2 meters (4 ft)
Location 2 - vertical	13.4 meters (44 ft)
Location Z1	2 meters (6.5 ft)
Location SZ1	76.2 meters (250 ft)
Location DH6	1109 meters (3900 ft)
Location DH5	1495 meters (4900 ft)
Location DH4	1790 meters (5900 ft)

B. Site altitudes above mean sea level (msl)

EAFB	722 meters (2375 ft)
TFSO	1492 meters (4894 ft)
UBSO	1600 meters (5248 ft)

---

*To top of case

4. ANALYSIS AND INTERPRETATION OF EXPERIMENTAL DATA

4.1 GENERAL

Interpretation of the sonic boom field data was focused upon the characteristics of the seismic signature, values of the vertical peak ground particle velocities, and upon the manner in which these parameters vary with flight conditions, geologic location, and weather. In addition, several more specialized problems were considered, including the attenuation of particle velocity with depth, the frequency content of the seismogram, focusing of seismic energy due to the hyperbolic intersection of the shock cone and the ground, and the propagation of seismic energy outside of the sonic boom pressure envelope.

4.2 EXPERIMENTAL DATA PROVIDED BY NASA FOR THE SEISMIC EFFECTS PROGRAM

Geotech was responsible only for the seismic measurements at EAFB, TFSO, and UBSO. Other experimental data which were required for the seismic effects program were collected by various other government agencies and/or contractors of the USAF and NASA. The NASA Langley Research Center (LRC) provided the seismic effects program with the following data for as many missions as possible:

a. Pressure signature, the peak positive and peak negative overpressure, the rise time to the peak positive overpressure, and the period of the N-wave;

b. Aircraft speed, heading, altitude;

c. Meteorological data.

In addition, USAF personnel from EAFB surveyed the seismometer locations at EAFB.

4.3 METHODS OF MEASUREMENT AND CLASSIFICATION OF SEISMOGRAMS

A hypothetical seismogram is shown in figure 12. It is a representation of the ground particle velocity at a point which is subjected to the "typical" N-wave, and is typical of the seismic waveforms observed. The various characteristics of the seismogram which were measured in this study are identified in this figure. These measurements and all available related pressure and radar data pertaining to each flight were coded on punched cards, and the empirical relationships between the various parameters were obtained by machine processing.

It was possible to categorize the bow and stern halves of each seismogram into 1 of 10 groups in a manner similar to that used by NASA LRC for the pressure N-wave data. Examples of the wave shapes in each seismic classification are shown in figure 13. Correlation of the seismic and pressure classifications produced no consistent relationships. That is, a particular class of N-wave does not produce a particular class of seismic waveform. However, the seismic classification can be correlated with seismometer location.

Positions 1 and 4 on the lake bed at EAFB produce class 1 waveforms, and position 5 on the quartz monzonite outcrop usually produces class 2 waveforms.

4.4 SEISMOGRAM CHARACTERISTICS

Over 1000 individual seismograms were recorded at 20 different sites. Although the seismic signatures varied considerably from site to site, and to a lesser extent from mission to mission, all of the records possessed some characteristics in common.

Each seismogram recorded under the sonic boom pressure envelope is characterized by two relatively large downward particle velocities, which are caused by the rapid pressure changes associated with the leading and trailing edges of the N-wave. In almost every case, these downward peaks on the vertical component constitute the maximum particle velocities observed at a location for a given overflight. The time interval between these maximum trace excursions is equal to the period of the N-wave, which in turn varies primarily with aircraft type, altitude, and speed.

Figure 14 is a seismogram recorded on a well-consolidated rock outcrop (position 5, figure 5) at EAFB. It is representative of a large number of seismograms which are almost devoid of features other than the two large downward peaks. Other seismograms, especially those recorded on the dry lake bed at EAFB, have oscillations of several different frequencies following each maximum.

Figure 15 is a vertical seismogram recorded on the lake bed showing 80 Hz sinusoidal oscillations following each of the large downward peaks. Figure 16 was recorded at a different position on the lake bed and shows 9 Hz oscillations and 80 Hz oscillations following the peaks. Seismograms recorded at TFSO and UBSO also vary with location, as shown in figure 17, but they tend to resemble the seismograms recorded on the well-consolidated rock (position 5) at EAFB in that they are characterized by the bow and stern peaks and show little addition of sinusoidal oscillations.

Figure 18 is a high-sensitivity velocity seismogram in which it is possible to see a precursor to the maximum velocities. The particle velocity associated with the precursor is commonly 5-10 μ/second, which is only a fraction of the maximum velocity, and which cannot be seen on seismograms recorded at an operational sensitivity at which the maximum particle velocity did not exceed the dynamic range of the recording system. Nevertheless, the precursor, which is a wave propagated from a previous location of the pressure disturbance, is apparently always present where the compressional velocity of the ground is greater than the aircraft speed.

The horizontal components of particle motion usually exhibit a maximum velocity a few cycles after the initial movement. Figure 19 is a typical three-component seismogram recorded on the lake bed. The radial component commonly shows greater particle velocity than the transverse but less than the vertical.

4.5 EFFECTS OF FLIGHT CONDITIONS, GEOLOGICAL LOCATION, AND WEATHER ON THE SEISMIC SIGNATURE AND ON PEAK PARTICLE VELOCITIES

4.5.1 Effect of Seismometer Location on the Seismic Signature

The particular location of the seismometer has an important effect on the seismic signature, as can be seen in figure 20, in which very similar N-waves produce distinctively different seismic waveforms at each of five locations. This effect is primarily due to the variation of the elastic parameters of the earth, mainly the shear wave velocity and the near-surface layering of the rock or soil in the immediate vicinity of the seismometer. The local nature of the seismometer location effect can be seen by noting the difference between the seismograms shown in figures 15 and 16, both of which were recorded on the dry lake bed at EAFB but at locations about 250 meters apart. An explanation for the particular variations of seismic waveforms observed at EAFB is given in sections 5.2 and 5.3.

4.5.2 Effect of Aircraft Type on the Seismic Signature

The effect of aircraft size and configuration on the seismic signature is indirect in that the aircraft geometry affects the N-wave characteristics, which in turn influence the particle velocity signature. Figure 21 shows vertical velocity seismograms produced by N-waves generated by four different types of aircraft - F-104, B-58, XB-70, and SR-71. These seismograms were recorded on a well-consolidated rock outcrop (position 5) at EAFB. Figure 22 shows seismograms for the same four types of aircraft, recorded on the lake bed (position 1) at EAFB. The primary difference between the seismograms at a given location is the time interval between the maxima, which corresponds directly to the different periods of the N-waves.

4.5.3 Effect of Seismometer Location and Aircraft Type on Peak Particle Velocity

Figures 23 through 41 show the empirical relationship between peak positive overpressure and peak ground particle velocity as a function of aircraft type and seismometer locations. The lines drawn through the data points are constrained to pass through the origin, and they minimize the sum of the squares of the perpendicular distances from the points to the line. If the variance of the acoustical measurements is about the same as the variance of the seismic measurements, the lines are the maximum likelihood estimators.

Several conclusions may be drawn from these relations:

a. Reference to the geologies of the EAFB seismometer locations given in table 1 indicates that a given maximum positive overpressure produces greater maximum particle velocities for locations on loosely-consolidated, low-velocity material than on hard, higher-velocity material.

b. The peak particle velocity appears to be linearly related to maximum overpressure. Each pound per square foot of overpressure produces about 100 μ/second peak particle velocity on loosely-consolidated rock and about 75 μ/second on well-consolidated rock.

c. For a given maximum overpressure, the aircraft type is not significant in determining the maximum particle velocity.

d. For a given overpressure, maximum particle velocities in a direction radial to the flight track of the aircraft are less than those in a vertical direction and greater than those in a direction transverse to the flight track.

Too few flights were made at TFSO and UBSO to estimate the true overpressure - particle velocity relationship. However, figures 40 and 41 give the empirical relationship for the flights available. The lines drawn through these points have little statistical significance because of the small number of data points upon which they are based.

4.5.4 Effect of Aircraft Altitude on Peak Particle Velocity

Maximum particle velocity is a function of aircraft altitude only through the relationship of altitude to maximum overpressure. That is, for a given overpressure, the maximum particle velocity is independent of the aircraft altitude. However, the indirect relationship of maximum particle velocity to aircraft altitude is of some interest and is given in figure 42 for the F-104 and B-58. The data points show considerable scatter, and no extrapolation beyond the altitude range of the observed data should be attempted. The relationship of altitude to peak particle velocity for the XB-70 is not given because the XB-70 flew at only two altitudes during the tests (~37,000 feet and ~60,000 feet). It might be noted, however, that the XB-70 at 60,000 feet produced about the same peak particle velocity as a B-58 at 40,000 feet and an F-104 at 20,000 feet.

4.5.5 Effect of Aircraft Speed on Peak Particle Velocity

No relationship could be observed between aircraft velocity in the supersonic range and peak particle velocities. Theoretically, the overpressure should be affected very little by changes in the aircraft speed above Mach 1.3, and since peak particle velocities are seen to vary with overpressure, no relationship should be expected. Aircraft velocity was important, however, in certain cases where there was a matching with the seismic velocity of Rayleigh waves. This phenomenon will be discussed in section 5, although it might be noted here that in no case did velocity-coupled Rayleigh waves constitute the maximum particle velocity of a seismogram.

4.5.6 Effect of Meteorological Conditions on Peak Particle Velocity

Variations in temperature, relative humidity, and wind velocity were not observed to affect the maximum particle velocity directly, although the effect of such variations on the overpressure was reflected in ground velocity.

4.6 FOCUSING

Because the sonic boom shock cone intersects the ground in a hyperbolic arc, and because seismic waves would be expected to travel backward from the source arc, as well as forward, there exists the possibility of seismic waves arriving in phase from the two arms of the hyperbolic source with a resultant reinforcement of seismic energy. One of the objectives of the seismic experiments at TFSO was to evaluate possible focusing effects. Five seismometers numbered 1-5 and arranged in a circle of 1 km radius, as shown in figure 6, were utilized for this purpose. The aircraft flew as nearly over the center of the circle as possible with the idea that the traveling focus, if it exists, would pass through the circle and be recorded by one or more of the seismometers. No evidence of focusing was obtained from this experiment. It seems likely that inhomogeneities in the ground make it impossible for seismic waves to travel several kilometers over different paths and arrive exactly in phase. Also, as noted in section 4.4, the particle velocities associated with propagating waves such as the precursor are only a few microns per second and even a doubling of this particle velocity, which focusing could theoretically produce, would be insignificant when compared to the particle velocities associated with direct passage of the N-wave.

4.7 ATTENUATION OF GROUND PARTICLE VELOCITY WITH DEPTH

The primary purpose of the overflights at UBSO was to study the attenuation of the sonic boom induced ground motion with depth. As was explained in section 2.5, it proved to be impossible to record ground velocity data from the three seismometers in the deep well, largely because of the high amplitude 60 Hz noise present in the area.

It was possible to record some low quality data from a Seismometer, Model 18300, which was placed on a concrete pier in a sealed steel vault at a depth of 13.4 meters (44 feet). This seismometer was almost directly beneath a similar seismometer in a pressurized case which was placed at the ground surface. The comparative seismograms produced by each seismometer for mission Uinta 3 are shown in figure 43. There was an attenuation of the peak particle velocity by a factor of about 75 at a depth of 13.4 meters, relative to the surface. The seismic effects of the sonic boom are apparently near-surface phenomena.

4.8 COMPARISON OF SEISMOGRAMS RESULTING FROM CULTURALLY-PRODUCED NOISE AND SEISMOGRAMS RESULTING FROM SONIC BOOMS

It is of some interest to compare the velocities and frequencies of boom-induced ground motion to the velocities and frequencies associated with ground motion due to various types of cultural noise.

Seismograms of noise produced by five different cultural sources were recorded at EAFB. These were the passage of an automobile, a man walking, an XB-70 taking off, an F-104 in "touch-and-go" operations, and a low-flying, subsonic F-111 aircraft.

Figure 44 shows the maximum particle velocity and the associated frequency observed for each source type. Analogous information for several sonic booms is included for comparison. Figures 45 and 46 show seismograms recorded for two non-boom sources.

The maximum particle velocities associated with sonic booms are several times larger than those of any of the non-boom sources monitored. However, had the non-boom disturbances been recorded closer to their source, they would have probably produced greater particle velocities than did the sonic booms.

In general, the sonic booms produced seismograms with more energy concentrated at the lower frequencies than did the non-boom sources, although in no case did the maximum particle velocity of the sonic boom seismogram occur at these low frequencies.

4.9 FREQUENCY SPECTRA OF VELOCITY SEISMOGRAMS

The power spectra of velocity seismograms recorded at several different locations for various types of aircraft and flight conditions were digitally computed.

The samples were digitized at a rate of 1000 samples per second, which gave adequate resolution of the high frequencies. All dc offsets were removed from the digitized data, and the seismograms were normalized to the maximum. Each seismogram was digitally represented by 3050 samples, or just over 3 seconds.

The smoothed spectral estimates of the seismograms were produced using a CDC 3100 computer. The technique was based on the method of Blackman and Tukey (1958).

Figures 47, 48, and 49 show the amplitude power spectra of seismograms recorded at the same location (position 4) at EAFB for different shaped N-waves. Each of the three spectra show predominant peaks at about 80 Hz, a frequency which is characteristic of seismograms recorded at position 4, even though there is relatively little power in any of the N-wave spectra at that frequency.

Figures 50, 51, and 52 show the great variation of the power spectra with geology for the same pressure input.

The seismic spectra depend both on the shape of the N-wave and the response characteristics of the ground with the latter apparently having the greater influence.

4.10 PROPAGATION OF SEISMIC ENERGY OUTSIDE THE BOOM PRESSURE ENVELOPE

Two flights (Tonto 3 and Tonto 7) at TFSO were made at lateral distances of 20 miles from the seismic detectors. These flights were made by B-58's flying at Mach 1.65 at about 48,000 feet. The maximum particle velocity recorded for the flights was 9 microns per second. This is about 1/6 the maximum particle velocities observed at the same locations for a B-58 flying approximately overhead at the same altitude and speed (Tonto 1). On this basis, it appears that significant seismic energy will not propagate outside the boom pressure envelope.

4.11 COMPARISON OF MAXIMUM PARTICLE VELOCITIES WITH DAMAGE CRITERIA

The earth particle velocities measured in this study were found to be approximately linearly related to overpressure. The maximum particle velocities measured, which did not exceed 600 μ/second, were in response to overpressures of between 5 and 6 lb/ft^2. Although it is not the purpose of this study to determine whether measured particle velocities are potentially damaging, it is interesting to compare the value of 600 μ/second with currently acceptable damage criteria.

It is the recommendation of the United States Bureau of Mines (W. I. Duvall and D. E. Fogelson, 1962; and personal communication with W. I. Duvall, 1967) that vibration levels in the vicinity of residential structures should be maintained below a peak particle velocity of 2 inches per second (50,800 μ/second). On this basis, the maximum particle velocities observed in this study, which were in response to large overpressures acting on relatively loose material (lake bed), reached about 1.2 percent of the damage threshold.

Several states and agencies have adopted slightly different damage criteria, some of which are based on the "energy ratio," a concept conceived by F. J. Crandell (Crandell, 1949). Crandell defined the energy ratio as the acceleration squared, divided by the frequency squared, where the acceleration is expressed in units of feet per second squared and the frequency in units of hertz. Energy ratios below 3, which is equivalent to a particle velocity of 76,200 μ/second, were considered safe by Crandell. The states of New Jersey and Massachusetts have specified an energy ratio of 1 (48,514 μ/second) as the allowable limit. A damage criterion based on an energy ratio of 1 was also specified by the U. S. Corps of Engineers and the New York State Power Authority. The peak particle velocities observed in this study were well below all these levels.

5. THEORETICAL STUDIES

5.1 GENERAL

In addition to providing information for the empirical relationships between flight parameters and particle velocities, a primary purpose of the seismic monitoring program at EAFB was to provide a physical explanation for the observed seismic signatures and to develop a method to determine the maximum particle velocities to be expected from a given N-wave at a particular geological location.

As discussed previously, the great majority of the seismograms recorded at EAFB were made at two separate positions on the clay lake-bed and at a position on a quartz monzonite outcrop. The sonic boom seismic signature was found to depend strongly on the location at which it was recorded. Figure 53 shows that each of the three locations furnish distinctive waveforms for the same flight. The two predominant downward particle velocities which almost entirely constitute the rather simple seismogram recorded on the well-consolidated quartz monzonite outcrop (figure 53a) are due to the vertical forces exerted by the two compressions of the N-wave. These downward peaks may be considered to be an elastic deformation of the surface of the ground due to the locally-applied pressure load rather than to a seismically-propagated wave, since the motion was detected almost at the point of application of the force and almost simultaneous with the application of the force. The two peak-downward particle velocities also dominate the seismograms recorded at positions 1 and 4 (figures 53b and 53c) on the dry lake-bed, but recordings made at these positions present a more complicated signature. Data recorded at position 1 consistently exhibit the superposition of a high-frequency (~80 Hz) oscillation, and data recorded at position 4 show the addition of this high frequency plus a lower frequency (5 to 10 Hz).

Section 5.2 offers an explanation of the presence of these sinusoidal oscillations,and a theoretical technique for the estimation of the peak particle velocities is presented in section 5.3.

5.2 VELOCITY COUPLING

It has been shown (Press and Oliver, 1956; Press and Ewing, 1951a and 1951b) that velocity-coupled Rayleigh waves can and often do exist in a layered earth after an explosion in the air. This type of wave results from the coupling of energy into the earth from the air wave propagating outward from the point of explosion. It has been observed only when the phase velocity of the dispersive Rayleigh wave is equal at some frequency, to the velocity of sound in air. Since Rayleigh waves in a layered medium can exist over a range of velocity values, the condition for resonant coupling is not too difficult to satisfy. When this condition is met, the resulting seismic wave will have a phase velocity equal to the velocity of the traveling disturbance, regardless of whether the disturbance is an air wave moving at the speed of sound or is an N-wave moving at supersonic speed. The coupled wave will have a constant frequency equal to that frequency at which the dispersive wave travels with the velocity of the traveling disturbance. Some of the seismograms, especially those recorded at position 4 on the dry lake bed (e.g., figure 16), show damped sinusoidal oscillations of two distinct frequencies (~78 Hz and ~9 Hz in this particular instance) following each of the two large downward pulses. These frequencies, although constant for a particular seismogram, were observed to vary for missions involving different aircraft speed. Particle motion analysis from a three-component seismograph system indicates that the motion for the lower frequency sinusoid is retrograde elliptical - a Rayleigh wave. Particle motion analyses for the higher frequency sinusoid are inconclusive. The observed frequencies were plotted against the aircraft ground speed, which is equal to the speed of the traveling pressure disturbance, in an effort to substantiate the hypothesis that energy in this frequency range is velocity-coupled Rayleigh energy. This was done for seismograms recorded at position 4 on the lake bed. By utilizing the compressional wave velocity determined from the refraction survey conducted at EAFB, and estimating the value of Poisson's ratio as 0.4, which is a reasonable but critical assumption, the theoretical Rayleigh wave dispersion curve for the lake bed was computed. This relation gives phase velocity as a function of frequency (or period) for Rayleigh waves traveling through the idealized dry lake model. Figure 54 shows good agreement between the superposed plots of the aircraft velocity - observed period curves for position 4 and the theoretical fundamental mode Rayleigh dispersion curve. Figure 54 also shows that the observed higher-frequency sinusoids lie along the theoretically-predicted curve for a higher-mode Rayleigh wave, and indicates that the high-frequency oscillations could be a velocity-coupled, higher-mode Rayleigh wave. However, this interpretation is considered to be questionable because of the absence of oscillations corresponding to intermediate modes, such as the first higher mode. An alternative suggestion is that these oscillations result from constructively interfering reflections of compressional waves between the free surface and the clay-quartz monzonite interface. It has been shown (Gupta, 1966) that compressional waves normally incident on a one-layer model will result in maximum amplitudes for frequencies of:

$$f = \frac{(2m-1)V}{4H}$$

where V = compressional velocity in the layer

H = thickness of the layer

m = 1, 2, 3 ....

On this basis,

$$H = \frac{(2m-1)\ 600\ \text{m/sec}}{4 \times 78\ \text{Hz}}$$

and $m = 1$ $H = 2$ meters
$m = 2$ $H = 6$ meters
$m = 3$ $H = 10$ meters
$m = 4$ $H = 14$ meters
$\vdots$ $\vdots$

That is, the oscillations at a frequency of about 80 Hz could be explained by the presence of a pronounced velocity discontinuity (layer boundary) at a depth of any of the values of H. The refraction survey indicates that a velocity discontinuity is present at a depth of 10 meters, corresponding to $m = 3$. Thus, the clay-quartz monzonite boundary could account for the 80 Hz oscillations.

Although the gross geological features of positions 1 and 4 are almost identical, the seismograms recorded at position 1 show a much poorer development of the coupled Rayleigh wave than is seen at position 4. The difference in the seismograms recorded at the two lake-bed positions indicates that the velocity coupling is a local phenomenon, and apparently the variability of the thin layers in the clay around position 1 is sufficient to inhibit the formation of well-defined coupled waves. Figure 14 shows the poor development of velocity-coupled waves at position 5 on a quartz monzonite outcrop. The seismometer was positioned on unweathered rock, although it was covered by weathered material. The compressional velocity of the unweathered quartz monzonite where it underlies the lake bed is approximately 2000 meters/second (~Mach 5.5), which is too high for efficient velocity coupling. None of the recording positions occupied at TFSO and UBSO show evidence of velocity coupling. The refraction surveys and well velocity logs show the average velocities of the near-surface rock to be too high for coupling to exist from the flights made over these locations.

5.3 PREDICTION OF SEISMOGRAMS AND MAXIMUM PARTICLE VELOCITIES

5.3.1 Discussion

It can be seen from the examples of seismograms shown that the maximum velocities of the sonic boom seismic signature are not associated with the energy contained in the velocity-coupled waves or with the energy attributed to the reflected compressional waves. The maximum velocities were the two pronounced downward velocities which result from the direct passage of the leading and trailing edges of the N-wave.

This section will show that an elastostatic approximation of the action of an N-wave pressure distribution on an idealized model of the lake bed can account for these two pronounced downward motions and the general overall shape of the seismic signature.

5.3.2 Assumptions

It will be assumed that at EAFB, the lake bed area in the vicinity of the seismometer is a homogeneous, elastic half-space. This idealizes the physical situation to an extent that is, in general, invalid for geologic environments; however, the unusual nature of the dry lake bed at least approximately fulfills the assumptions for the following reasons:

a. The surface of the lake bed, covering over 300,000 square meters, has essentially no relief;

b. The lake bed material, although composed of both sand and clay particles, appears to be relative homogeneous to the depth of burial of the seismometers in the sense of uniformity of compaction and absence of layering.

5.3.3 Deformation of a Half-Space

Boussinesq (1885) has given a solution for the state of deformation present in an elastic half-space whose plane boundary, described by the x_1-x_2 plane, is under the action of a concentrated normal force, the direction of the force being in the positive (downward) x_3 direction. Love (1927) expanded the solution to include the action of a distributed normal load.

The procedure for determining the deformation of a half-space by a concentrated force and ultimately a distributed pressure load may be summarized as follows:[1]

a. The equations of equilibrium and the stress-strain relations for a homogeneous, isotropic, elastic solid are expressed in terms of displacements. The result is a system of differential equations known as Navier's equations.

b. Kelvin (1848) gives a particular solution to Navier's equations for the conditions of a concentrated force acting downward at the origin along the x_3-axis within an elastic solid. The normal stresses for this solution are seen to vanish everywhere on the plane $x_3=0$ except at the origin; the shear stresses do not vanish upon this plane.

c. Kelvin's solution can be used in conjunction with the principle of superposition to obtain another solution. The stress distribution in the body is determined for a center of compression (equal and opposite forces acting along the three coordinate directions) at the origin. It is then assumed that centers of compression are located all along the negative x_3-axis, and the stress distribution for this condition is determined by integrating the result for single centers along the x_3-axis from 0 to $-\infty$. It is found for this solution also that the normal stresses vanish in the plane $x_3=0$, except for a concentrated force at the origin, and that the shear stresses do not vanish on this plane.

---

[1] See appendix B for the complete derivation

d. By combining the two solutions with a suitable adjustment of the two constants involved, it is possible to obtain a stress distribution such that the plane $x_3=0$ is free from both shear and normal stresses and a concentrated force acts on the origin. These are the conditions for a concentrated force acting on a half-space.

e. The solution for the concentrated force can be generalized to yield displacements produced by a suitably restricted continuous distribution of normal loads, giving

$$u_1 = \frac{x_3 x_1}{4\pi\mu} \iint_{-\infty}^{\infty} \frac{p(\xi,\eta)\,d\xi d\eta}{r^3} - \frac{x_1}{4\pi(\lambda+\mu)} \iint_{-\infty}^{\infty} \frac{p(\xi,\eta)\,d\xi d\eta}{r(r+x_3)}$$

$$u_2 = \frac{x_3 x_2}{4\pi\mu} \iint_{-\infty}^{\infty} \frac{p(\xi,\eta)\,d\xi d\eta}{r^3} - \frac{x_2}{4\pi(\lambda+\mu)} \iint_{-\infty}^{\infty} \frac{p(\xi,\eta)\,d\xi d\eta}{r(r+x_3)} \qquad (2)$$

$$u_3 = \frac{x_3^2}{4\pi\mu} \iint_{-\infty}^{\infty} \frac{p(\xi,\eta)\,d\xi d\eta}{r^3} + \frac{\lambda+2\mu}{4\pi\mu(\lambda+\mu)} \iint_{-\infty}^{+\infty} \frac{p(\xi,\eta)\,d\xi d\eta}{r}$$

where	u_1, u_2, u_3	are the displacements in the x_1, x_2, x_3 directions, respectively
	$p(\xi,\eta)$	is the distributed normal load acting at the point (ξ,η) of the $x_3=0$ plane
	x_1, x_2, x_3	is the point at which the displacements are computed
	λ, μ	are the Lame' elastic constants

and

$$r = (x_1-\xi)^2 + (x_2 - \eta)^2 + x_3^2$$

These integrals are difficult to evaluate unless the nature of the load $p(\xi,\eta)$and the area over which it acts are simplified. A discrete approximation of the spatial distribution of the N-wave at a given instant of time was substituted for the continuous load, $p(\xi,\eta)$. Each N-wave was considered to have a straight leading edge (rather than a hyperbolic edge) because only the portion of the load within a few hundred feet of a given point contributes significantly to the displacement at that point. Over this small a distance, the curvature of the wave front is insignificant. Utilizing information supplied from pressure measurements of N-wave rise times, wave lengths, and maximum overpressures, N-waves for selected flights were modeled as aggregates of discrete forces per each square meter, and equations (2) were considered as summations over all square meters of the loaded area. Equations (2) are then written:

$$
\begin{aligned}
u_1 &= \frac{x_1 x_3}{4\pi\mu} \sum_{\xi} \sum_{\eta} \frac{p(\xi,\eta)}{r^3} - \frac{x_1}{4\pi(\lambda+\mu)} \sum_{\xi} \sum_{\eta} \frac{p(\xi,\eta)}{r(r+x_3)} \\
u_2 &= \frac{x_2 x_3}{4\pi\mu} \sum_{\xi} \sum_{\eta} \frac{p(\xi,\eta)}{r^3} - \frac{x_2}{4\pi(\lambda+\mu)} \sum_{\xi} \sum_{\eta} \frac{p(\xi,\eta)}{r(r+x_3)} \qquad (3) \\
u_3 &= \frac{x_3^2}{4\pi\mu} \sum_{\xi} \sum_{\eta} \frac{p(\xi,\eta)}{r^3} + \left(\frac{\lambda+2\mu}{4\pi\mu(\lambda+\mu)}\right) \sum_{\xi} \sum_{\eta} \frac{p(\xi,\eta)}{r}
\end{aligned}
$$

where $p(\xi,\eta)$ is the discrete load on a square meter, the center of which is at (ξ,η). The displacements were determined as a discrete function of time by allowing the modeled N-wave to assume varying positions relative to the observation point, the positions being based on the aircraft speed and direction supplied from radar tracking data. These functions were numerically differentiated to give theoretical velocity seismograms.

6. COMPARISON OF FIELD RECORDINGS AND THEORETICALLY-PREDICTED VALUES

Ten missions were selected for comparison of the seismograms recorded at EAFB and TFSO with theoretical seismograms computed from the geologic models and the characteristics of recorded N-waves. The ten missions used were selected because they represent several different types of aircraft and a wide range of maximum overpressures.

Table 3 gives the pertinent information for the missions considered. Figure 55 shows that the observed and theoretically predicted (usually maximum) velocities for each of the missions selected agree well with each other. Figures 56 through 64 show the observed seismograms superposed on theoretically predicted seismograms for a vertical seismograph located on the lake bed for 9 of the 10 missions. The basic seismic signature is well described by the theory, although many secondary features including the air-coupled waves and reflections are not. The theoretical results are valid for the lake bed positions (1 and 4). To test the value of the theoretical predictions for a geological environment which does not satisfy the conditions of a half-space as well as the lake bed, a theoretical seismogram was calculated for mission TONTO 2 at seismometer position Z-67 at the Tonto Forest Observatory. Table 1 shows the Z-67 environs to be layered. A thin layer (0.43 meters) with velocity 183 meters/second overlies a second layer (2.92 meters thick) with velocity 548 meters/second. The seismometer was buried to a depth of 2.1 meters, near the middle of the second layer. The velocity in the second layer was used in modeling the properties of the half-space. Figure 65 shows the comparison of the theoretical and observed seismograms obtained for mission TONTO 2 at position Z-67 at the Tonto Forest Observatory. Surprisingly close agreement is seen between the theoretical and observed maximum velocities, although correspondence between the wave forms of the two velocity seismograms is not as good as the correspondence between theoretical and observed seismograms from the lake bed at EAFB.

Table 3. Data for missions used in comparison of theoretical and observed seismograms

AIRCRAFT							GEOLOGY			
Mission	Type	Mach	Altitude (K ft)	Max. over-pressure (lb/ft^2)	Period of N-wave (sec)	Rise time of N-wave (sec)	Seismometer depth (m)	Compressional velocity (m/sec)	Estimated shear velocity (m/sec)	Density (Gm/cm^3)
1-1	XB-70	1.5	37.2	2.61	.224	.002	1.1	600	245	2.00
75-1	F-104	1.5	49.6	.92	.103	.008	1.1	600	245	2.00
86-1	B-58	1.64	36.1	1.86	.159	.007	1.1	600	245	2.00
85-1	B-58	1.63	36.0	2.22	.161	.007	1.1	600	245	2.00
117-1	F-104	1.65	26.4	1.48	.075	.002	1.1	600	245	2.00
79-1	F-104	1.5	50.4	.49	.112	.008	1.1	600	245	2.00
122-1	B-58	1.65	48.6	1.20	.182	.009	1.1	600	245	2.00
117-2	B-58	1.65	48.0	1.48	.194	.007	1.1	600	245	2.00
61-1	F-104	1.65	29.6	1.25	.077	.002	1.1	600	245	2.00
Tonto 2	B-58	1.65	48.0	1.08	.176	.020	2.1	548	293	2.00

7. CONCLUSIONS

We conclude the following from the results of this study:

a. The maximum ground particle velocity produced by a sonic boom is linearly related to the maximum overpressure of the boom, in the range of overpressures between 0.5 and 5.0 pounds per square foot. Experimental results indicate that each pound per square foot of overpressure produces about 100 μ/sec peak particle velocity on low-density rock and about 75 μ/sec on high-density rock.

b. A theoretical estimation technique based on the elastostatic deformation of a half space gives good agreement with experimental results for the peak particle velocities resulting from a given N-wave acting on a particular geology.

c. The damage potential of the peak particle velocities produced by sonic booms is well below the damage thresholds accepted by the United States Bureau of Mines and other agencies.

d. Peak particle velocities recorded on the lateral edge of the sonic boom pressure envelope are attenuated by a factor of about 6 relative to peak particle velocities observed under the aircraft.

e. Focusing of seismic energy due to backward propagation from the hyperbolic intersection of the shock cone and the ground was not observed.

f. Peak particle velocities recorded at a depth of 44 feet were attenuated by a factor of 75 relative to those recorded at the surface.

g. Good evidence for the existence of velocity-coupled Rayleigh waves was found for one recording station. These waves did not produce the maximum particle velocity associated with the boom. The lateral uniformity of near-surface layering and velocity distribution necessary for such waves to build up sufficiently to constitute a menace to structures seems unlikely.

8. RECOMMENDATIONS

8.1 Theoretical results indicate that the peak particle velocity is not only linearly related to maximum overpressure, but is also related, in a more complicated manner, to the N-wave rise time and wave length. No quantitative investigation of the effect of these parameters was made in this study, but some preliminary results indicate that a decrease in rise time, for a given maximum overpressure, might significantly reduce the peak particle velocity, although not necessarily reducing the maximum displacement. Because the damage potential of vibrations is more closely related to particle velocity than to displacement further investigation of the roles of N-wave rise time and N-wave period in peak particle velocity might be worthwhile.

8.2 Theoretical results indicate that knowledge of the seismic shear wave velocity, as well as the seismic compressional wave velocity, is needed for accurate theoretical predictions of maximum particle velocities. Although reasonable estimates of the seismic shear velocity can be made through knowledge of the compressional velocities used in conjunction with published values of compressional/shear velocity ratios obtained by laboratory studies of various materials, as was done in this study, the theoretical estimation technique developed should ideally be verified by using experimentally-determined values of in situ shear velocities. The measurement of shear velocities presents a serious problem because previously-arriving compressional waves disturb the record; however, recent investigations (Whitcomb, 1966) indicate promise for a method utilizing angular accelerometers as transducers. The application of such a technique and the use of measured shear velocities should be utilized to rigorously determine the accuracy of the estimation technique over a wide range of shear velocities.

8.3 Peak particle velocities produced by sonic booms depend greatly on geologic conditions in the immediate vicinity of the point of observation. It would therefore be valuable to build a catalog of seismic measurements of sonic booms for a wide variety of local environments. If a shear velocity measurement technique could be developed, and the accuracy of the theoretical estimation technique verified, as recommended in section 8.2, the catalog of sonic boom measurements could be replaced by a catalog of equally-valuable but much more easily-obtained shear velocity measurements. Catalogs of these types should be valuable in estimating ground motions resulting from N-waves "after-the-fact" (for example, substantiating or repudiating structural damage claims related to sonic boom induced seismic energy).

9. ACKNOWLEDGEMENTS

We are indebted to the Air Force Technical Applications Center, VELA Seismological Center, for the use of the facilities at the Tonto Forest Seismological Observatory and the Uinta Basin Seismological Observatory. United States Air Force personnel prepared the seismometer sites and locations at Edwards Air Force Base. A. C. Morgan and H. K. King made the field recordings. The NASA LRC provided pressure, radar, and meteorological data. George Gerlach provided valuable advice and assistance throughout the study and edited the final manuscript. John Cook was instrumental in the original concept, in defining the scope of the project, and in providing advice throughout the program. Martin Robinson provided valuable assistance in solving various instrumentation problems.

APPENDIX A

MISSIONS MONITORED IN THE SEISMIC EFFECTS STUDY

DATE	MISSION	AIRCRAFT	MACH NO.	ALTITUDE
31 OCT 66	17-1	F104	1.6	31.
	17-2	B58	1.61	48.6
	18-1	B58	1.57	47.3
	18-2	F104	1.61	31.0
	19-1	F104	1.64	30.5
	19-2	B58	1.46	38.9
	20-1	B58	1.55	43.9
	20-2	F104	1.65	31.0
03 NOV 66	13-1	B58	1.57	35.
	13-2	XB70	1.80	60.0
	13-3	F104	1.34	20.0
	SR1	SR71	.	.
	SR2	SR71	.	.
04 NOV 66	8K1	F104	.	30.
	8K2	F104	.	30.2
	8K3	F104	.	20.7
	8K4	F104	.	32.6
	8K5	F104	.	32.8
08 NOV 66	21-1	B58	1.51	47.
	22-1	B58	1.65	47.5
	24-1	B58	1.69	47.7
	25-1	B58	1.61	46.8
	26-1	B58	1.51	47.9
	27-2	B58	1.64	47.4
	28-2	B58	1.67	48.0
	29-2	B58	1.62	47.4

DATE	MISSION	AIRCRAFT	MACH NO.	ALTITUDE
	30-2	B58	1.66	47.5
	121-1	B58	1.65	47.4
	31-2	B58	1.60	47.0
	32-2	B58	1.67	48.0
09 NOV 66	X1	F104	.	7.
10 NOV 66	9-1	XB70	2.51	59.
	9-2	B58	1.63	40.4
	9-3	F104	1.14	21.1
	2-1	XB70	1.48	37.3
	2-3	B58	1.48	33.0
	2-4	F104	.	.
14 NOV 66	8K7	F104	.	31.
15 NOV 66	74-1	F104	1.48	50.
	61-1	F104	1.65	29.6
	49-2	F104	1.16	16.6
	50-2	F104	1.21	16.4
16 NOV 66	33-1	B58	1.65	36.
	34-1	B58	1.65	36.0
	35-1	B58	1.63	36.4
	36-1	B58	1.64	36.2
	37-1	B58	1.65	36.0
	38-1	B58	1.64	35.9
	39-1	B58	1.65	35.7
	40-1	B58	1.64	36.2
	85-1	B58	1.63	36.0
	86-1	B58	1.64	36.1

DATE	MISSION	AIRCRAFT	MACH NO.	ALTITUDE
17 NOV 66	87-1	B58	.	36.
	88-1	B58	.	36.3
	41-1	B58	.	36.3
	SR3	SR71	.	.
21 NOV 66	42-1	B58	.	.
	43-2	B58	1.65	25.9
	44-2	B58	1.65	36.4
	45-1	B58	1.63	36.0
	46-1	B58	1.55	35.9
	47-2	B58	1.62	35.8
	48-2	B58	1.65	36.0
23 NOV 66	10-1	XB70	2.46	59.
	10-2	B58	1.32	32.4
	1-1	XB70	1.46	37.2
	1-3	B58	1.4	32.4
	1-4	F104	1.3	18.6
29 NOV 66	51-2	F104	1.3	16.
	64-2	F104	1.65	29.4
	76-2	F104	1.52	50.4
	77-2	F104	1.51	48.8
	SR7	SR71	.	.
30 NOV 66	62-1	F104	1.66	30.
	73-1	F104	1.51	50.1
	63-1	F104	1.62	29.6
	75-1	F104	1.5	49.6
	SR8	SR71	.	.

DATE	MISSION	AIRCRAFT	MACH NO.	ALTITUDE
01 DEC 66	8K18	F104	1.3	30.
	8K19	F104	1.3	30.0
	SR9	SR71	.	.
	SR10	SR71	.	.
	SR11	SR71	.	.
	8K20	F104	1.3	30.8
	8K21	F104	1.3	30.2
02 DEC 66	117-1	F104	1.65	26.
	117-2	B58	1.65	48.0
	118-1	B58	1.65	48.7
	118-2	F104	1.60	26.1
06 DEC 66	65-2	F104	1.60	29.
	52-1	F104	1.3	17.0
	53-1	F104	1.3	17.1
	66-2	F104	1.64	30.1
07 DEC 66	78-2	F104	1.5	50.
	79-1	F104	1.5	50.4
	67-1	F104	1.65	29.6
	54-1	F104	1.3	16.5
	119-1	F104	1.65	26.4
08 DEC 66	221-1	B58	1.4	47.
	122-1	B58	1.65	48.6
	123-1	B58	1.51	47.6
	124-1	B58	1.65	48.2
	125-1	B58	1.65	48.2
	126-1	B58	1.65	50.2

DATE	MISSION	AIRCRAFT	MACH NO.	ALTITUDE
	127-2	B58	1.65	49.0
	SR12	SR71	•	•
	128-2	B58	1.4	41.6
	129-2	B58	1.65	48.8
	130-2	B58	1.65	48.4
	131-2	B58	1.65	48.5
	132-2	B58	1.65	48.3
	SR13	SR71	•	•
09 DEC 66	82-2	F104	1.5	50.
	69-1	F104	1.67	29.6
	56-1	F104	1.28	16.5
	57-1	F104	1.29	16.0
	SR14	SR71	•	•
12 DEC 66	5-1	B58	1.65	36.
	5-2	XB70	2.49	59.1
	3-1	B58	1.5	32.4
	3-3	F104	•	•
	3-2	XB70	1.5	37.6
	3-4	F104	1.3	17.8
	SR15	SR71	•	•
13 DEC 66	SR16	SR71	•	•
	SR17	SR71	•	•
	SR18	SR71	•	•
	8KC1A	B58	1.4	45.5
16 DEC 66	11-1	F104	1.4	20.
	11-2	B58	1.65	40.2

DATE	MISSION	AIRCRAFT	MACH NO.	ALTITUDE
	11-3	XB70	2.5	59.4
	4-1	B58	1.5	32.0
	4-2	XB70	1.5	38.6
	SR19	SR71	.	.
	SR20	SR71	.	.
17 DEC 66	SR21	SR71	.	.
19 DEC 66	SR22	SR71	.	.
20 DEC 66	83-2	F104	1.5	50.
	71-2	F104	1.58	30.6
	72-2	F104	1.42	34.3
	58-2	F104	1.3	16.8
	59-2	F104	1.34	16.6
	6-1	B58	1.65	35.5
	6-2	XB70	2.5	60.0
	14-1	XB70	1.8	59.7
	14-2	B58	1.53	38.8
	14-3	F104	1.3	21.4
	SR23	SR71	.	.
04 JAN 67	12-1	B58	1.65	39.
	12-2	XB70	2.50	60.3
	12-3	F104	1.42	22.0
	113-1	B58	1.65	39.1
	113-2	XB70	1.81	60.3
	113-3	F104	1.40	20.6
06 JAN 67	SR27	SR71	.	.
09 JAN 67	8KS10	F104	1.30	30.

DATE	MISSION	AIRCRAFT	MACH NO.	ALTITUDE
	8KS11	F104	1.30	30.0
	8KS13	F104	1.30	30.6
	8KS14	F104	1.30	30.1
	8KS16	F104	1.30	31.4
	8KS17	F104	1.30	30.7
	8KS19	F104	1.30	30.0
	8KS20	F104	1.30	30.5
	TFX1	F111	1.94	40.9
	8KS21	F104	1.30	21.4
10 JAN 67	SR28	SR71	.	.
13 JAN 67	7-1	B58	1.62	35.
	7-3	XB70	2.50	60.3
	15-3	F104	1.40	20.2
	15-1	XB70	1.80	60.6
	15-2	B58	1.65	39.6
	SR29	SR71	.	.
16 JAN 67	TFX2	F111	.	.
	FF1	T38	.	.
	FF2	T38	.	.
	FF3	T38	.	.
17 JAN 67	8-1	B58	1.65	35.
	8-3	XB70	2.5	60.0
	16-1	B58	1.65	39.7
	16-2	XB70	1.80	59.7
	16-3	F104	1.40	20.6
	SR30	SR71	.	.

DATE	MISSION	AIRCRAFT	MACH NO.	ALTITUDE
	SR31	SR71	.	.
18 JAN 67	FF4	F104	.	.
	FF5	F104	.	.
	FF6	F104	.	.
16 FEB 67	TONT1	B58	1.65	48.
	TONT2	B58	1.65	48.0
	SRP1	SR71	.	.
	TONT3	B58	1.65	48.0
21 FEB 67	TONT5	B58	1.65	48.
	TONT6	B58	1.65	39.0
	TONT7	B58	1.65	48.0
	TONT8	B58	1.65	48.0
02 MAR 67	UINT1	B58	1.65	48.
	UINT2	B58	1.59	48.
	UINT3	B58	1.65	48.

APPENDIX B

DEFORMATION OF AN ELASTIC HALF-SPACE

The complete system of equations of equilibrium of a homogeneous isotropic elastic solid is composed of the following two equations:

(a) Equations of equilibrium

$$\tau_{ij,j} + F_i = 0 \qquad (i,j = 1,2,3)$$

(1)

(b) Stress-strain relations

$$\tau_{ij} = \lambda\, \delta_{ij}\theta + 2\mu\, e_{ij}$$

where

F_i	are body forces
τ_{ij}	are the stresses
λ,μ	are Lame's elastic constants
δ_{ij}	is the Kronecker delta
θ	is the dilatation
e_{ij}	are the strains

A repeated subscript in a term implies summation as the index that is repeated takes on values of 1, 2, and 3. A comma in the subscript indicates differentiation with respect to the indices following the comma.

The dilatation, θ, is given by

$$\theta = e_{11} + e_{22} + e_{33} = \frac{\alpha u_1}{\alpha x_1} + \frac{\alpha u_2}{\alpha x_2} + \frac{\alpha u_3}{\alpha x_3} = u_{i,i}$$

where

$$e_{ij} = 1/2\ (u_{i,j} + u_{j,i})$$

and u_i are the components of displacement.

In order to express (1) in terms of displacements, substitute for θ and e_{ij} in (1b), giving,

$$\tau_{ij} = \lambda\delta_{ij}u_{k,k} + \mu u_{i},_{jj} + F_i = 0 \qquad (2)$$

or

$$\mu\nabla^2 u_i + (\lambda + \mu)\frac{\alpha\theta}{\alpha x_i} + F_i = 0 \qquad (3)$$

These are known as Navier's equations.

It is necessary to obtain the general solution of (3) by adding solutions of

$$\mu\nabla^2 u_i + (\lambda + \mu)\frac{\alpha\theta}{\alpha x_i} = 0$$

to particular solutions of (3)

Kelvin (1848) was responsible for a solution of Navier's non-homogeneous equations given in (3), namely

$$U_i(x) = \frac{\lambda + \mu}{8\pi\mu(\lambda+2\mu)}\int_v \left[\left(\frac{\lambda + 3\mu}{\lambda + \mu}\right)\frac{F_i(\xi)}{r} - \frac{\alpha}{\alpha x_i}\left(\frac{1}{r}\right)(x_j - \xi_j)F_j(\xi)\right] dv \qquad (4)$$

where $r^2 = (x_1 - \xi)^2 + (x_2 - \xi_2)^2 + (x_3 - \xi_3)^2$ gives the distance from the field point (x_1, x_2, x_3) to a variable point (ξ_1, ξ_2, ξ_3) inside v. The $F_i(\xi)$ are the components of the body force F_i in terms of the variable of integration ξ_i.

Suppose that the forces are distributed over a region v_1 (which includes ξ), which is a part of v. Also, suppose that the forces vanish in the remainder of v. The resultant of the body forces on v_1 is

$$F_i{}^\circ = \int_{v_1} F_i dv \qquad (5)$$

Let F_i increase so that the integral has a finite limit $F_i{}^\circ$ as v_i is made to approach zero. This gives the impression of a concentrated force $F_i{}^\circ$ at ξ_i.

Equation (4) can be rewritten as

$$U_i(x) = \frac{\lambda+3\mu}{8\pi\mu(\lambda+2\mu)}\int_v \frac{F_i(\xi)}{r}\,dv - \frac{(\lambda+\mu)}{8\pi\mu(\lambda+2\mu)}\int_v \frac{\alpha}{\alpha x_i}\left(\frac{1}{r}\right)(x_j - \xi_j)F_j(\xi)dv \qquad (6)$$

Substituting from (5) and differentiating under the second integral:

$$U_i(x) = \frac{\lambda+3\mu}{8\pi\mu(\lambda+2\mu)} \cdot \frac{F_i^\circ}{r} + \frac{(\lambda+\mu)}{8\pi\mu(\lambda+2\mu)} \frac{(x_i-\xi_i)(x_j-\xi_j)}{r^3} F_j^\circ \qquad (7)$$

where u is the displacement produced at x_i by a force F_i° at ξ_i, provided that $x_i \neq \xi_i$. Because of the problem of $x_i=\xi_i$, the point is assumed to be surrounded by a small sphere of radius a. The solutions in the remaining region then correspond to the deformation present in a body v with a cavity of radius a, subjected to forces with resultant F_i°.

If the coordinate axes are chosen so that F_1° acts at the origin, then $\xi_i = (0,0,0)$.

Also, if $F_1^\circ = 0$, $F_2^\circ = 0$, and $F_3^\circ = P$, then from (7)

$$\begin{aligned} u_1 &= C\,\frac{x_1x_3}{r^3} \\ u_2 &= C\,\frac{x_2x_3}{r^3} \\ u_3 &= C\left[\frac{\lambda+3\mu}{\lambda+\mu}\ \frac{1}{r}\ \cdot + \frac{x_3^2}{r^3}\right] \end{aligned} \qquad (8)$$

where $r^2 = x_ix_i$ and $C = \dfrac{(\lambda+\mu)P}{8\pi\mu(\lambda+2\mu)}$

Equations (8) represent the displacement at x_i in a medium due to a force P applied within a sphere of radius a.

It will now be necessary to compute the stresses and tractions over the sphere. Recalling the stress-strain relations,

$$\tau_{ij} = \lambda u_{k,k}\,\delta_{ij} + \mu\,(u_{i,j} + u_{j,i})$$

we find,

$$\begin{aligned} \tau_{11} &= \frac{-2\mu Cx_3}{r^3}\left[3\left(\frac{x_1}{r}\right)^2 - \frac{\mu}{\lambda+\mu}\right] \\ \tau_{22} &= \frac{-2\mu Cx_3}{r^3}\left[3\left(\frac{x_2}{r}\right)^2 - \frac{\mu}{\lambda+\mu}\right] \end{aligned} \qquad (9)$$

$$\tau_{33} = \frac{-2\mu C x_3}{r^3}\left[3\left(\frac{x_3}{r}\right)^2 + \frac{\mu}{\lambda+\mu}\right]$$

$$\tau_{23} = \frac{-2\mu C x_2}{r^3}\left[3\left(\frac{x_3}{r}\right)^2 + \frac{\mu}{\lambda+\mu}\right]$$

$$\tau_{13} = \frac{-2\mu C x_1}{r^3}\left[3\left(\frac{x_3}{r}\right)^2 + \frac{\mu}{\lambda+\mu}\right]$$

$$\tau_{12} = \frac{-6\mu C x_1 x_2 x_3}{r^5}$$

It should be noted that on the plane $x_3 = 0$, the normal stresses vanish.

The tractions T_i produced by these stresses over the sphere of radius $r = a$ are determined from

$$T_i = \tau_{ij}\,\nu_j \quad \text{with} \quad \nu_j = x_j/a$$

We get

$$T_1 = \frac{-6\mu C x_1 x_3}{a^4} \tag{10}$$

$$T_2 = \frac{-6\mu C x_2 x_3}{a^4}$$

$$T_3 = \frac{-6\mu C x_3^2}{a^4} - \frac{2\mu^2 C}{(\lambda+\mu)a^2}$$

and on integrating over the surface of the sphere $r = a$, we find,

$$\int_S T_1 d\sigma = 0, \quad \int_S T_2 d\sigma = 0, \quad \int_S T_3 d\sigma = \frac{-8\pi\mu C(\lambda+2\mu)}{\lambda+\mu} \tag{11}$$

These are the components of the resultant force exerted on S by matter exterior to S.

Whatever the radius of the cavity may be, this system of tractions is statically equivalent to a single force, applied at the origin, directed along the axis of Z in the positive direction, and of magnitude $8\pi\mu C(\lambda+2\mu)/(\lambda+\mu)$.

Boussinesq (1885) determined another solution of Navier's equation for the conditions of: (1) a force acting at the origin along x_3 and (2) no change of volume for points located along the negative Z axis. The solutions are:

$$u_1 = \frac{Dx_1}{r(r+x_3)} , \qquad u_2 = \frac{Dx_2}{r(r+x_3)} \tag{12}$$

$$u_3 = \frac{D}{r} \qquad \text{where } r^2 = x_i x_i \text{ and } D = \text{const.}$$

This is called the dilatationless solution of Navier's equations. It may easily be verified that this is a solution by substitution into Navier's equation for the condition of $\theta = 0$. Equations (12) represent a solution for the displacement at any point in the body except the origin and points on the negative Z axis. The stresses in the body from this solution can be computed from the stress-strain relationship which gives:

$$\tau_{11} = 2\mu D \left[\frac{x_2^2 + x_3^2}{r^3(r+x_3)} - \frac{x_1^2}{r^2(r+x_3)^2} \right]$$

$$\tau_{22} = 2\mu D \left[\frac{x_1^2 + x_3^2}{r^3(r+x_3)} - \frac{x_2^2}{r^2(r+x_3)^2} \right]$$

$$\tau_{33} = -2\mu D \frac{x_3}{r^3} \tag{13}$$

$$\tau_{13} = -2\mu D \frac{x_1}{r^3}$$

$$\tau_{23} = -2\mu D \frac{x_2}{r^3}$$

$$\tau_{12} = -2\mu D \frac{x_1 x_2 (x_3+2r)}{r^3(r+x_3)^2}$$

It should be noted from equation (13) that the normal stress on the plane $x_3 = 0$ is zero.

The tractions over the surface of the sphere of radius a are:

$$T_1 = -2\mu D \frac{x_1}{r^2(r+x_3)} \quad , \quad T_2 = -2\mu D \frac{x_2}{r^2(r+x_3)}$$

$$T_3 = -2\mu D \frac{1}{r^2} \quad , \quad r = a \tag{14}$$

The components of the resultant force R_i exerted on the sphere by the matter exterior to the sphere are:

$$R_1 = \int_S T_1 \, d\sigma = 0$$

$$R_2 = \int_S T_2 \, d\sigma = 0 \tag{15}$$

$$R_3 = \int_S T_3 \, d\sigma = -8\pi\mu D$$

We will now consider a semi-infinite region $x_3 \geq 0$ to be occupied by an elastic medium and assume that a concentrated force P, applied at the origin, acts in the positive direction of x_3. Since the point of application of the load is a singular point in the solution of Navier's equations, we delete it from the region $x_3 \geq 0$ by describing a hemisphere of small radius a and confine our attention to the semi-infinite region bounded by the $x_3 = 0$ plane.

We shall construct a solution such that the resultant of all external stresses acting on the hemisphere is P and $\tau_{13} = \tau_{23} = \tau_{33} = 0$ over the rest of the boundary.

Forming the sum of the displacements of (8) and (12), we obtain

$$u_1 = \frac{C\, x_1 x_3}{r^3} + \frac{Dx_1}{r(r+x_3)}$$

$$u_2 = \frac{C\, x_2 x_3}{r^3} + \frac{Dx_2}{r(r+x_3)} \tag{16}$$

$$u_3 = C\left(\frac{\lambda+3\mu}{\lambda+\mu} \cdot \frac{1}{r} + \frac{x_3^2}{r^3}\right) + \frac{D}{r}$$

The principle of superposition insures that the distribution of tractions over the surface of the hemisphere corresponding to the sum of the displacements can be obtained by summing the tractions in (10) and (14). Equations (11) and (15) show that the resultant force on the hemisphere acts in the x_3 direction and has magnitude

$$R = \frac{-4\pi\mu C(\lambda+2\mu)}{\lambda+\mu} - 4\pi\mu D \tag{17}$$

This is one-half the sum of the values given by equations (11) and (15) wherein the integration was performed over the entire sphere.

Since this represents the action of the medium on the hemisphere, we equate R to -P and get the equation

$$P = \frac{4\pi\mu C(\lambda+2\mu)}{\lambda+\mu} + 4\pi\mu D \tag{18}$$

involving two unknown constants C and D.

Using the boundary condition $\tau_{13} = \tau_{23} = \tau_{33} = 0$ on $x_3 = 0$, we can obtain another equation involving these constants. Therefore, at $x_3 = 0$,

$$\begin{aligned}
\tau_{13} &= \left\{\frac{-2\mu Cx_1}{r^3}\left[3\left(\frac{x_3}{r}\right)^2 + \frac{\mu}{\lambda+\mu}\right] - \frac{2\mu\ Dx_1}{r^3}\right\}_{x_3=0} = 0 \\
\tau_{23} &= \left\{\frac{-2\mu Cx_2}{r^3}\left[3\left(\frac{x_3}{r}\right)^2 + \frac{\mu}{\lambda+\mu}\right] - \frac{2\mu\ Dx_2}{r^3}\right\}_{x_3=0} = 0 \\
\tau_{33} &= \left\{\frac{-2\mu Cx_3}{r^3}\left[3\left(\frac{x_3}{r}\right)^2 + \frac{\mu}{\lambda+\mu}\right] - \frac{2\mu Dx_3}{r^3}\right\}_{x_3=0} = 0
\end{aligned} \tag{19}$$

Then,

$$\begin{aligned}
\tau_{13} &= \frac{-2\mu Cx_1}{r^3} \cdot \frac{\mu}{\lambda+\mu} - \frac{2\mu Dx_1}{r^3} = 0 \\
\tau_{23} &= \frac{-2\mu Cx_2}{r^3} \cdot \frac{\mu}{\lambda+\mu} - \frac{2\mu Dx_2}{r^3} = 0 \\
\tau_{33} &= 0
\end{aligned} \tag{20}$$

and

$$D = \frac{-C\mu}{(\lambda+\mu)} \tag{21}$$

giving

$$P = \frac{4\pi\mu C(\lambda+2\mu)}{\lambda+\mu} - \frac{4\pi\mu^2 C}{(\lambda+\mu)}$$

or

$$\frac{P}{4\pi\mu} = C\,\frac{(\lambda+2\mu-\mu)}{(\lambda+\mu)}$$

$$C = \frac{P}{4\pi\mu} \tag{22}$$

and

$$D = \frac{-\ P}{4\pi(\lambda+\mu)} \tag{23}$$

Substituting C and D into equation (16),

$$\begin{aligned} u_1 &= \frac{P}{4\pi\mu} \cdot \frac{x_1 x_3}{r^3} - \frac{P}{4\pi(\lambda+\mu)} \cdot \frac{x_1}{r(r+x_3)} \\ u_2 &= \frac{P}{4\pi\mu} \cdot \frac{x_2 x_3}{r^3} - \frac{P}{4\pi(\lambda+\mu)} \cdot \frac{x_2}{r(r+x_3)} \\ u_3 &= \frac{P}{4\pi\mu} \left(\frac{\lambda+3\mu}{\lambda+\mu} \cdot \frac{1}{r} + \frac{x_3^2}{r^3} \right) + \frac{P}{4\pi(\lambda+\mu)r} \end{aligned} \tag{24}$$

Equations (24) are the solution to the displacement at any point other than the origin in an isotropic, elastic half-space due to a concentrated force at the origin. Some insight into the reasoning behind the combination of two particular solutions for an extended solid to give a solution for a half-space may be obtained from the following points:

(a) At least two solutions were needed in order to make the shear stresses vanish in the plane $x_3 = 0$. For example, if only the first solution had been used, we would have at $x_3 = 0$,

$$\tau_{13} = \frac{-2\mu C x_1}{r^3} \cdot \frac{\mu}{\lambda+\mu} = 0$$

$$\tau_{23} = \frac{-2\mu C x_2}{r^3} \cdot \frac{\mu}{\lambda+\mu} = 0$$

But this can be true only if $C = 0$ or $x_1 = 0$ and $x_2 = 0$. However, if $C = 0$, all displacements vanish, giving a trivial solution, and if $x_1 = 0$ and $x_2 = 0$, $r = 0$, which is a singular point of the solution. We therefore need to add in the shear stresses due to another solution, which has another constant, and make the sum of the shear stresses vanish.

(b) No more than two solutions are needed because only two additional conditions are necessary to specify a concentrated force acting on a stress-free boundary, namely, the vanishing of the shear stresses and the specification of the value of the sum of the concentrated forces at the origin.

(c) The particular two solutions used were utilized because they are two most readily-obtainable solutions in which a concentrated force acts downward at the origin and the normal stresses vanish on the plane $x_3 = 0$. If neither the shear nor the normal stresses had vanished on the plane, superposition of the two solutions would have been insufficient to obtain the desired final solution.

The solutions (24) can be generalized to yield the displacements in a half-space due to a continuous load distribution. If we let $p(\xi,\eta)$ be the distributed normal load acting at the point (ξ,η) of the plane $x_3 = 0$, the resultant force P on an element of area $d\sigma$ is $P = p(\xi,\eta)\, d\sigma$.

Inserting this in (24), we obtain

$$u_1 = \frac{x_3 x_1}{4\pi\mu} \iint_{-\infty}^{\infty} \frac{p(\xi,\eta)d\xi d\eta}{r^3} - \frac{x_1}{4\pi(\lambda+\mu)} \iint_{-\infty}^{\infty} \frac{p(\xi,\eta)d\xi d\eta}{r(r+x_3)}$$

$$u_1 = \frac{x_3 x_2}{4\pi\mu} \iint_{-\infty}^{\infty} \frac{p(\xi,\eta)d\xi d\eta}{r^3} - \frac{x_2}{4\pi(\lambda+\mu)} \iint_{-\infty}^{+\infty} \frac{p(\xi,\eta)d\xi d\eta}{r(r+x_3)}$$

$$u_3 = \frac{x_3^2}{4\pi\mu} \iint_{-\infty}^{\infty} \frac{p(\xi,\eta)d\xi d\eta}{r^3} + \frac{\lambda+2\mu}{4\pi\mu(\lambda+\mu)} \iint_{-\infty}^{+\infty} \frac{p(\xi,\eta)d\xi d\eta}{r}$$

REFERENCES

Blackman, R. B., and Tukey, J. W., 1958, The measurement of power spectra: New York, Dover, pp. 159.

Boussinesqu, J., 1885, "Applications des potentiels . . .": Paris.

Cook, J. C., 1965, Seismic effects of sonic booms, Proposal 1-380, Teledyne Industries, pp. 1.

Crandell, F. J., 1949, Ground vibration due to blasting and its effect upon structures, Jour. Boston Soc. Civ. Eng., pp. 222-245.

Dibblee, T. W., 1960, Geology of the Rogers Lake and Kramer Quadrangles, California: Geologic Survey Bulletin 1089-B, pp. 137.

Dobrin, M. B., 1952, Introduction to geophysical prospecting: New York, McGraw-Hill, pp. 220.

Duvall, W. I., and Fogelson, D. E., 1962, Review of criteria for estimating damage to residences from blasting vibrations, Report of Investigations 5968, U. S. Dept. of the Interior, Bureau of Mines.

Ferri, A., et al, 1961, The theory of sonic bangs: Progress in aeronautical sciences, London, Pergamon Press.

Geotechnical Corporation, 1965, Installation of a 10-element shallow-buried array at the Uinta Basin Seismological Observatory, Vernal, Utah: Technical Report No. 65-28, p. 1-15.

Gupta, I. N., 1966, Standing waves in a layered half space, BSSA, vol. 56, No. 5, pp. 1153-1161.

Love, A. E. H., 1927, Theory of elasticity: Cambridge.

Press, F., and Ewing, M., 1951a, Ground roll coupling to atmospheric compressional waves: Geophysics, vol. 16, p. 416-430.

Press, F., and Ewing, M., 1951b, Theory of air-coupled flexural waves: Jour. App. Physics, vol. 22, p. 892-899.

Press, F., and Oliver, J., 1956, Model study of air-coupled surface waves: Jour. Acous. Soc. Amer., vol. 27, p. 43-46.

Roller, J. C., Jackson, W. H., Warren, D. H., and Healy, J. H., 1964, A preliminary study of a seismic-refraction survey in the vicinity of the Tonto Forest Observatory, Arizona: Technical Letter Number 23 of U. S. Geol. Surv., 57 p.

REFERENCES (continued)

Sonic Boom Experiments at Edwards Air Force Base. Prepared for the National Sonic Boom Evaluation Office by Stanford Research Institute, Contract AF 49(638)-1758, July 28, 1967.

United States Army Corps of Engineers, 1959, Traffic Evaluation Tests of Rogers Dry Lake, California: Miscellaneous Paper No. 4-265.

Westhusing, J. K., 1966, The effect of crustal structure on teleseismic P-wave travel time anomalies at the TFSO extended array, Arizona, Geotech Technical Report No. 66-17, pp. 11-20.

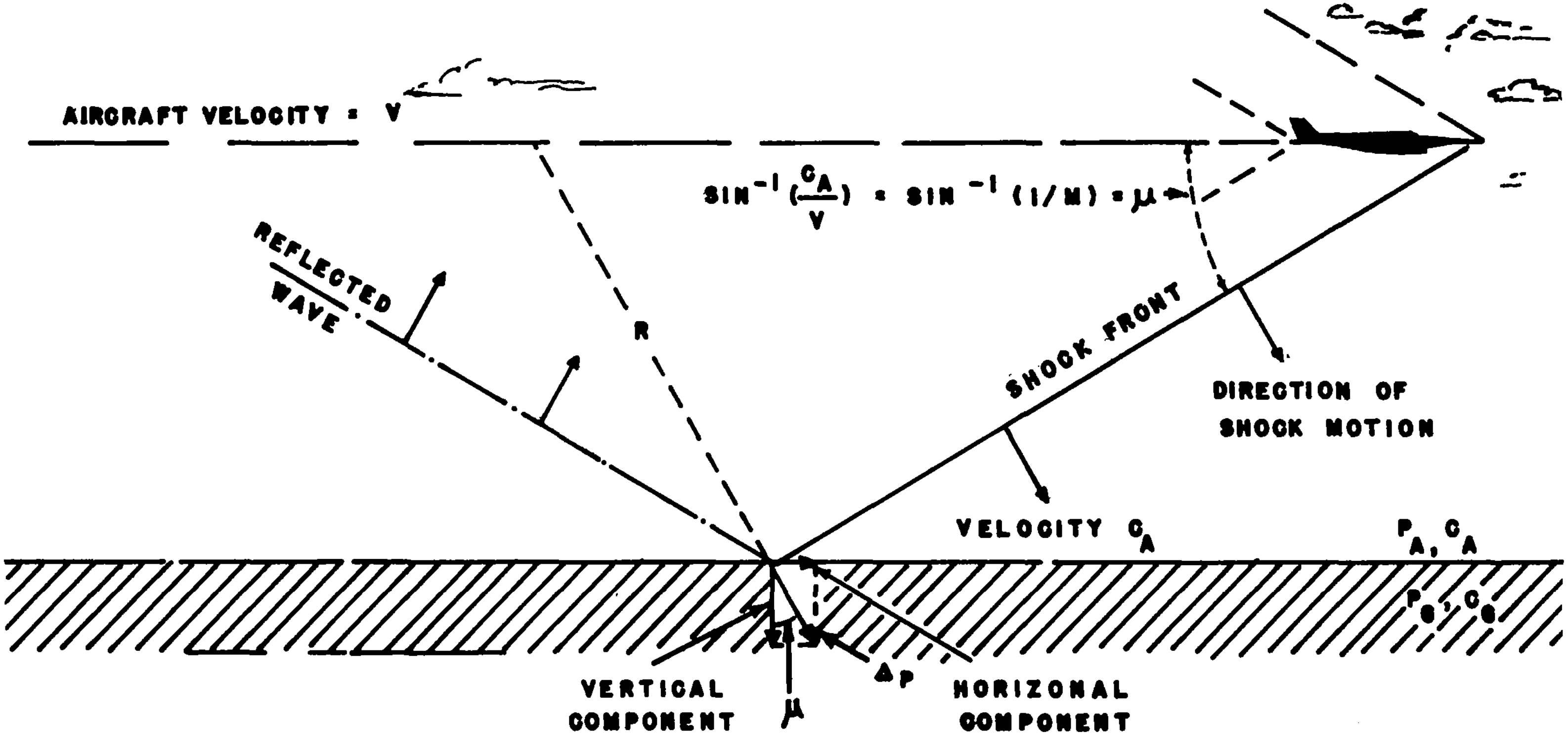

Figure 1. Vertical section showing the sonic boom shock wave interacting with the ground

G 3438

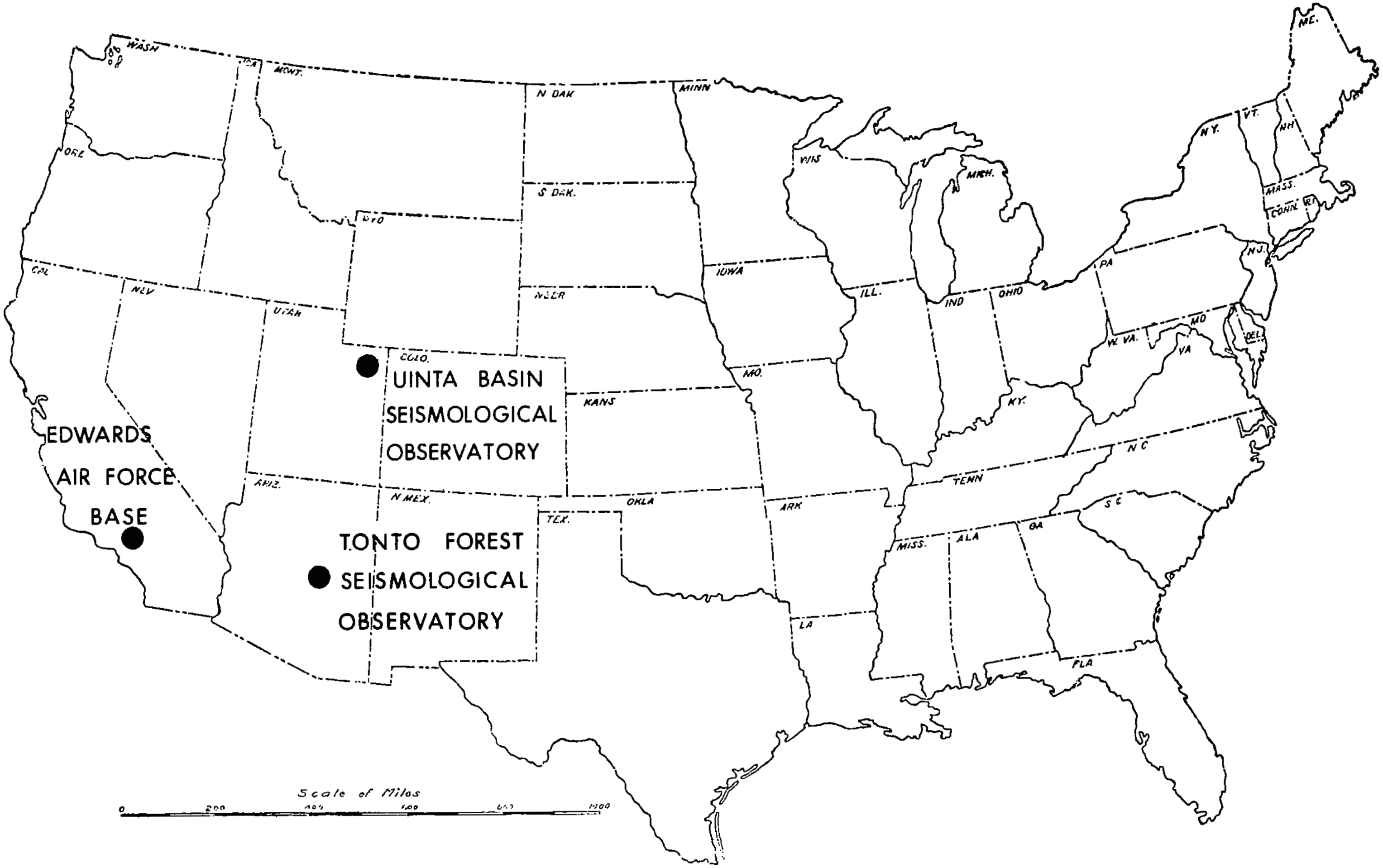

Figure 2. Locations of the test areas used for the study of the seismic effects of sonic booms

G 3439

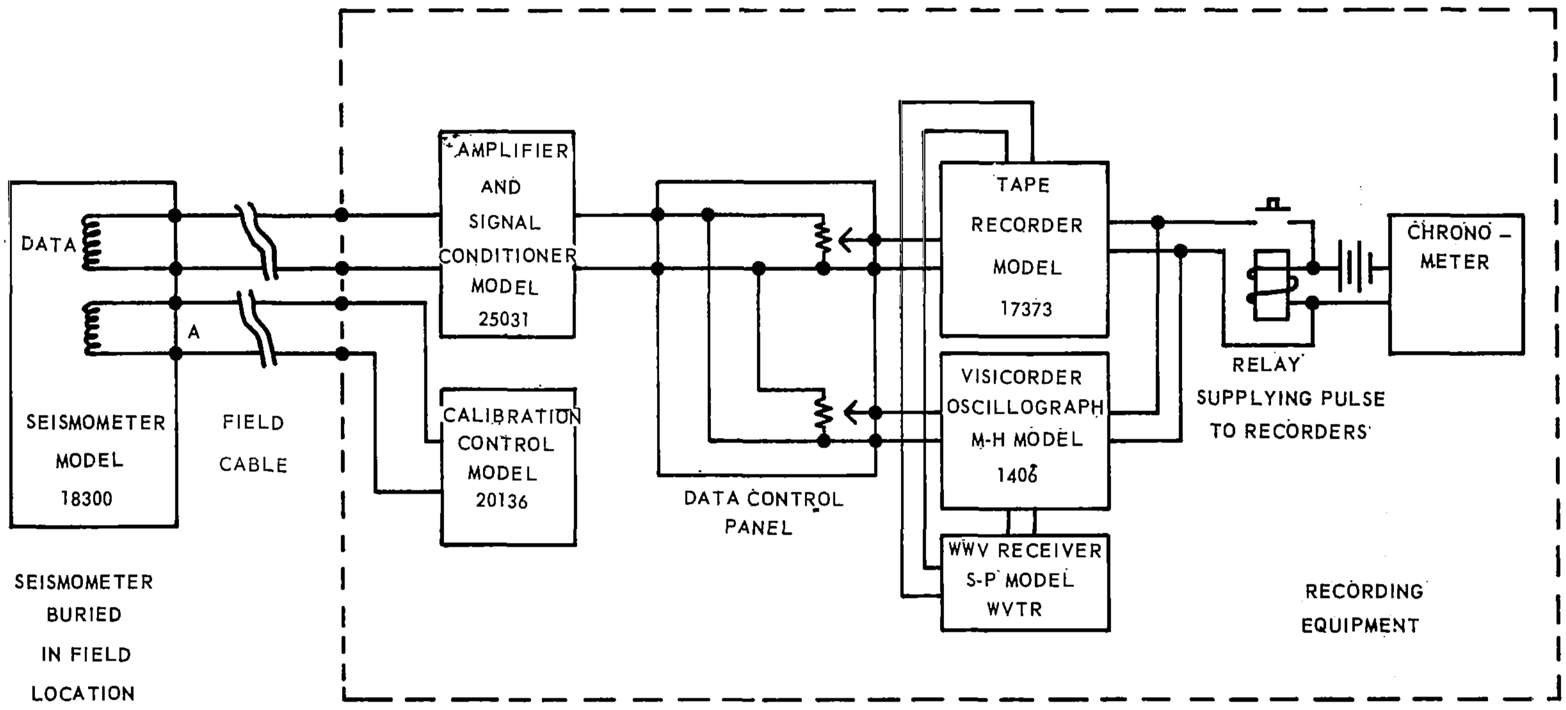

* AMPLIFIER AND SIGNAL CONDITIONER LOCATED AT SEISMOMETER END OF FIELD CABLE FOR LONG LENGTHS OF CABLE.

A POINT OF INSERTION OF VARIABLE FREQUENCY VARIABLE AMPLITUDE SINE WAVE FROM WIDE RANGE OSCILLATOR, H-P MODEL 200 CD.

Figure 3. Block diagram of one seismograph of the mobile equipment

G 3440

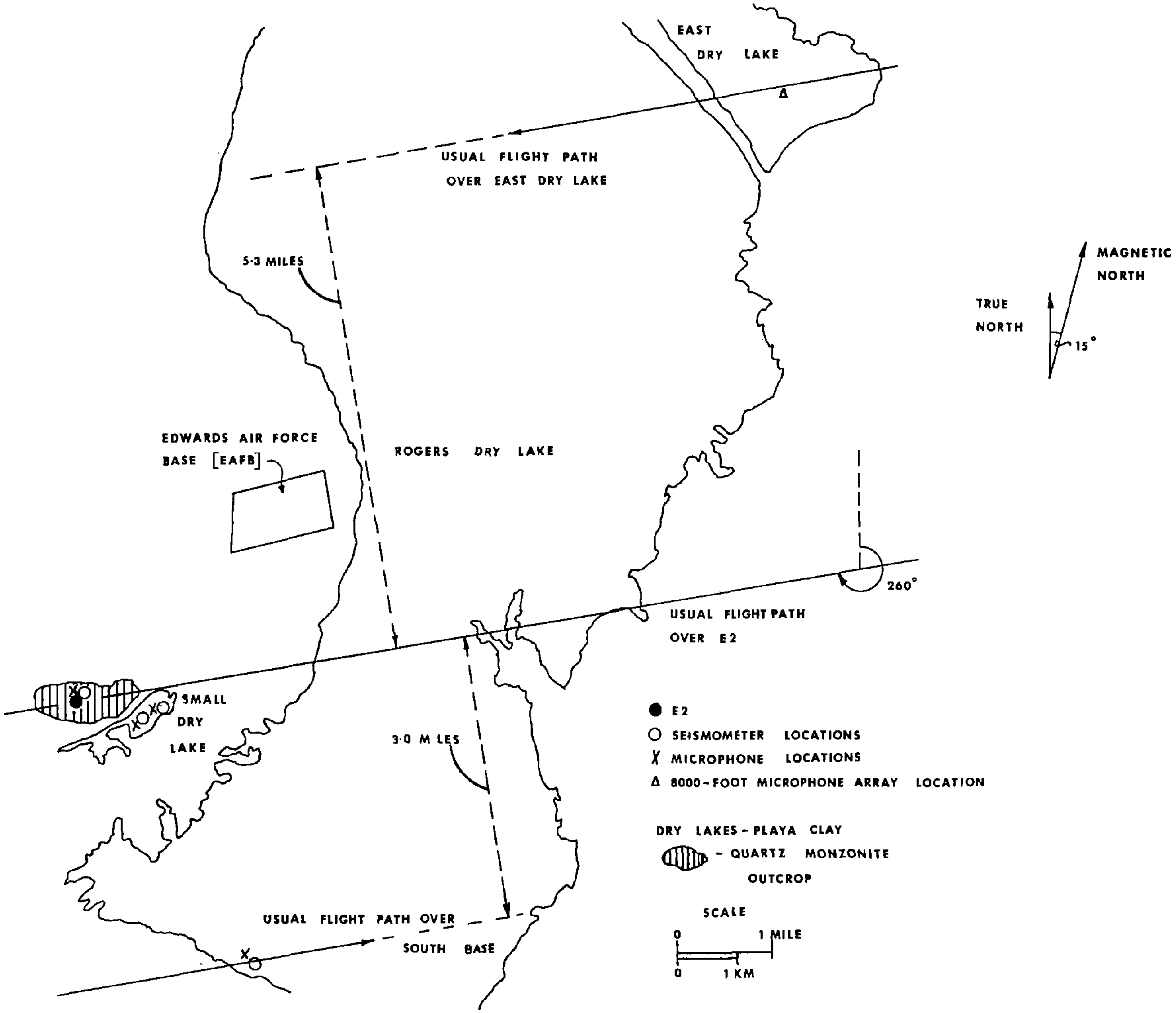

Figure 4. Map of the Edwards Air Force Base test area showing the planned aircraft flight tracks, seismometer locations, and the associated microphone locations

G 3441

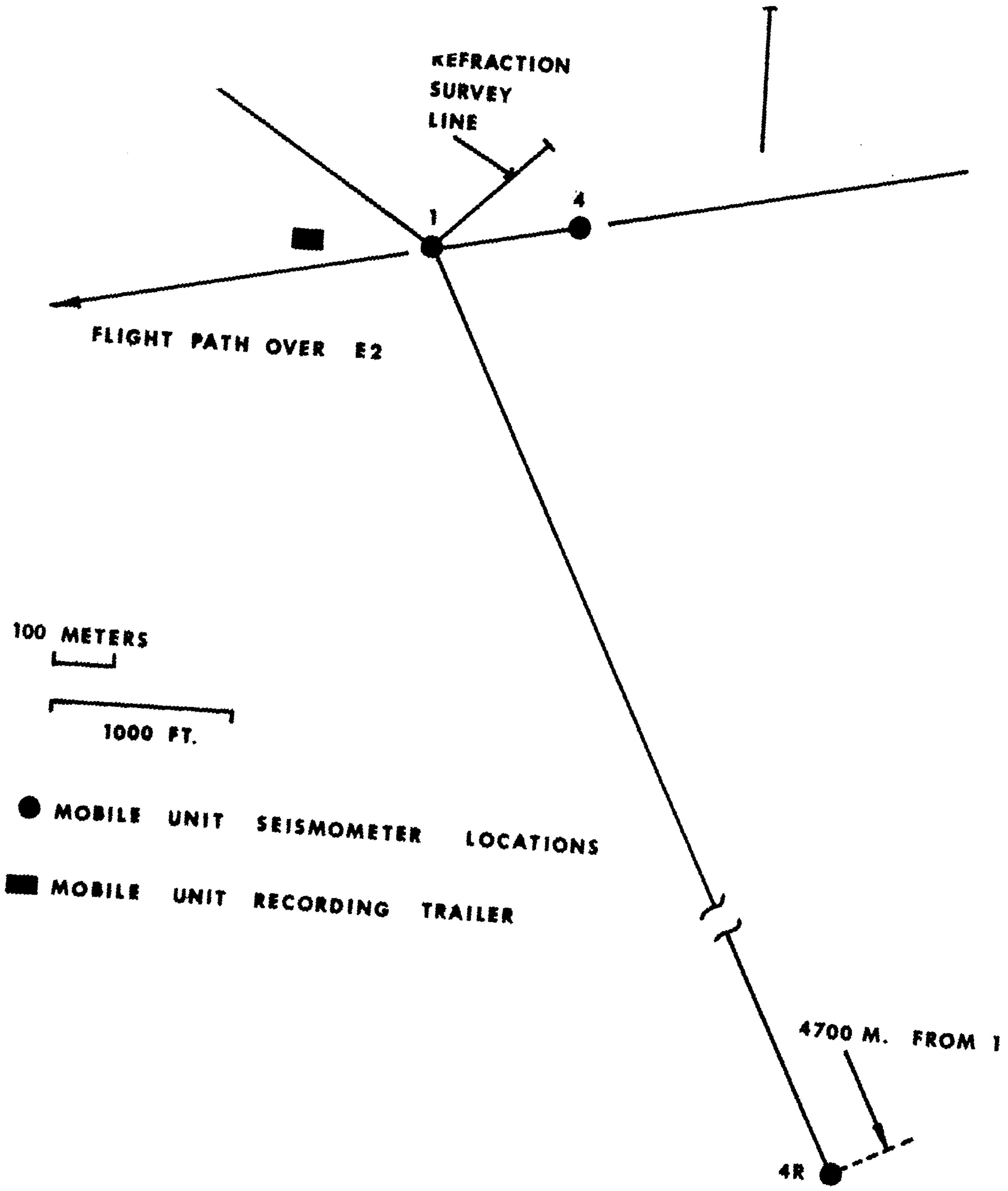

Figure 5. Relative positions of the seismometers used in the sonic boom study at Edwards Air Force Base

G 3442

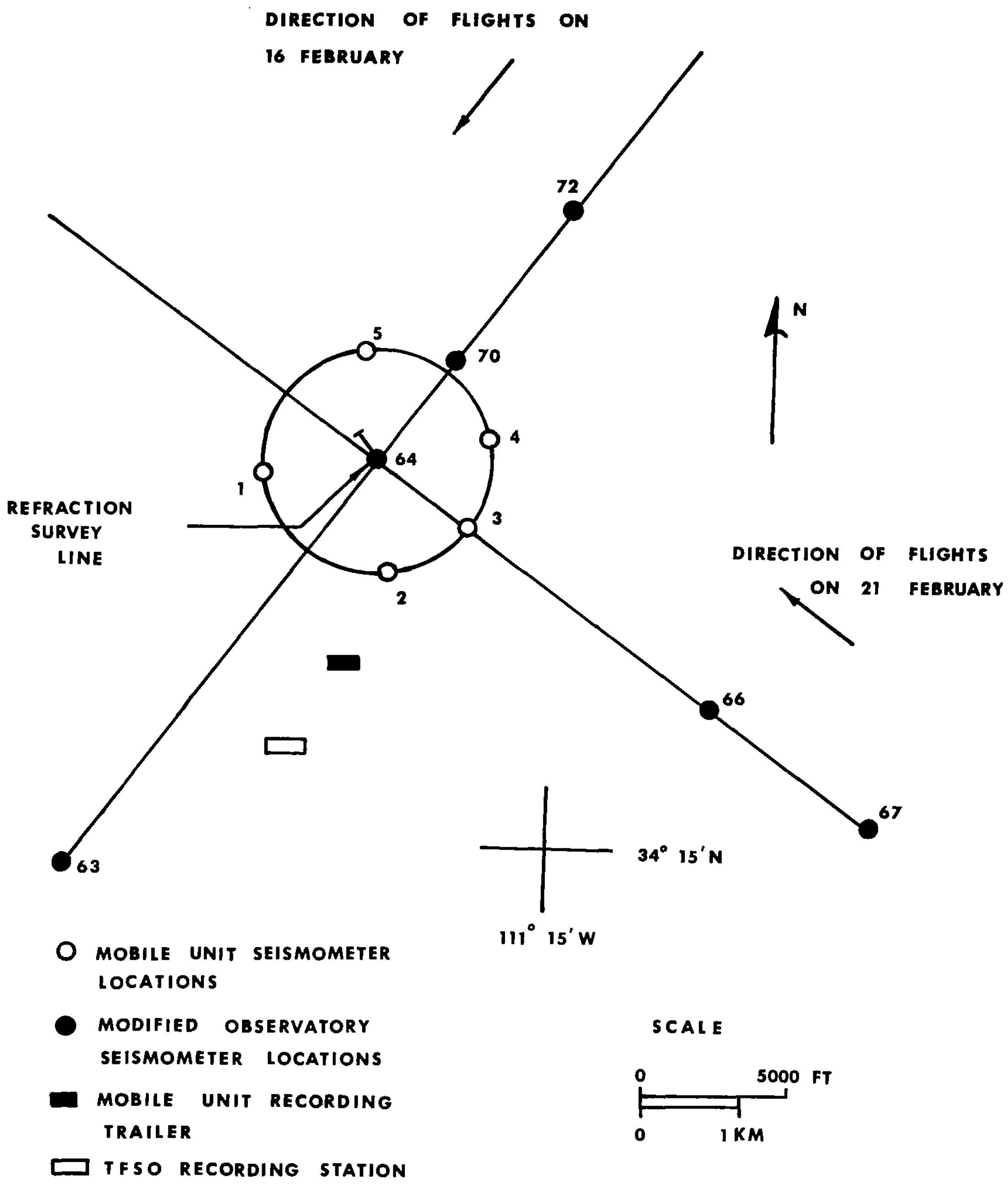

Figure 6. Locations of the seismometers used in the sonic boom seismic measurements program at the Tonto Forest Seismological Observatory

G 3443

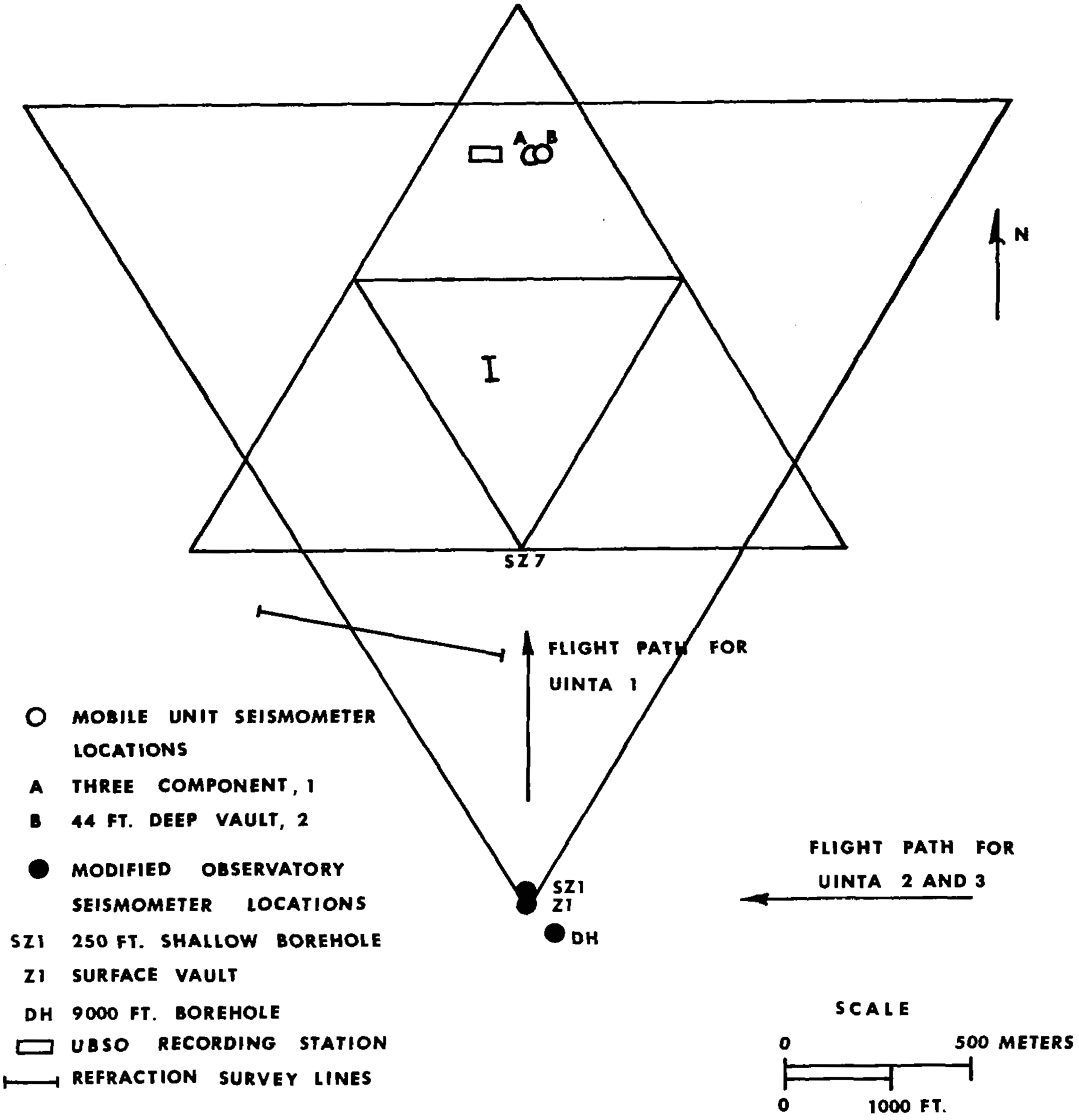

Figure 7. Locations of the seismometers used in the sonic boom seismic measurements program at the Uinta Basin Seismological Observatory

G 3444

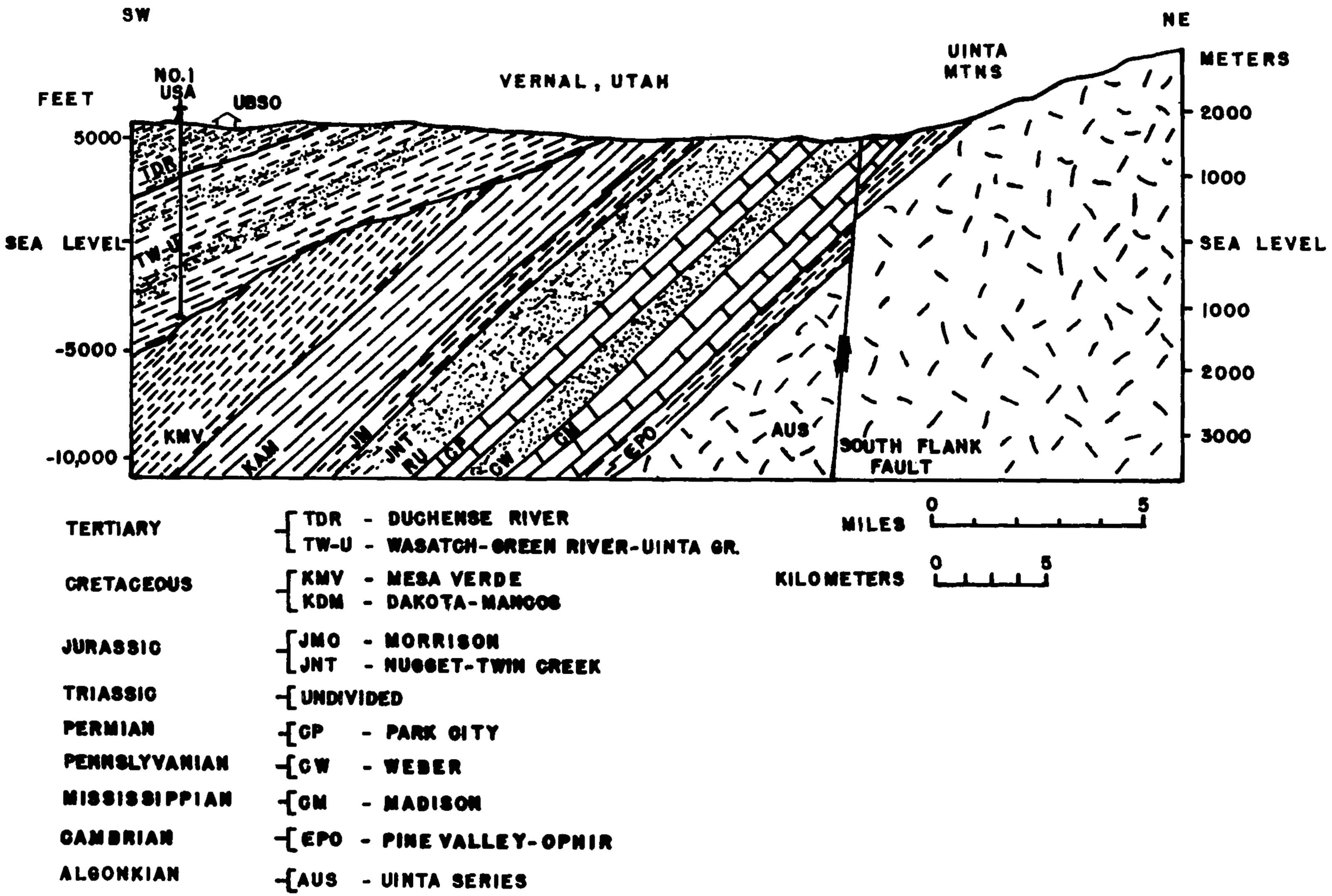

Figure 8. Hypothetical cross-section of the Uinta Uplift and Uinta Basin

G 3445

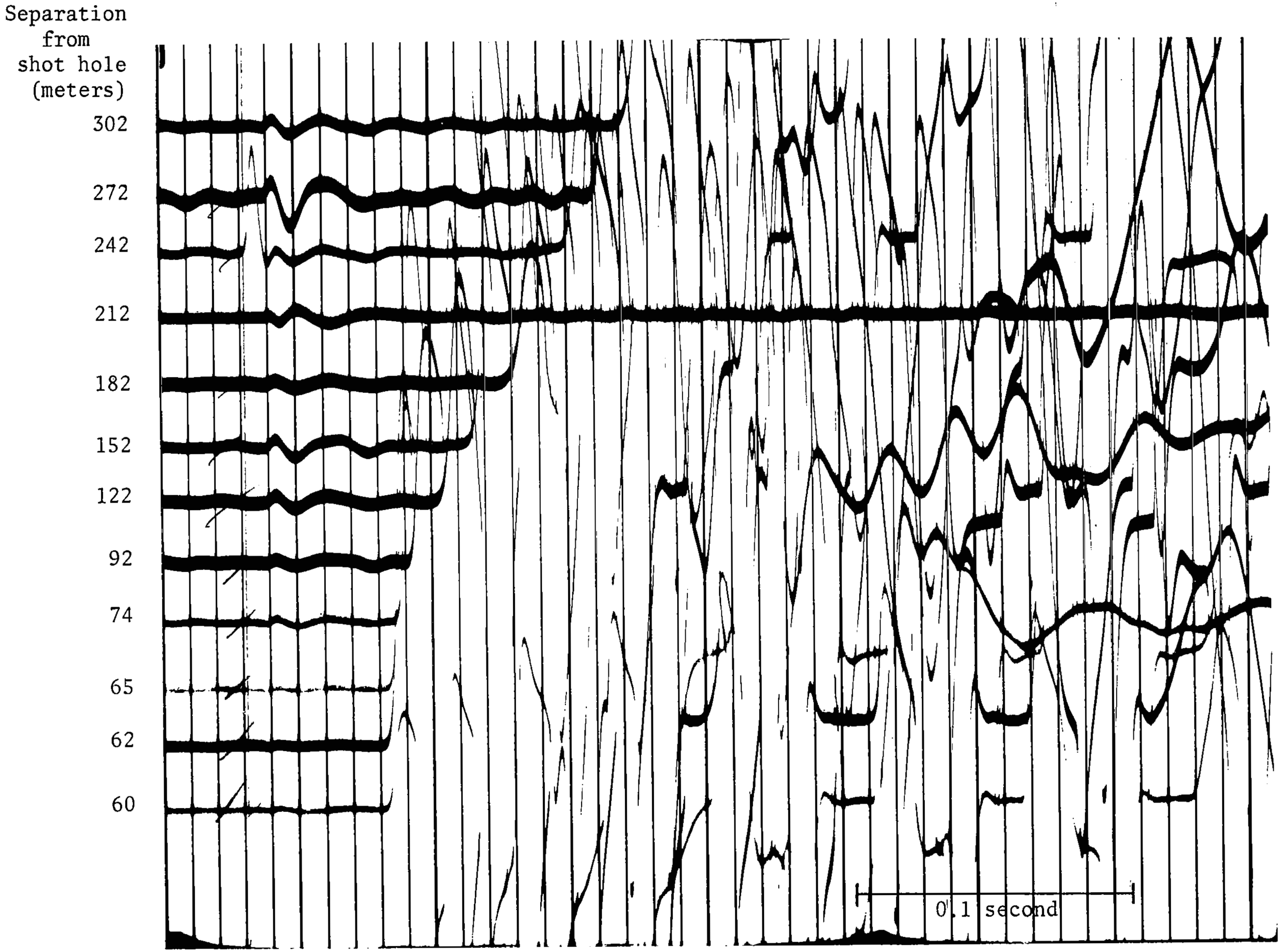

Figure 9. Typical explosion refraction-survey record. The large excursion on channel 3 is the firing pulse

G 3446

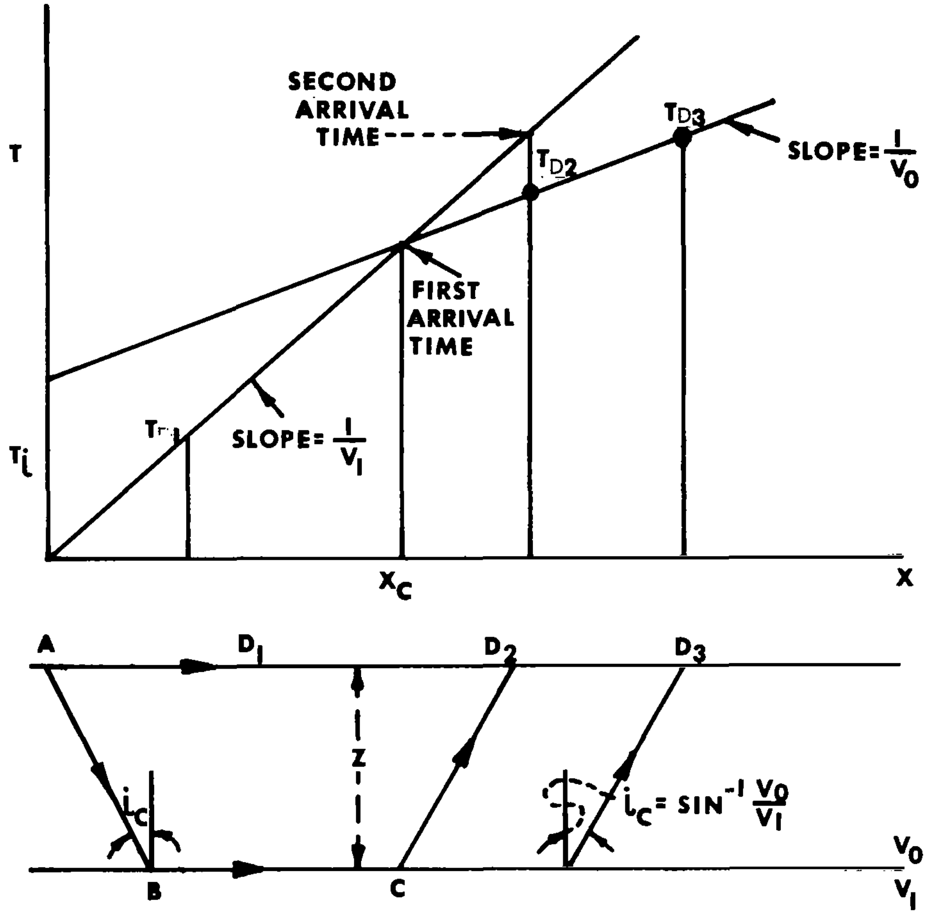

T = TRAVEL TIME

X = DISTANCE

V = COMPRESSIONAL WAVE VELOCITY

Figure 10. Ray paths of least time and the time-distance curve for two layers separated by a horizontal interface

G 3447

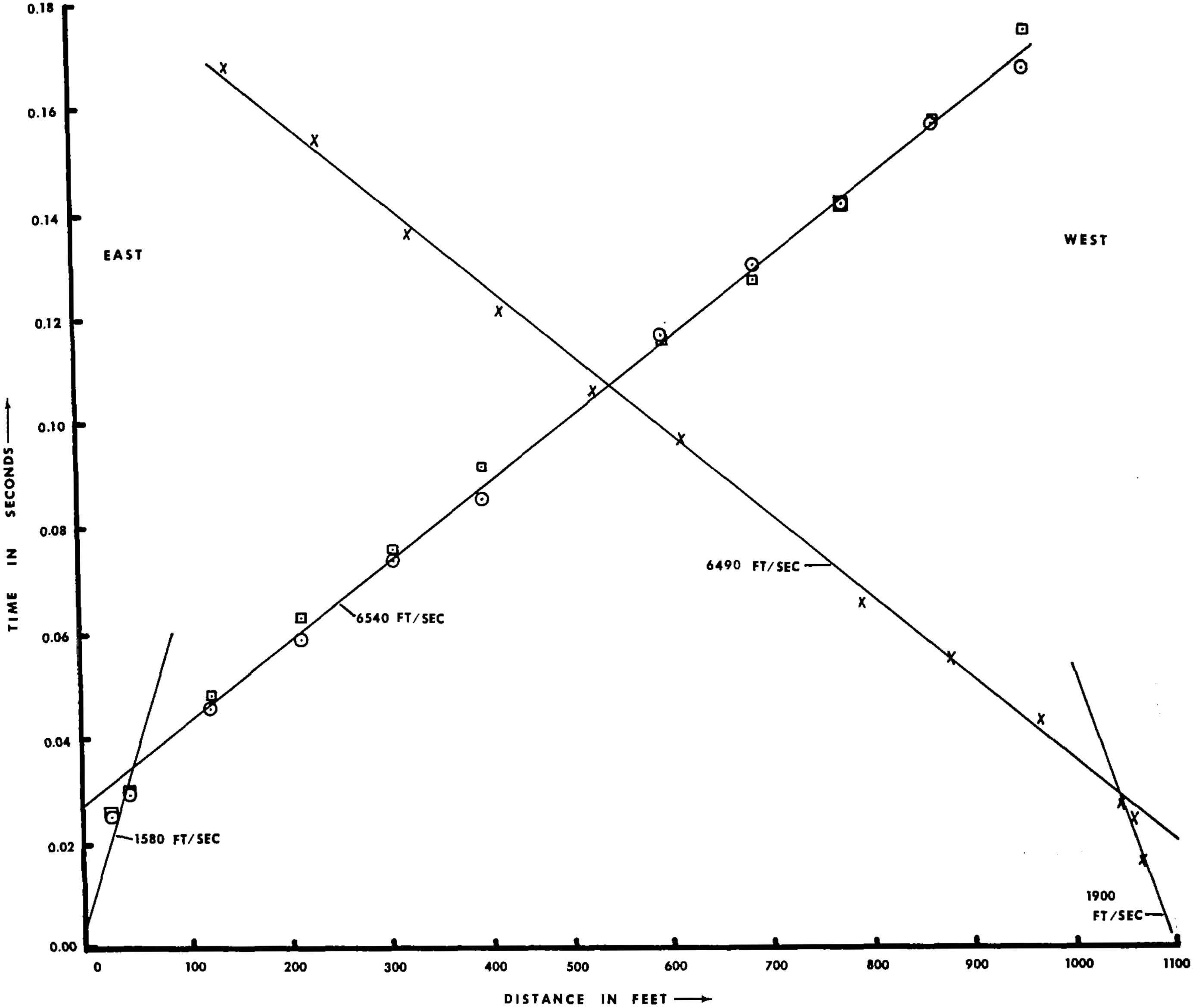

Figure 11. Time-distance curve for the seismic refraction survey at Edwards Air Force Base

G 3448

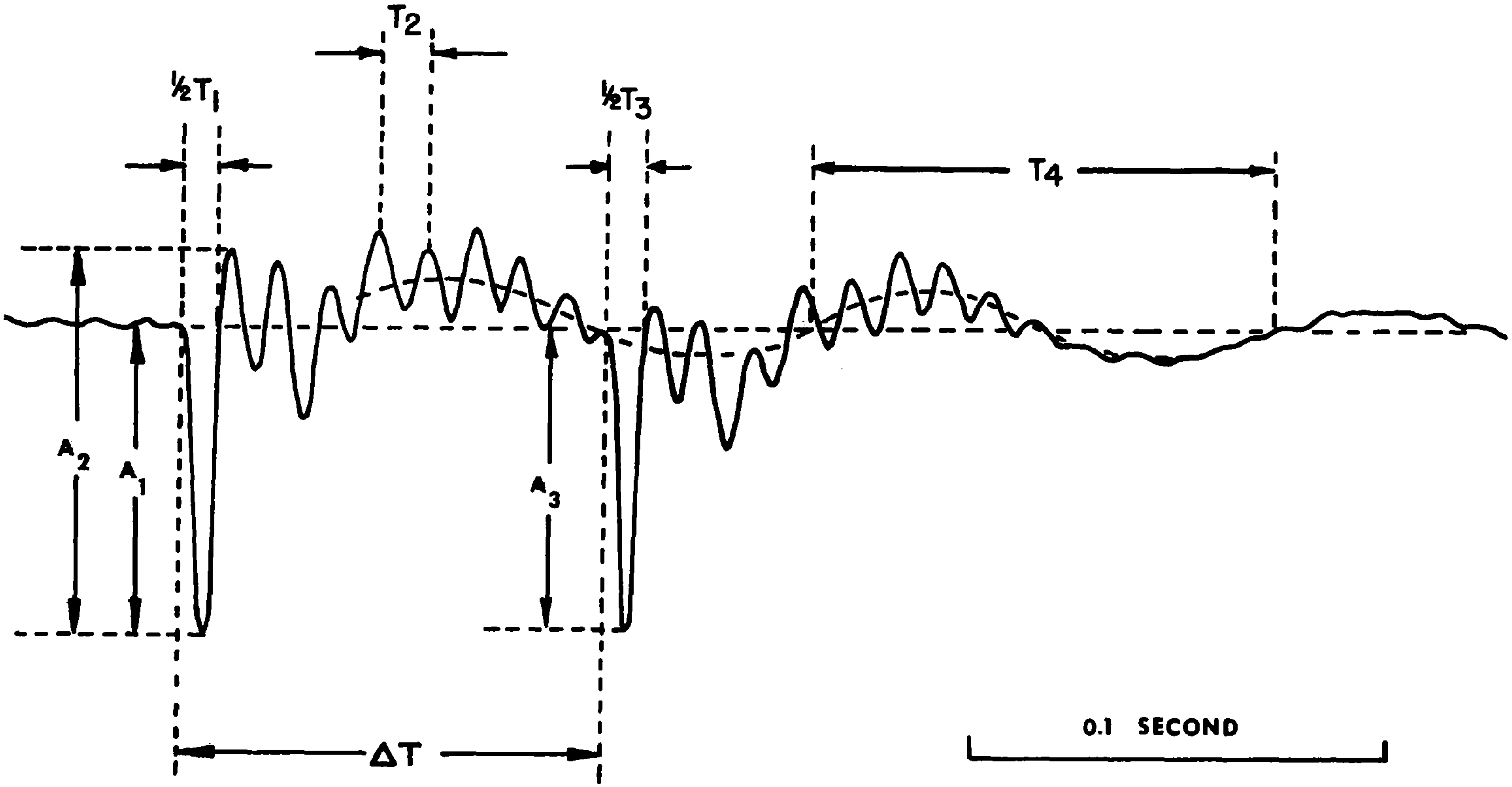

Figure 12. Hypothetical seismogram showing characteristic phases measured in the sonic boom study

G 3449

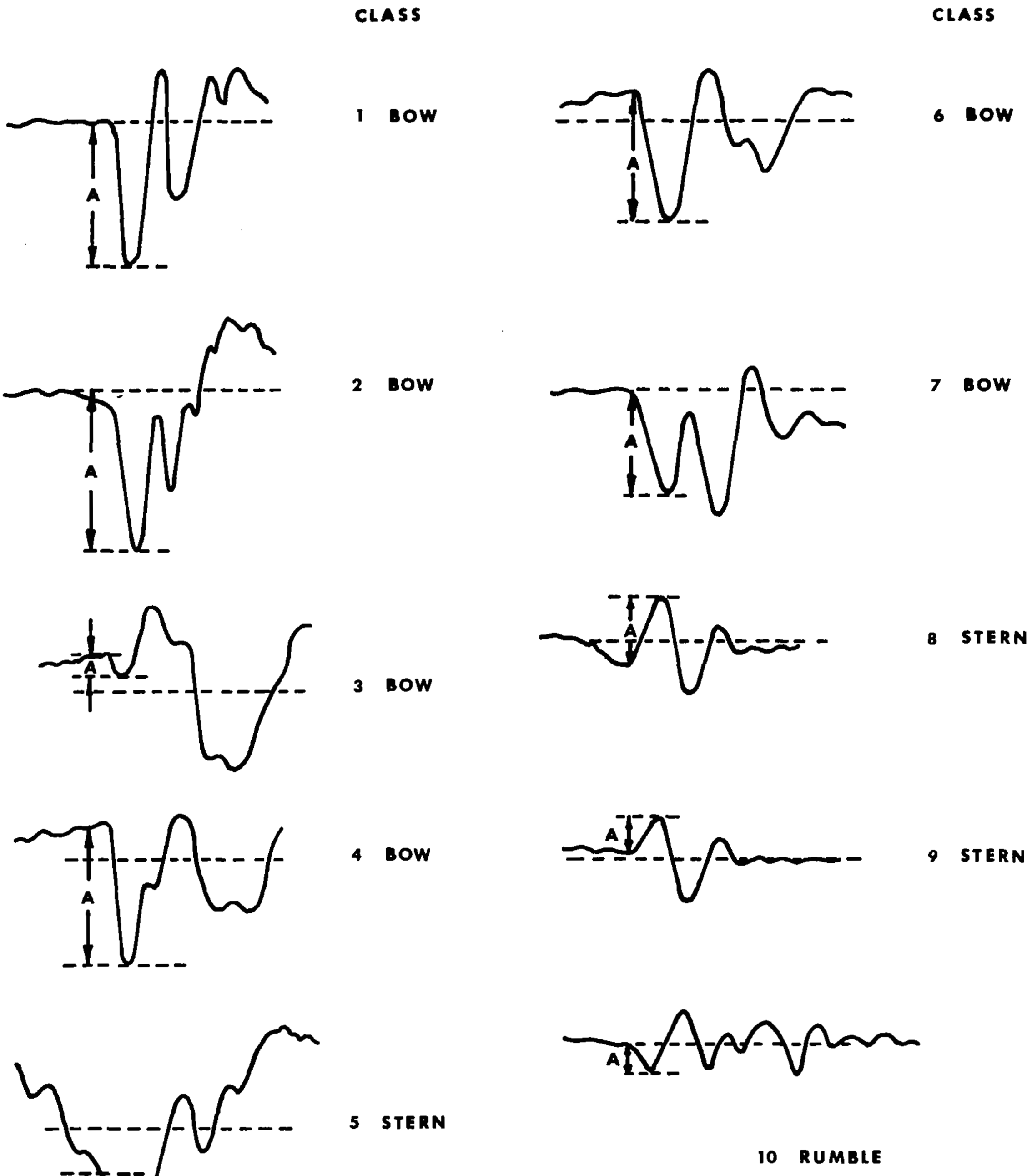

Figure 13. Schematic diagrams of the ten typical types of bow and stern velocity seismograms

G 3450

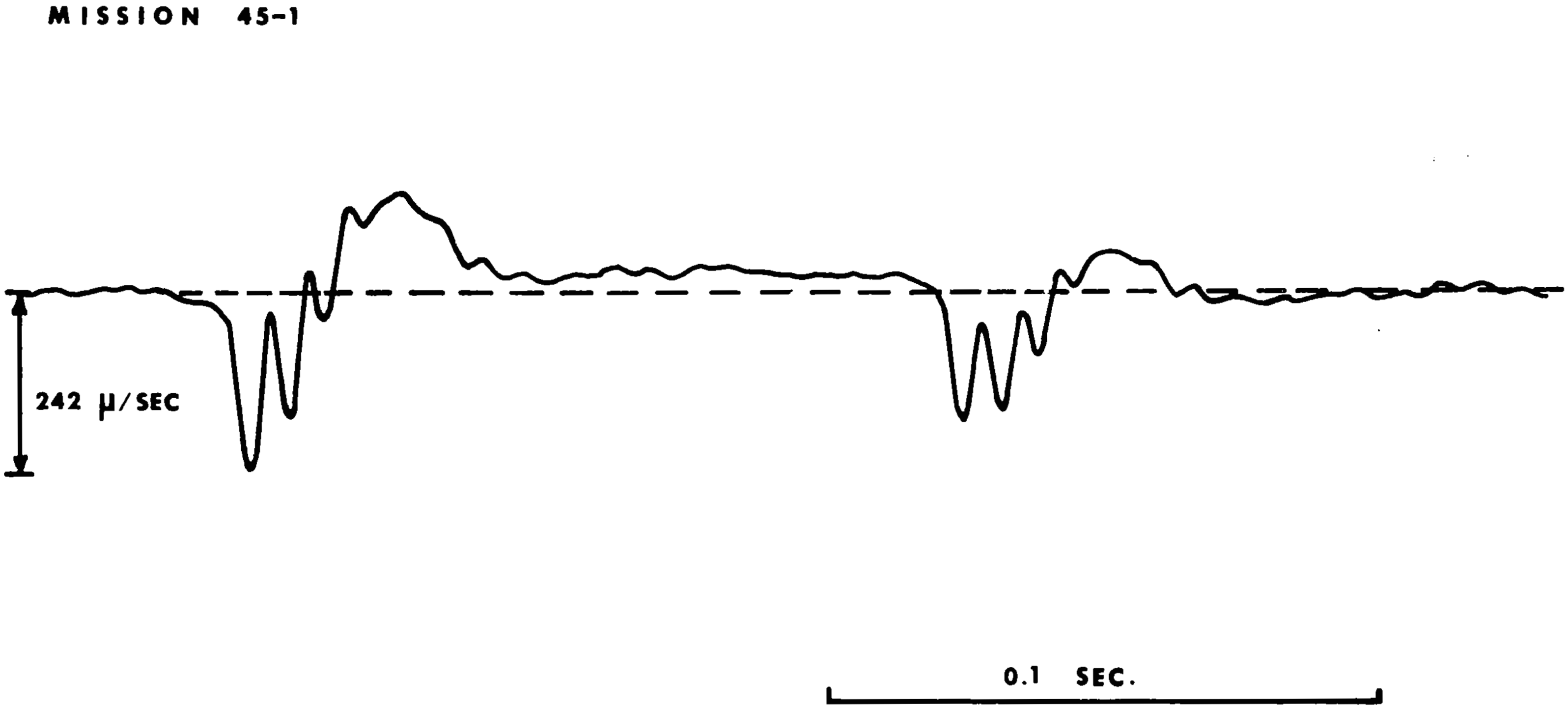

Figure 14. Seismogram recorded by a seismometer located on well-consolidated rock (position 5) at Edwards Air Force Base for a B-58 overflight

G 3451

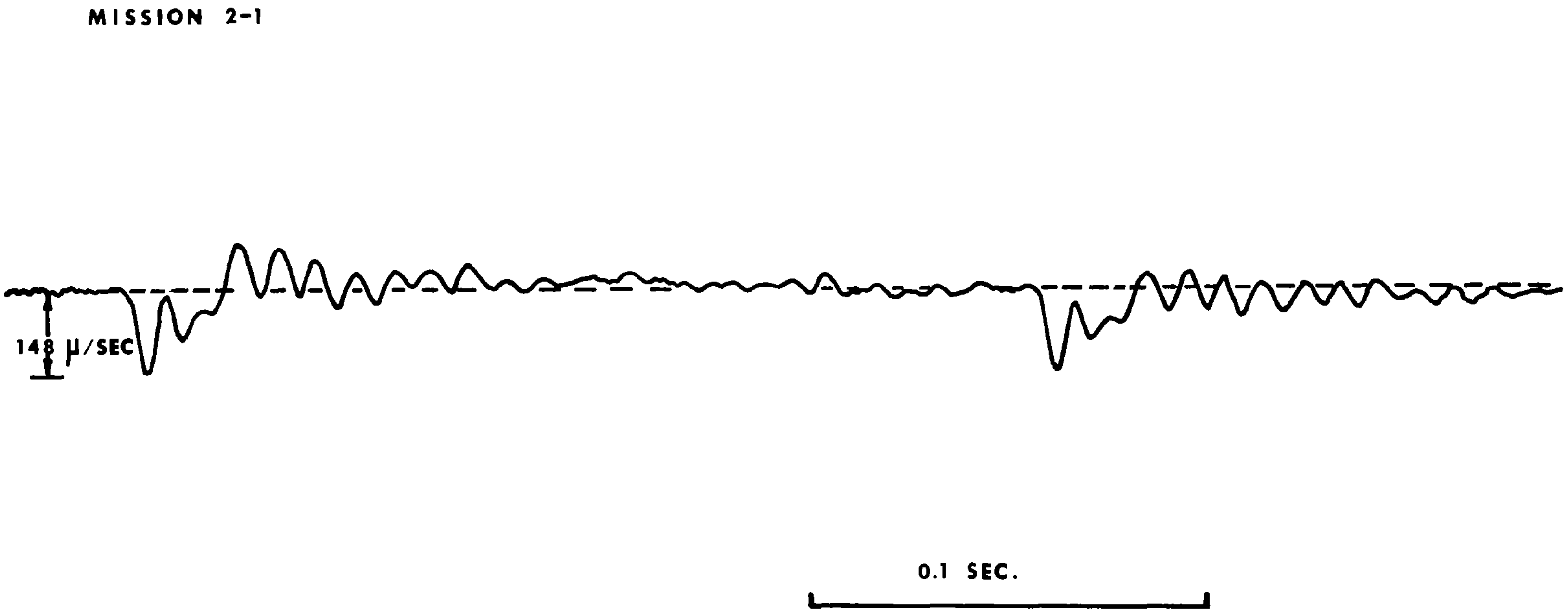

Figure 15. Seismogram recorded by a seismometer buried in the clay lake bed (position 1) at Edwards Air Force Base for an XB-70 overflight

G 3452

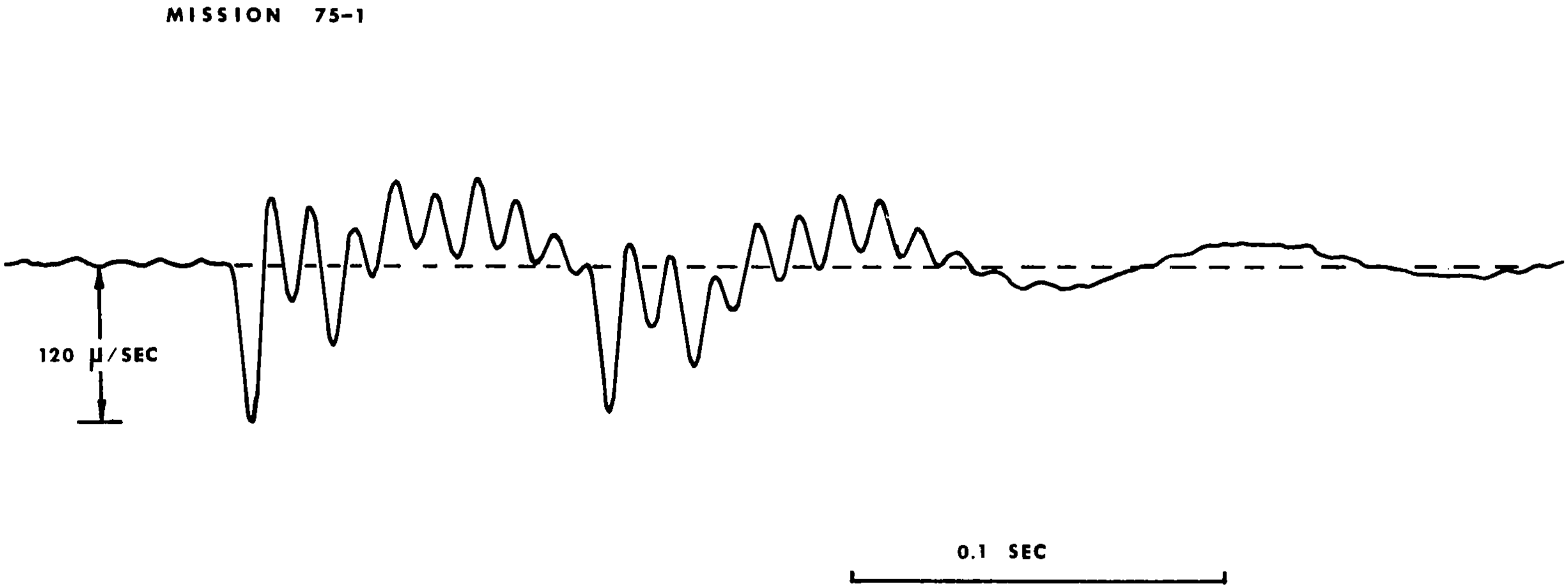

Figure 16. Seismogram recorded by a seismometer buried in the clay lake bed (position 4) at Edwards Air Force Base for an F-104 overflight

G 3453

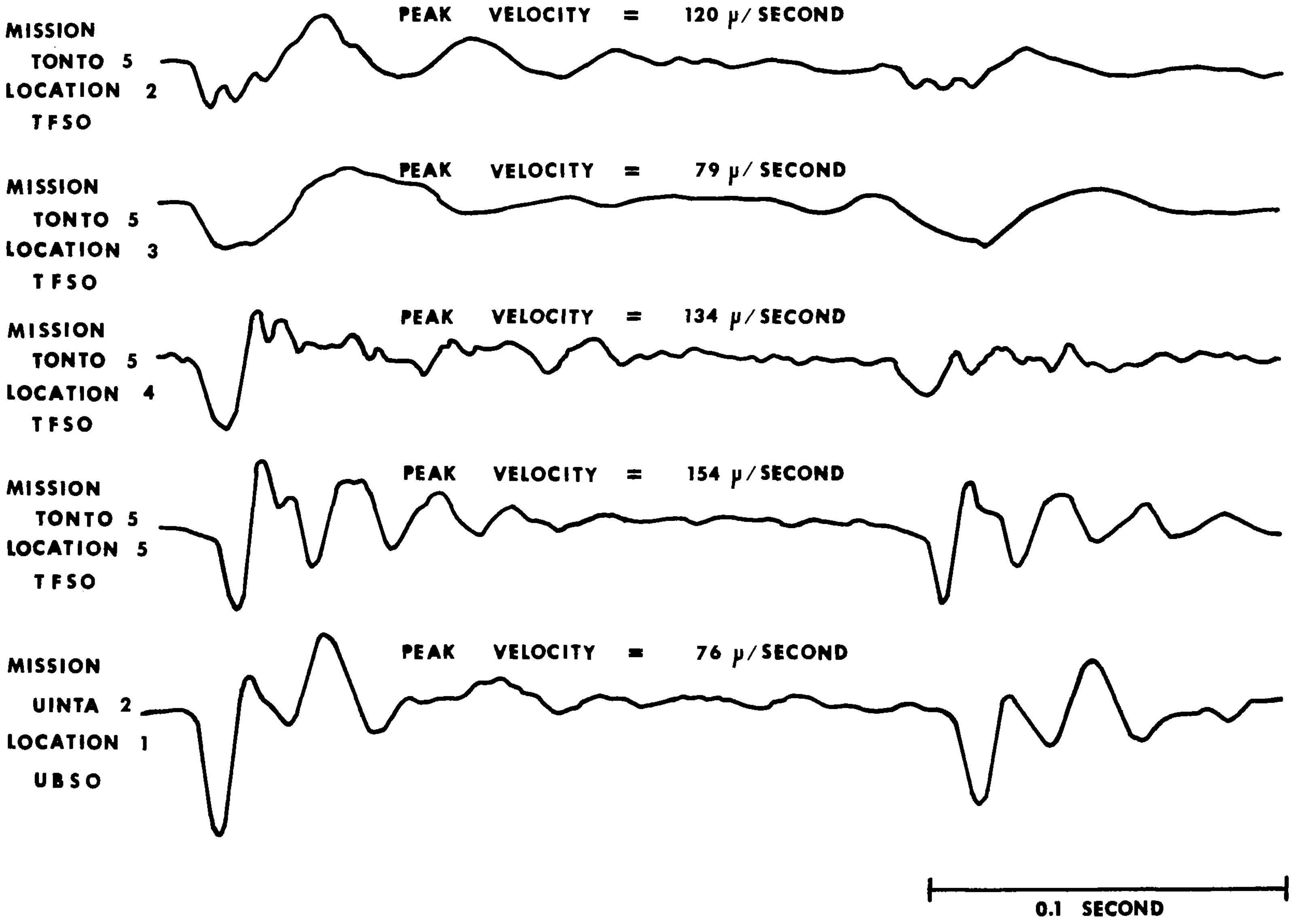

Figure 17. Seismograms recorded from similar B-58 overflights showing seismic signatures at the Tonto Forest and Uinta Basin observatories

G 3454

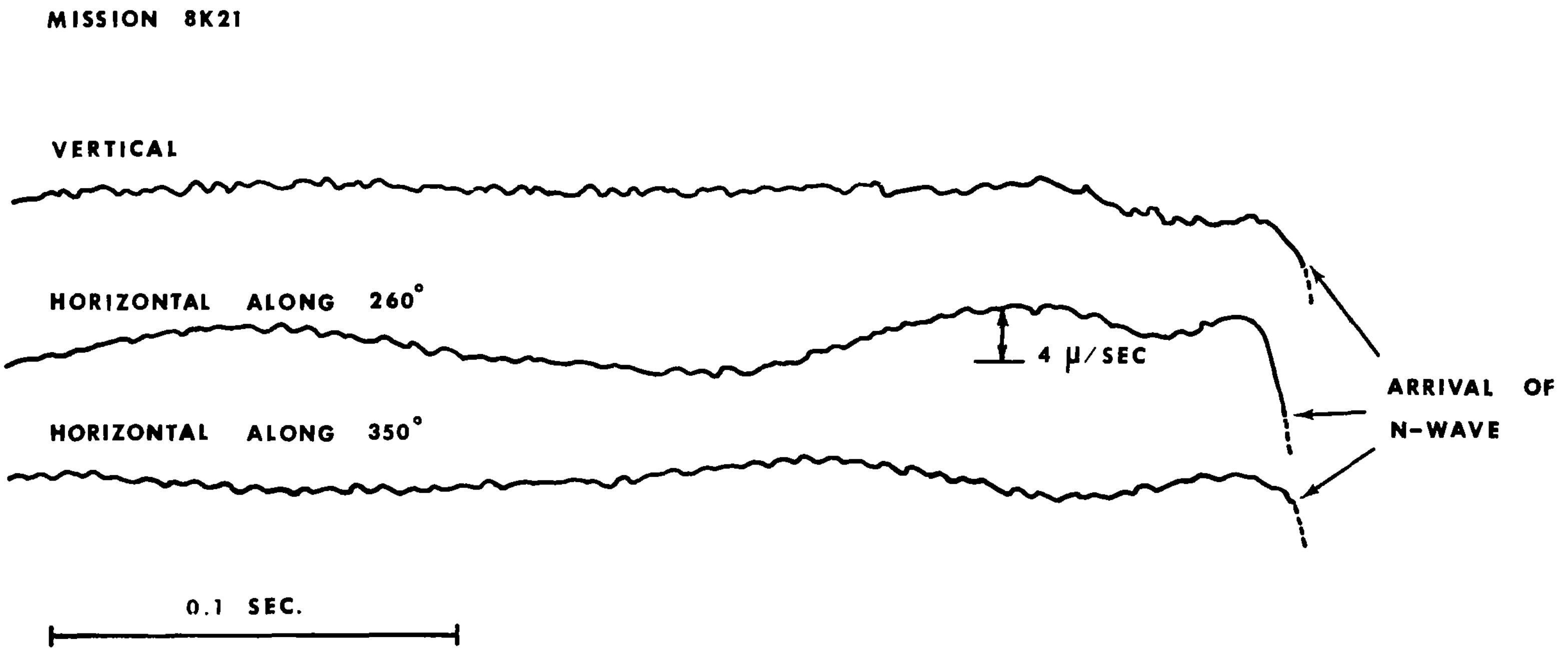

Figure 18. High sensitivity seismograms from a three-component seismograph at Edwards Air Force Base (position 1) showing a precursor to the arrival of the N-wave

G 3455

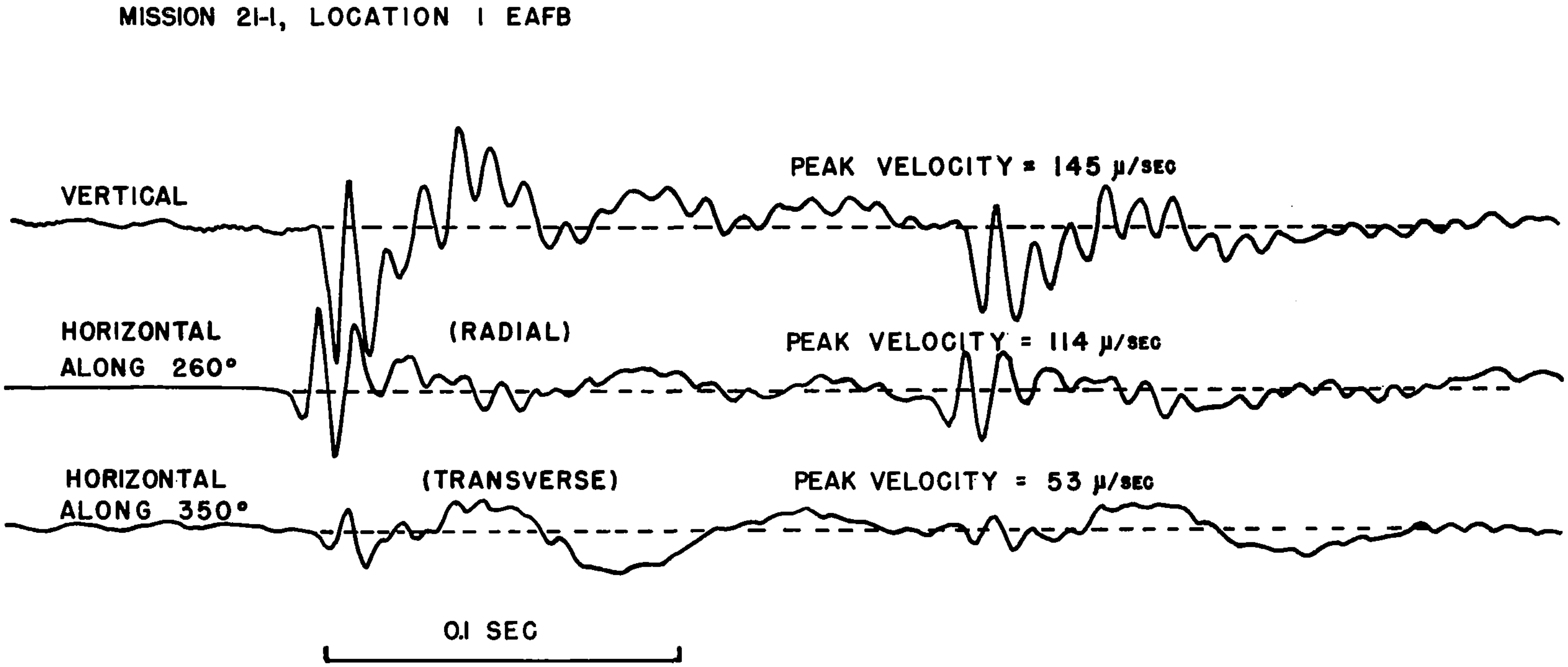

Figure 19. Typical three-component seismogram generated by the overflight of a B-58 aircraft at Edwards Air Force Base

G 3456

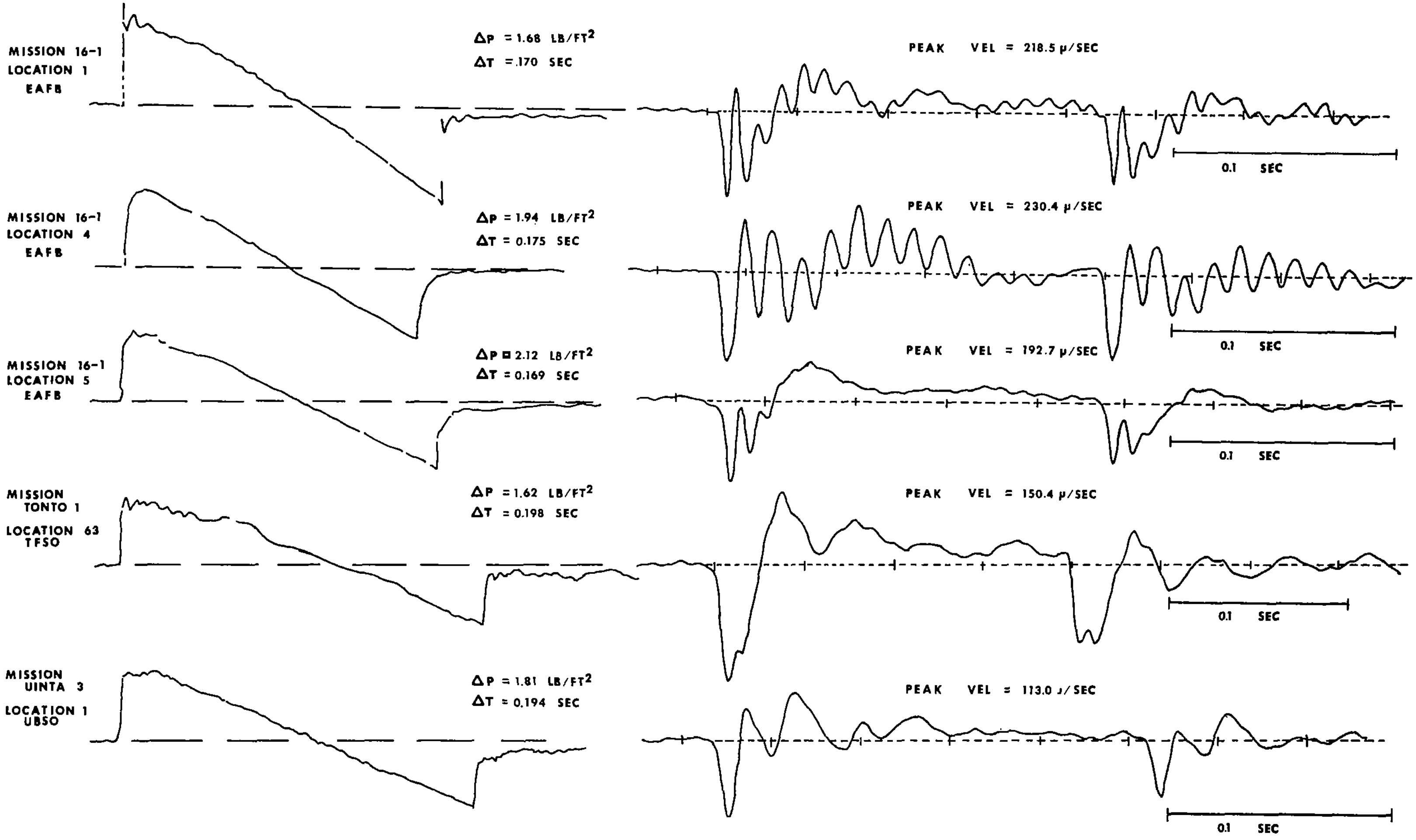

Figure 20. Seismograms and similar pressure signatures recorded at five locations for B-58 overflights showing the variations of the seismograms with geological environment

G 3457

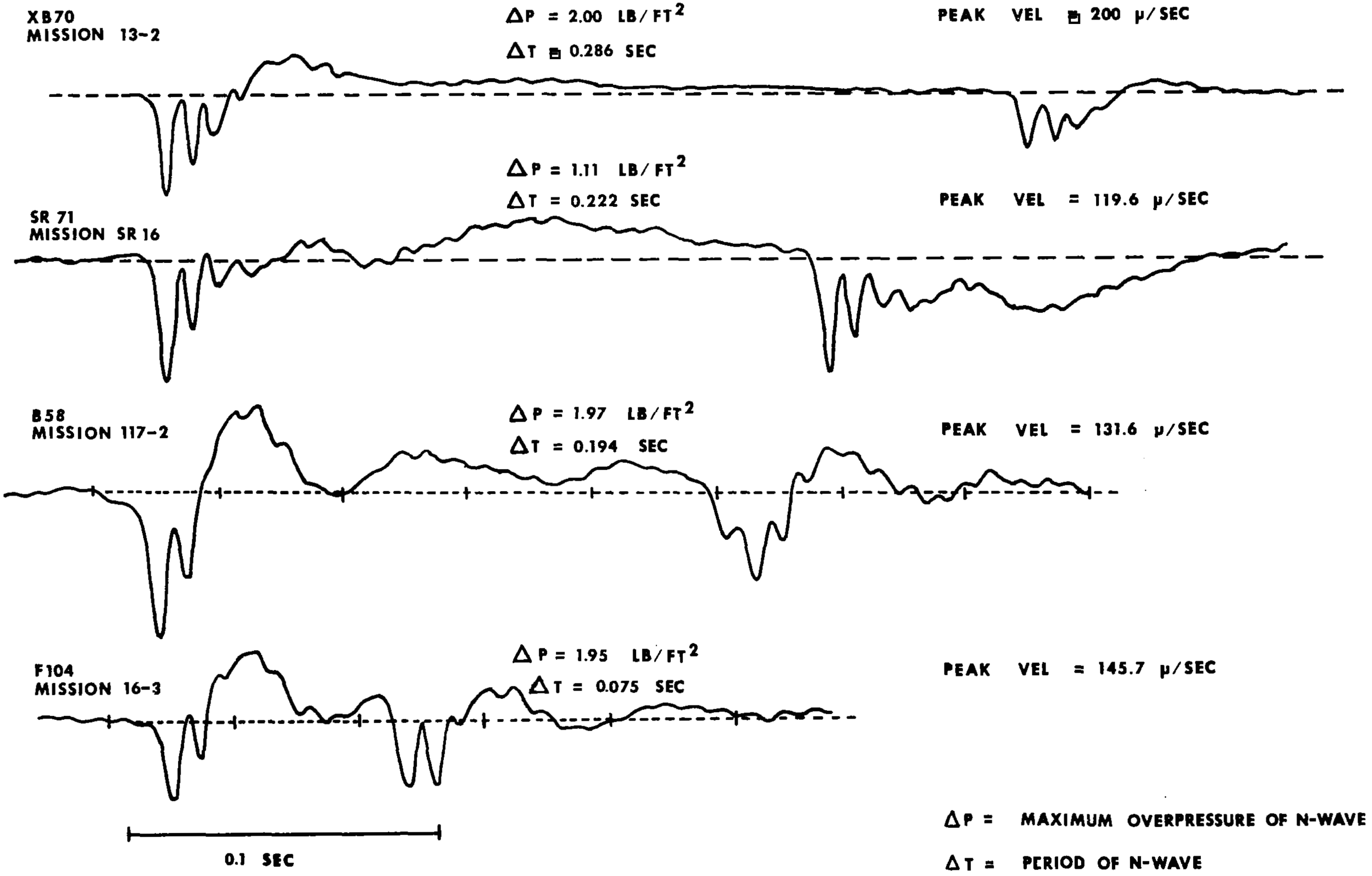

Figure 21. Seismograms produced by the overflights of four different types of aircraft recorded by a seismometer on well-consolidated rock (position 5) at Edwards Air Force Base

G 3458

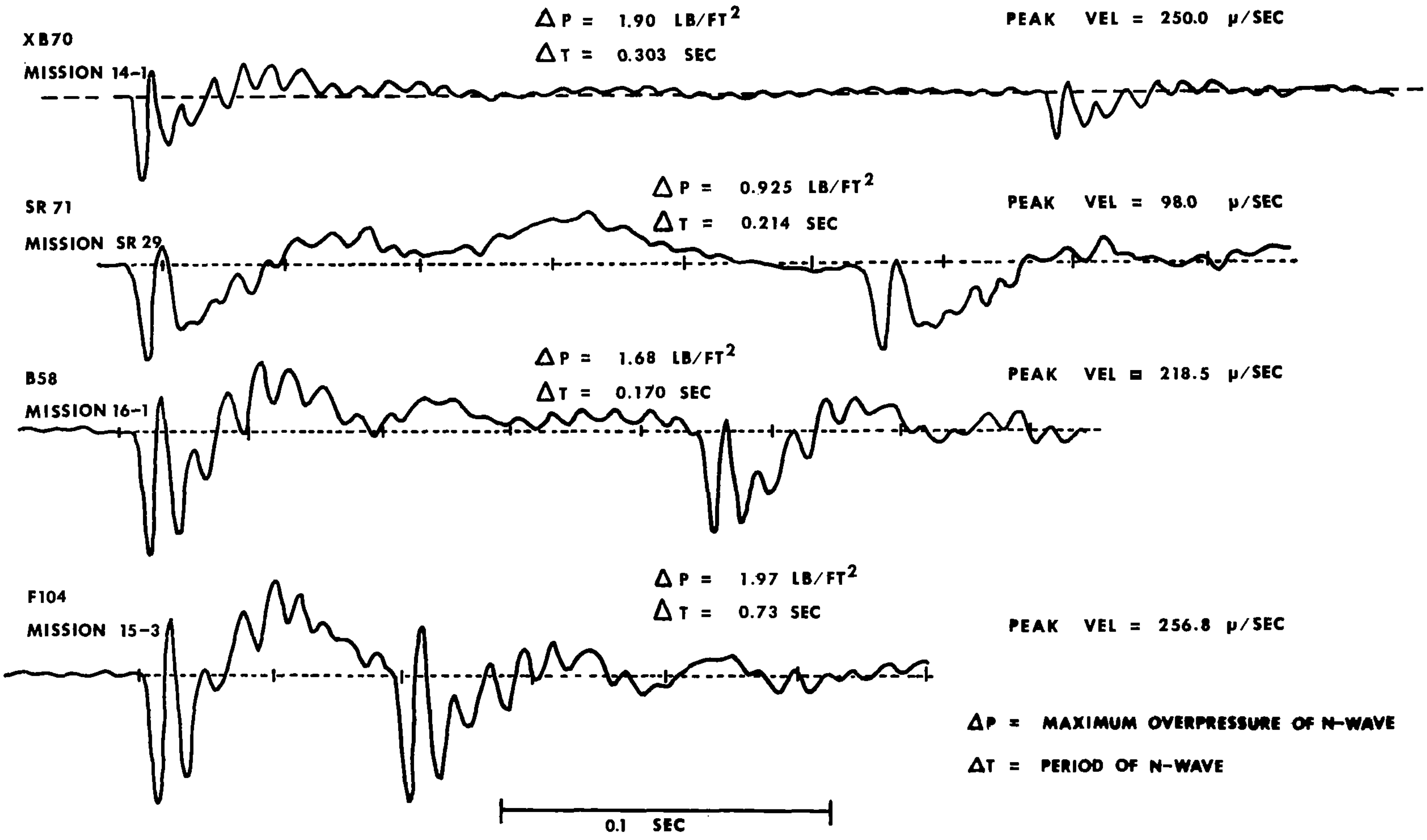

Figure 22. Seismograms produced by the overflights of four different types of aircraft recorded by a seismometer on a clay lake bed (position 1) at Edwards Air Force Base

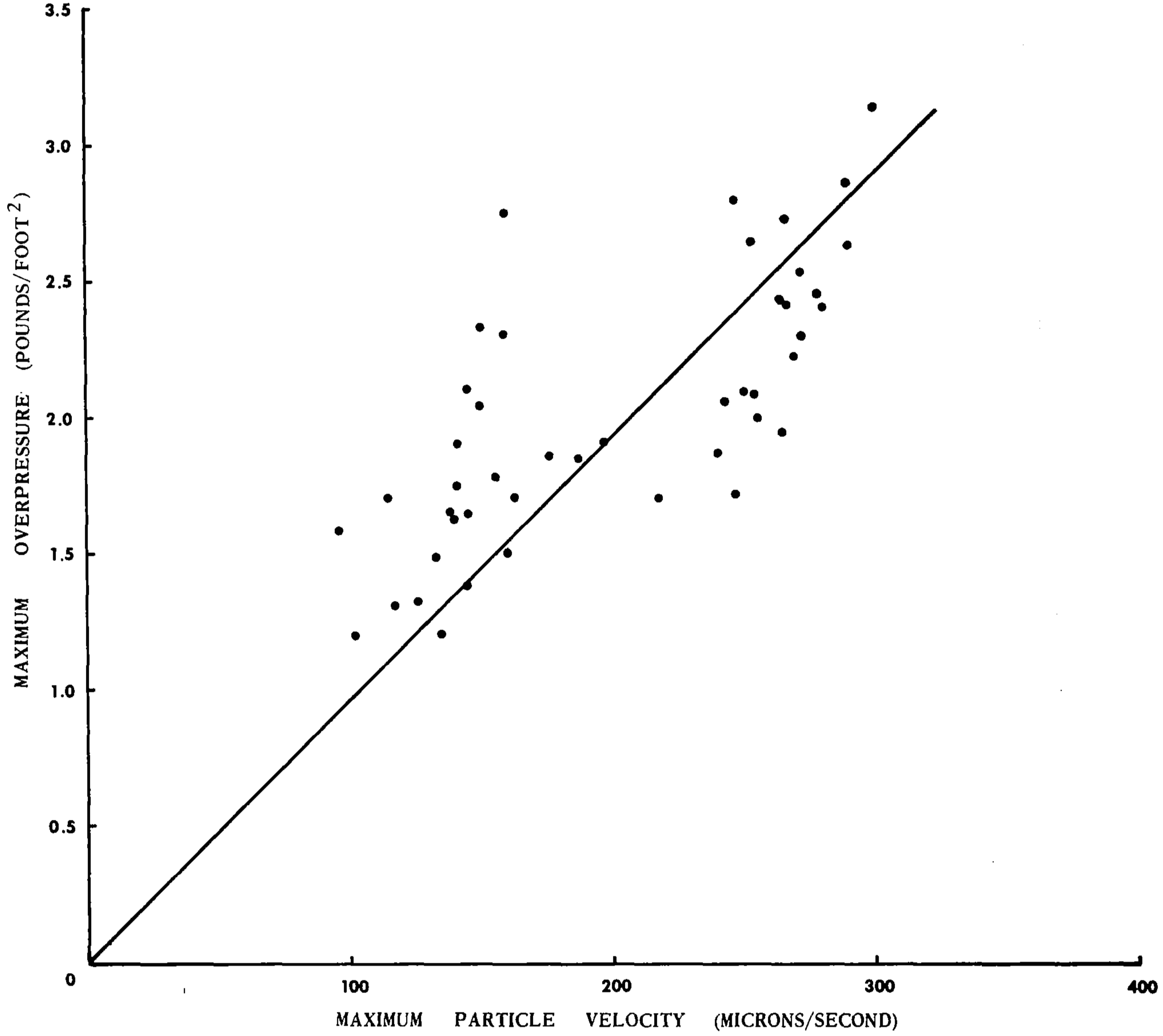

Figure 23. Relation of maximum overpressure for B-58 overflights to peak particle velocity observed on a vertical seismograph located on a clay lake bed (position 1) at Edwards Air Force Base

G 3460

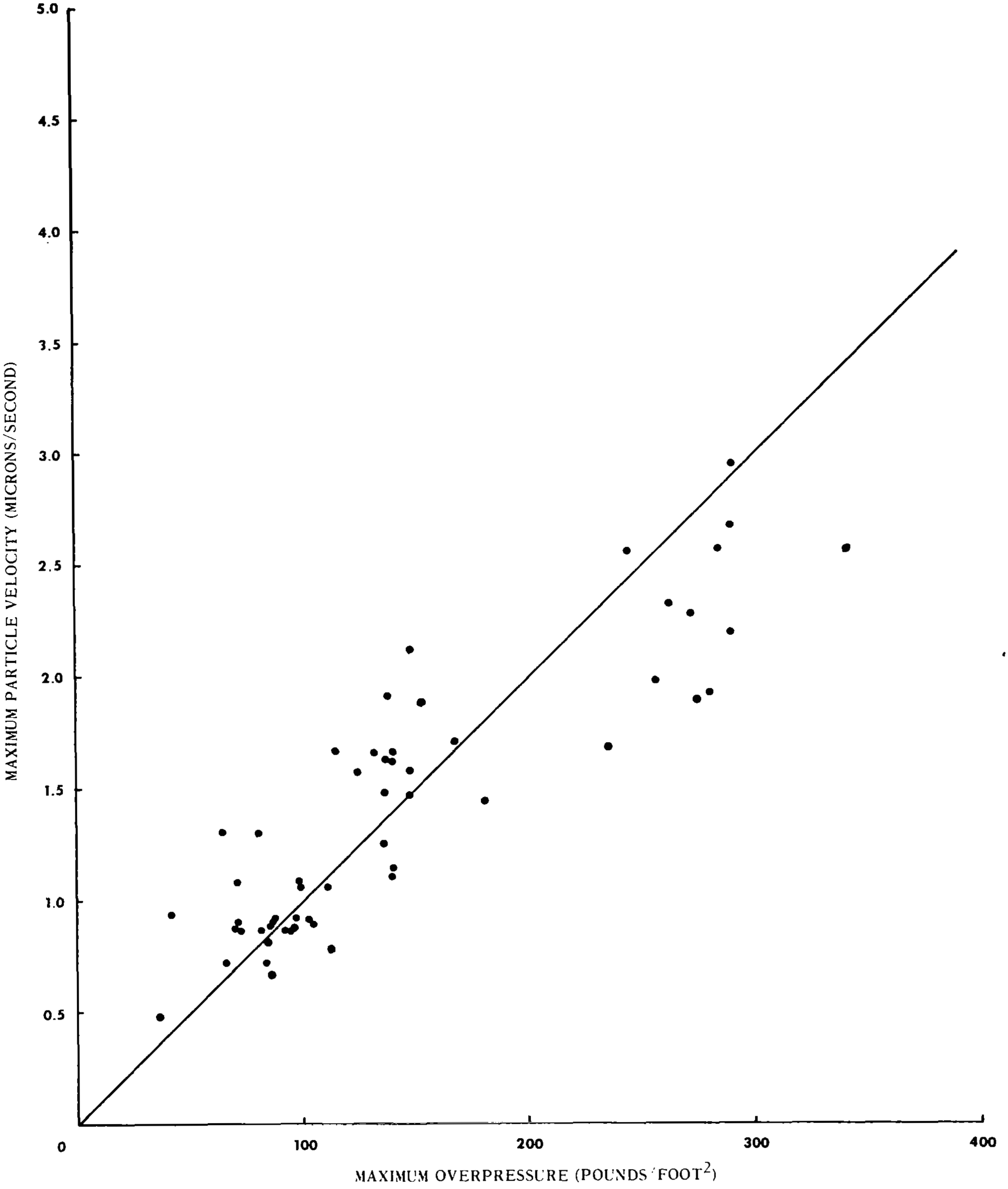

Figure 24. Relation of maximum overpressure for F-104 overflights to peak particle velocity observed on a vertical seismograph located on a clay lake bed (position 1) at Edwards Air Force Base

G 3461

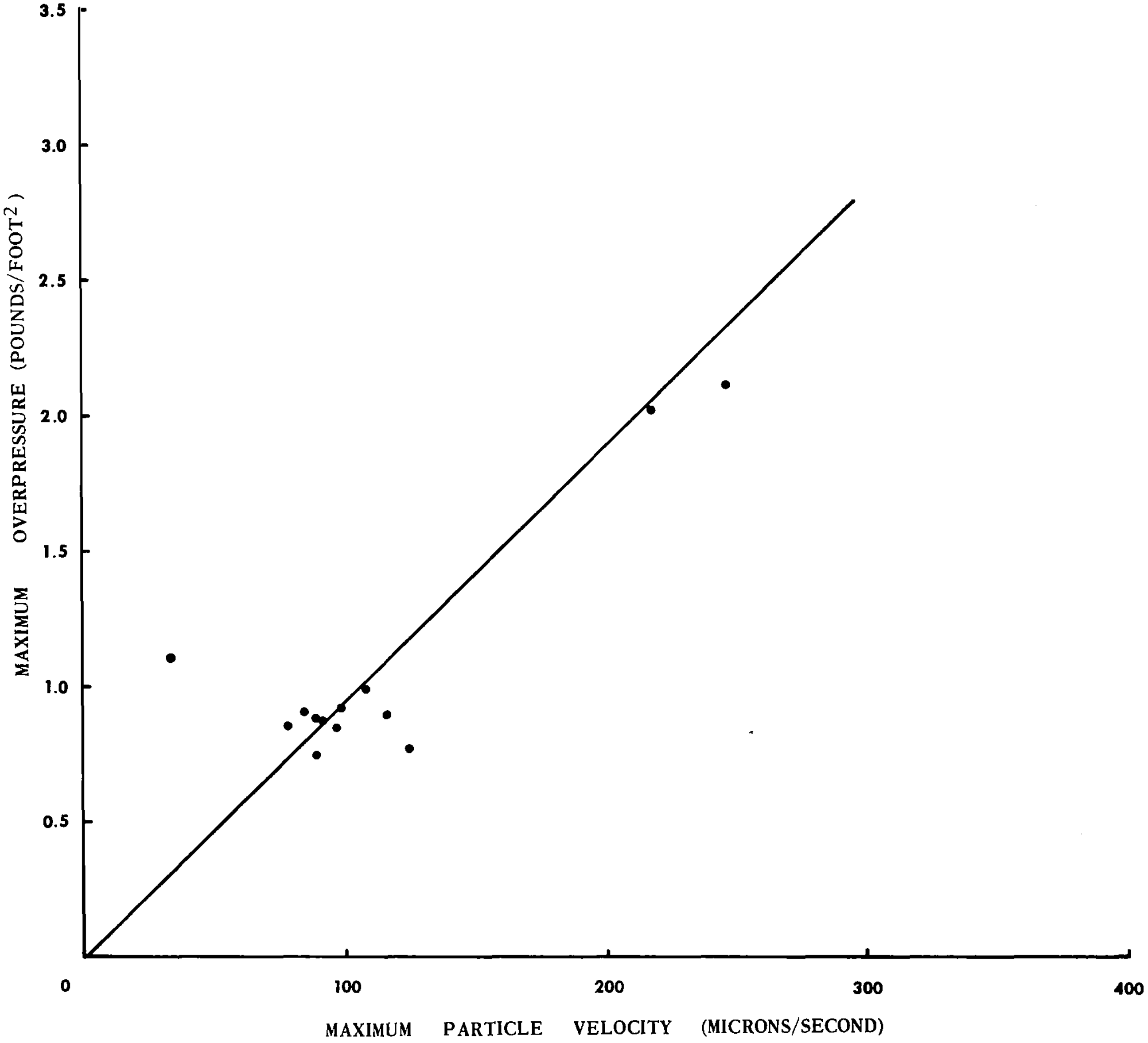

Figure 25. Relation of maximum overpressure for SR-71 overflights to peak particle velocity observed on a vertical seismograph located on a clay lake bed (position 1) at Edwards Air Force Base

G 3462

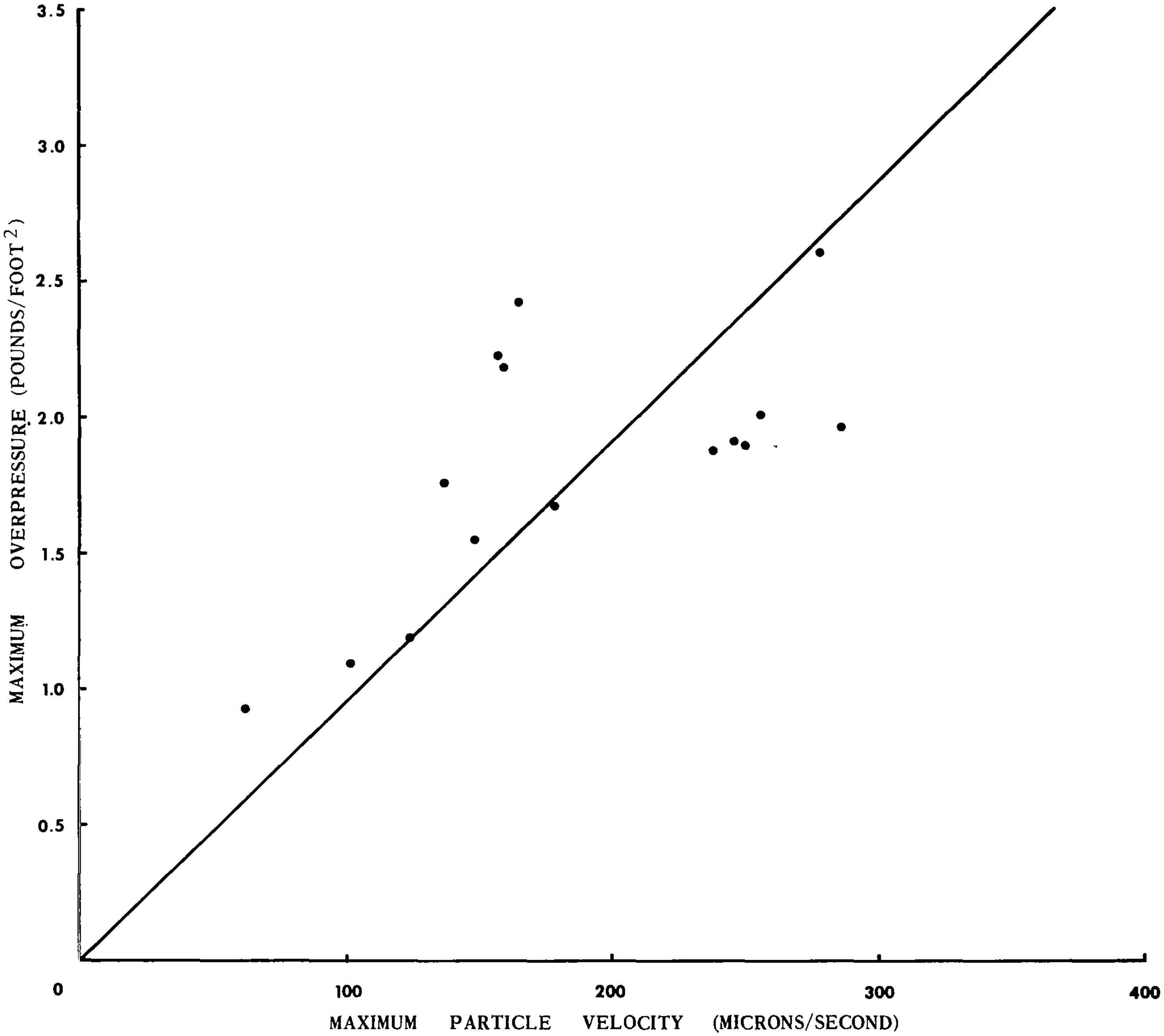

Figure 26. Relation of maximum overpressure for XB-70 overflights to peak particle velocity observed on a vertical seismograph located on a clay lake bed (position 1) at Edwards Air Force Base

G 3463

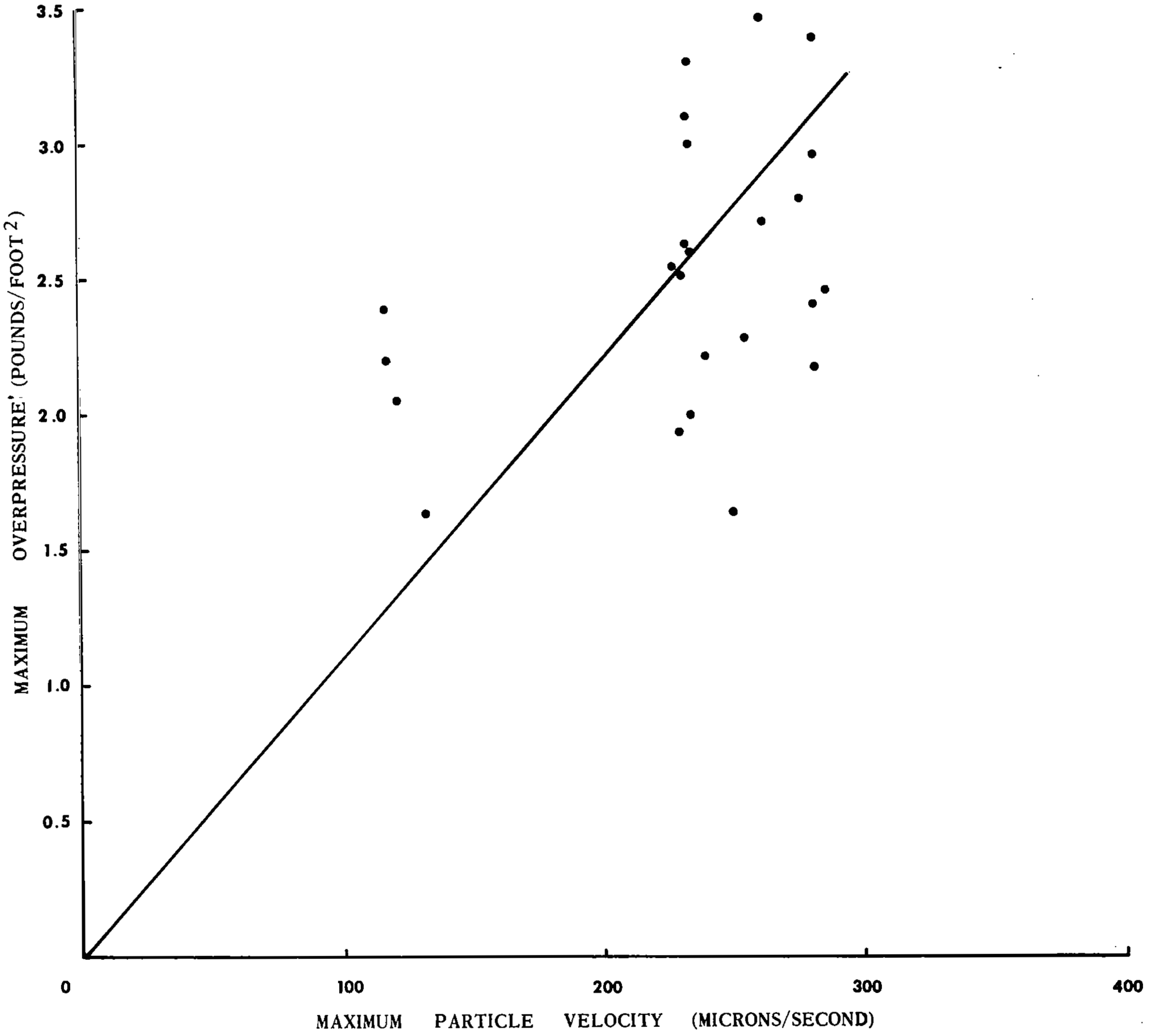

Figure 27. Relation of maximum overpressure for B-58 overflights to peak particle velocity observed on a vertical seismograph located on a clay lake bed (position 4) at Edwards Air Force Base

G 3464

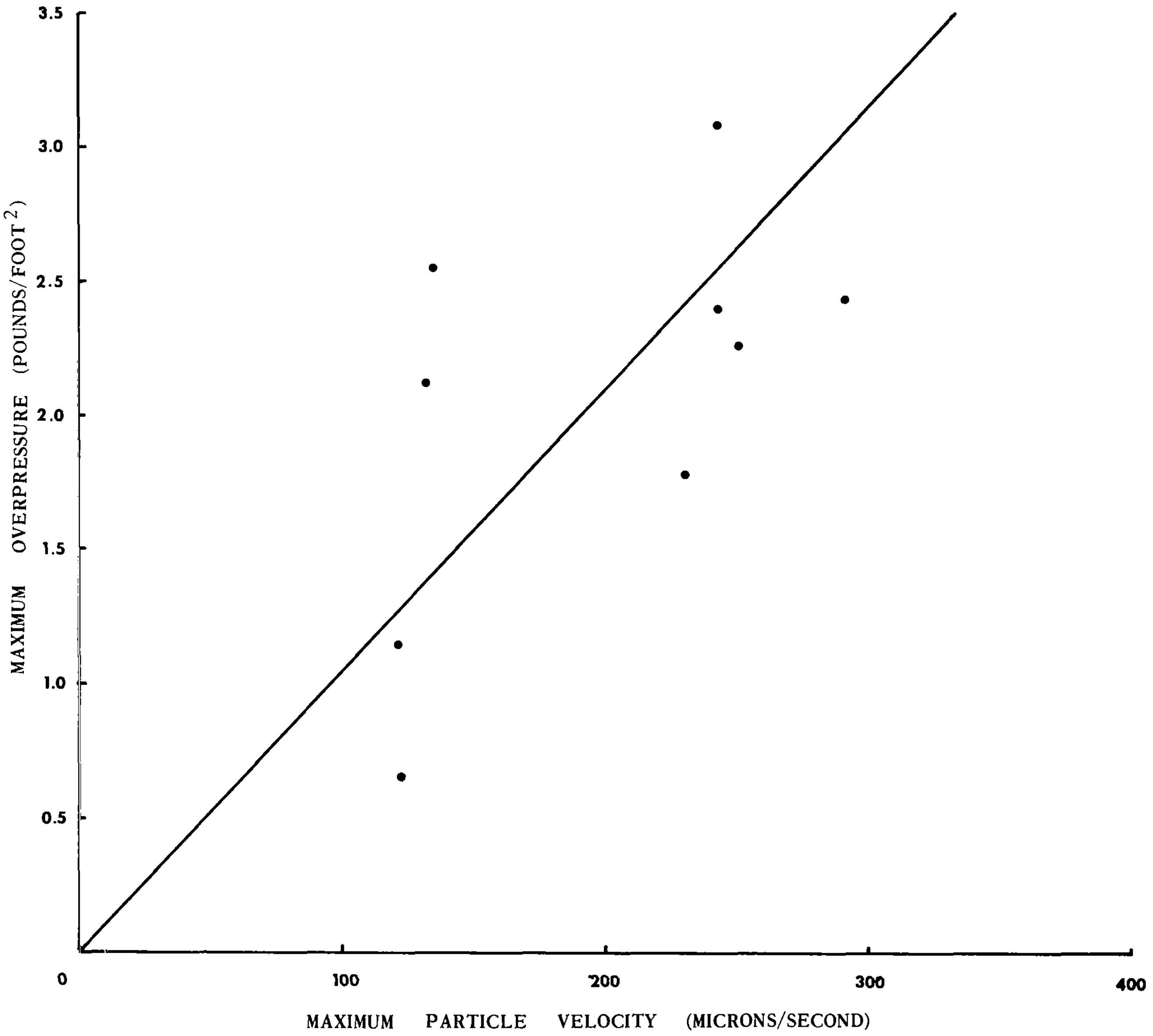

Figure 28. Relation of maximum overpressure for F-104 overflights to peak particle velocity observed on a vertical seismograph located on a clay lake bed (position 4) at Edwards Air Force Base

G 3465

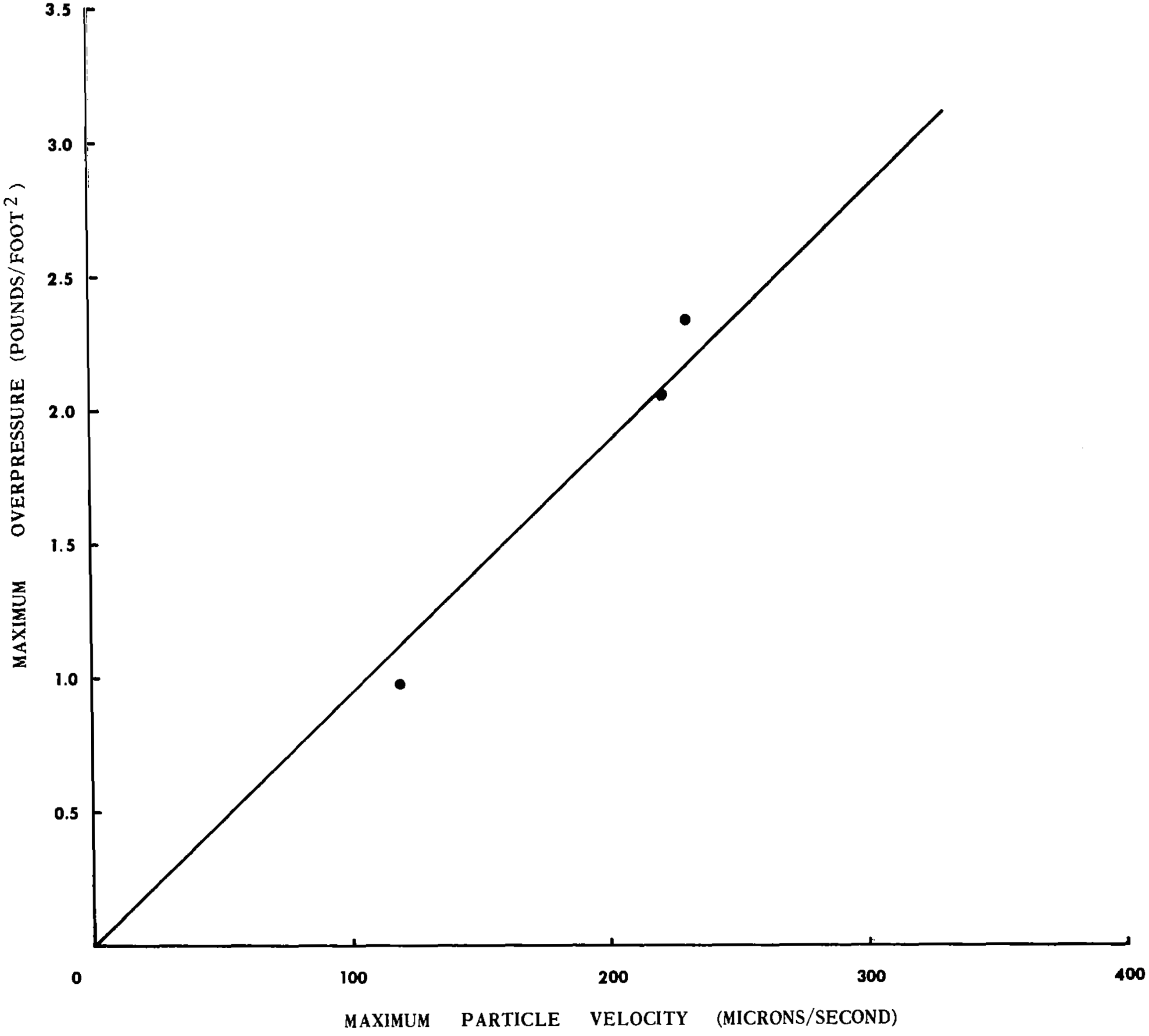

Figure 29. Relation of maximum overpressure for SR-71 overflights to peak particle velocity observed on a vertical seismograph located on a clay lake bed (position 4) at Edwards Air Force Base

G 3466

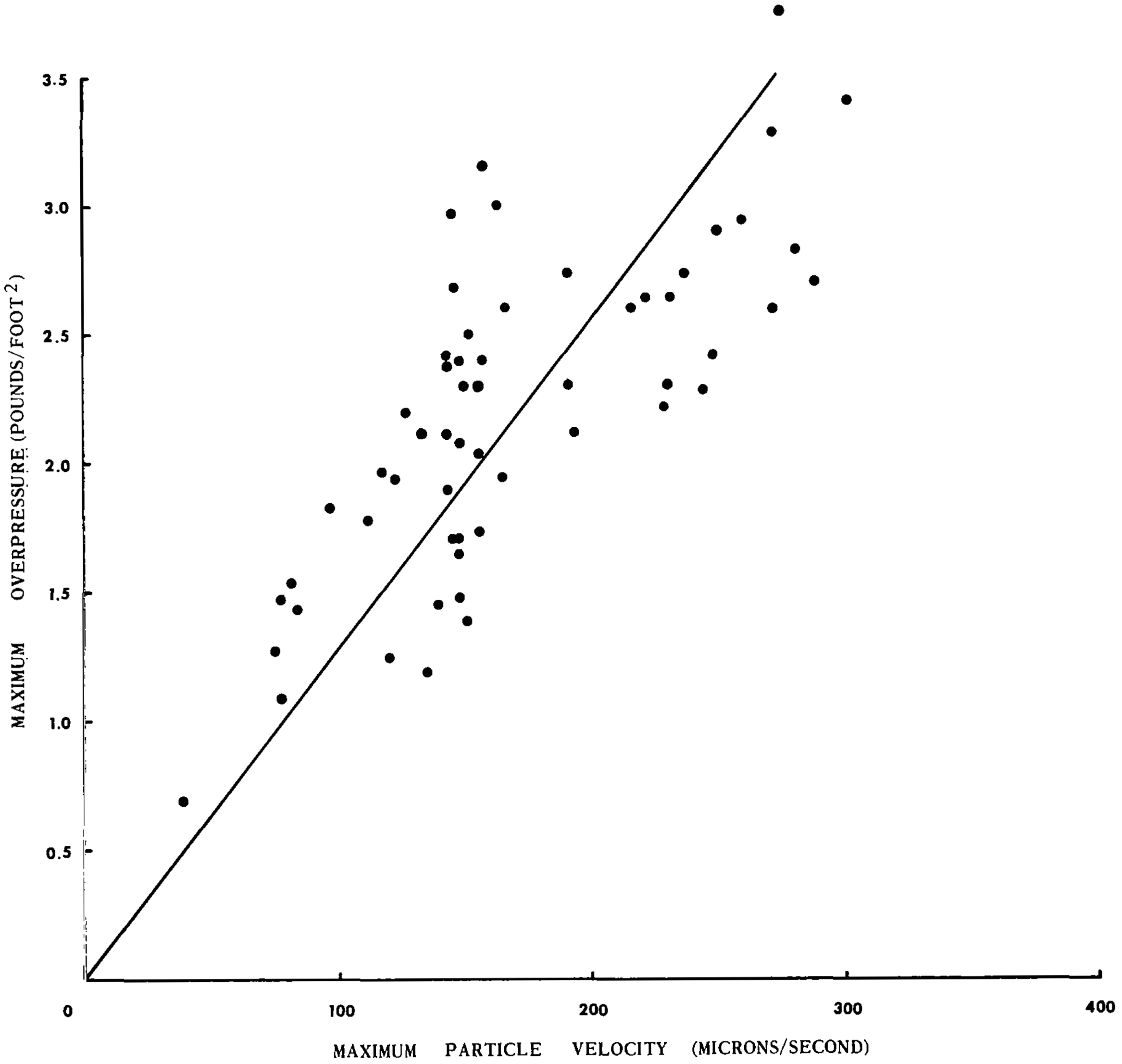

Figure 30. Relation of maximum overpressure for B-58 overflights to peak particle velocity observed on a vertical seismograph located on a well-consolidated rock outcrop (position 5) at Edwards Air Force Base

G 3467.

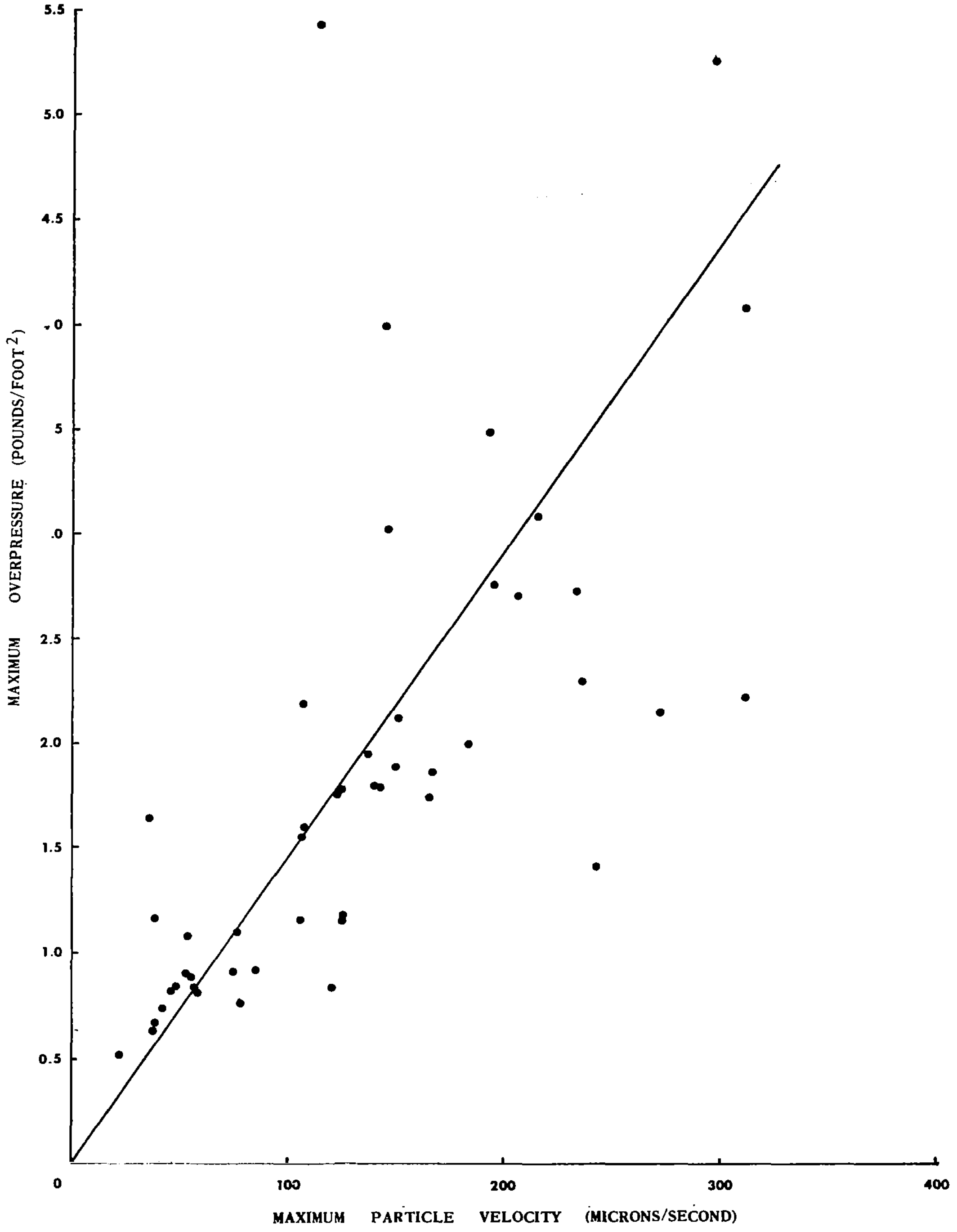

Figure 31. Relation of maximum overpressure for F-104 overflights to peak particle velocity observed on a vertical seismograph located on a well-consolidated rock outcrop (position 5) at Edwards Air Force Base

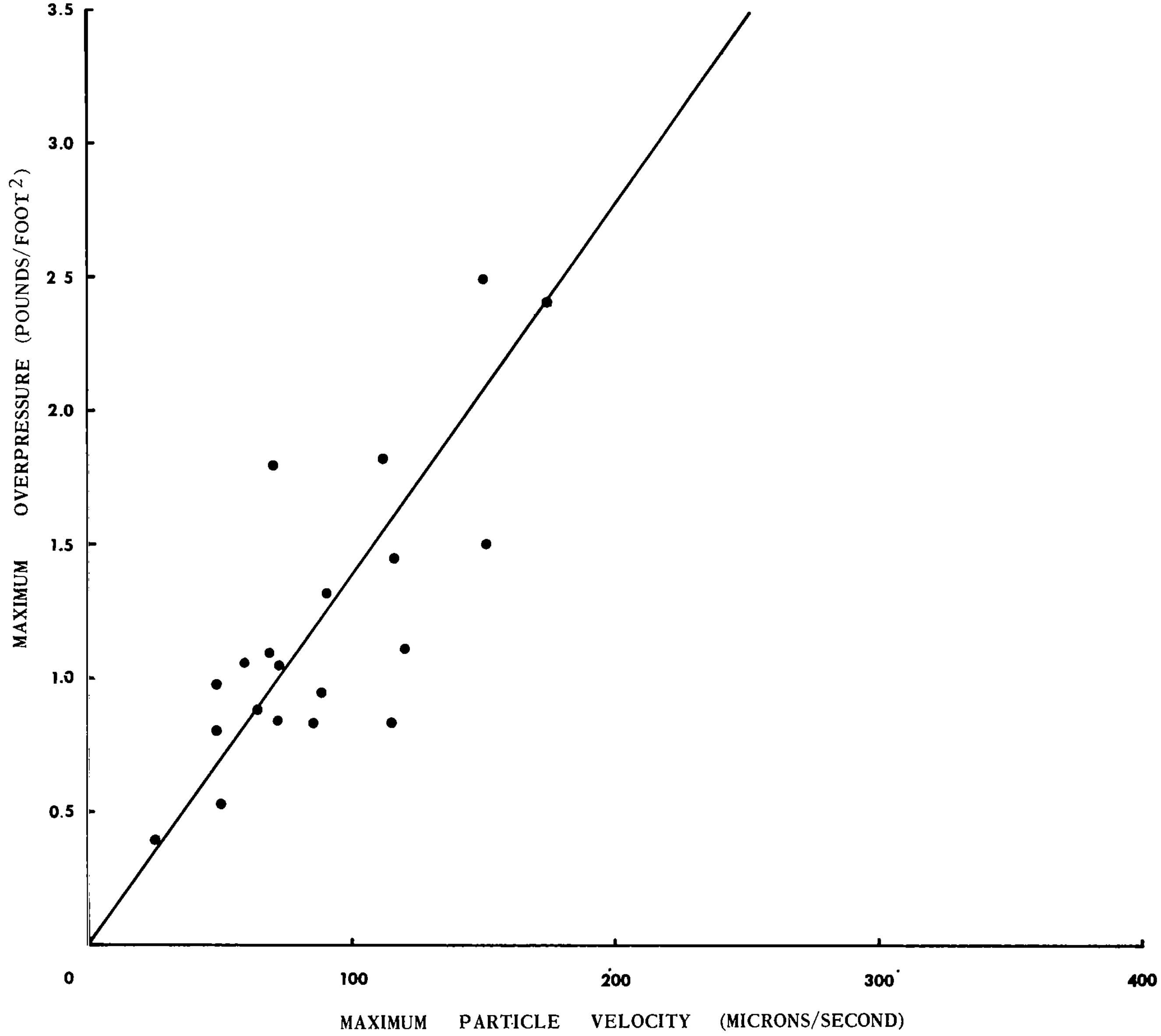

Figure 32. Relation of maximum overpressure for SR-71 overflights to peak particle velocity observed on a vertical seismograph located on a well-consolidated rock outcrop (position 5) at Edwards Air Force Base

G 3469

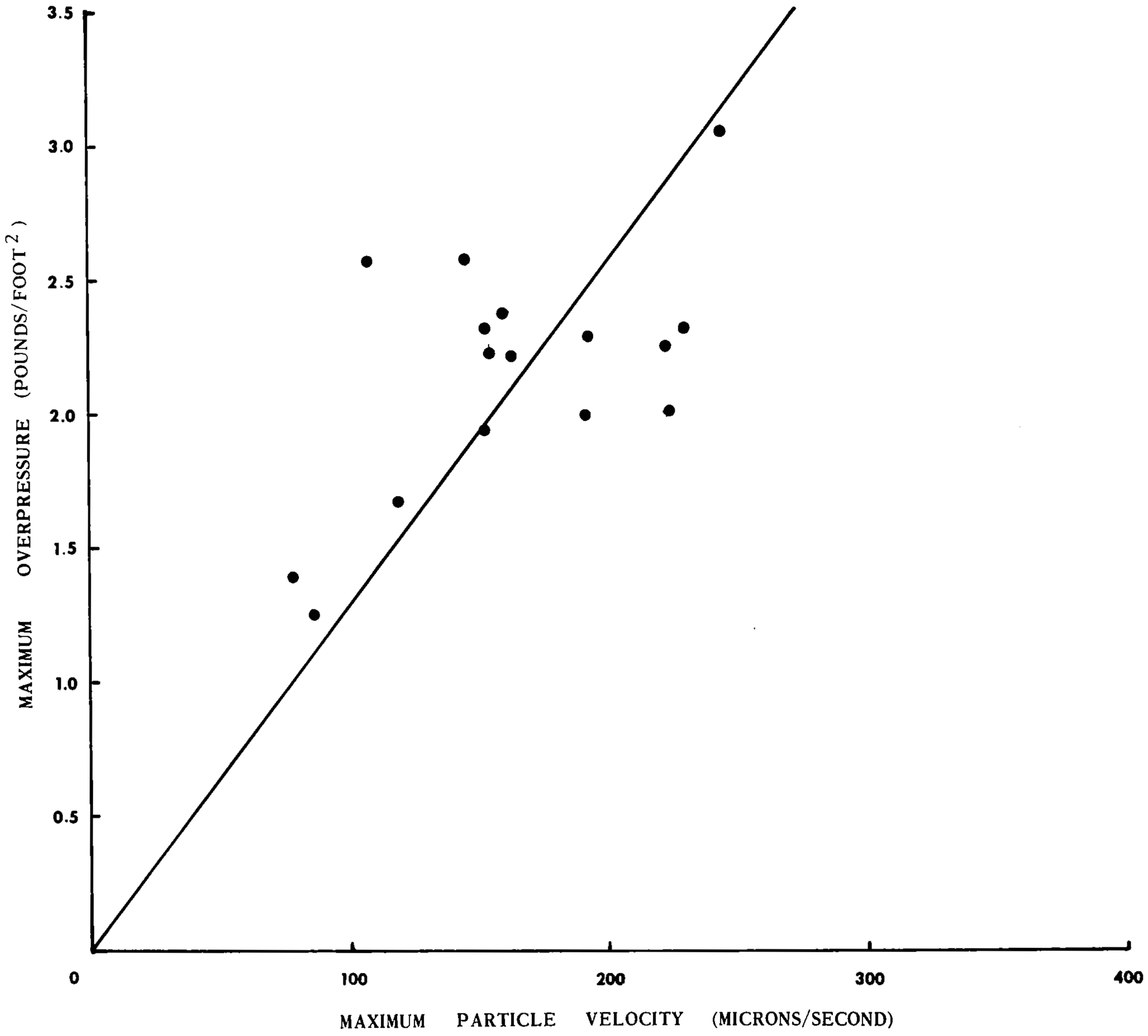

Figure 33. Relation of maximum overpressure for XB-70 overflights to peak particle velocity observed on a vertical seismograph located on a well-consolidated rock outcrop (position 5) at Edwards Air Force Base

G 3470

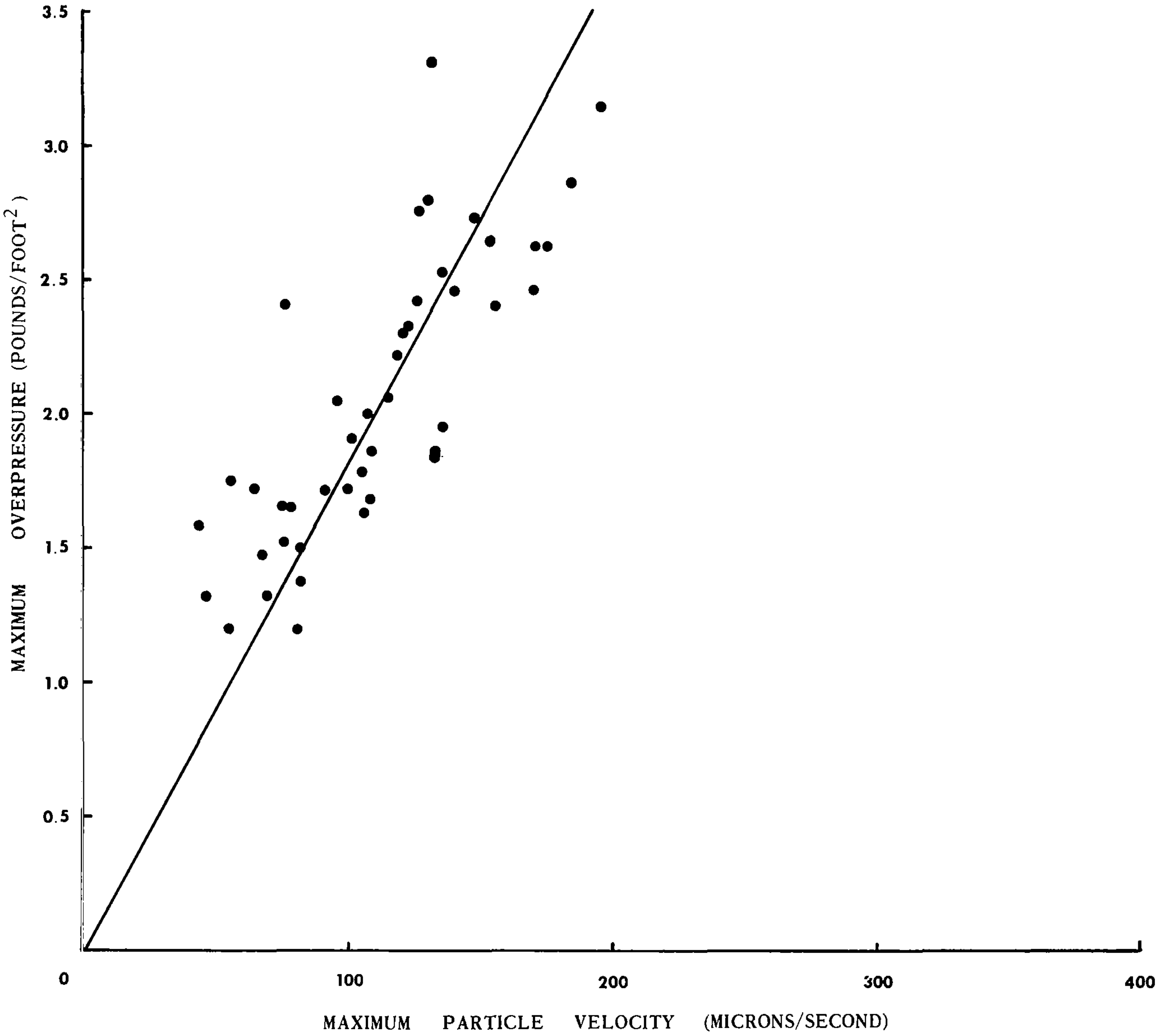

Figure 34. Relation of maximum overpressure for B-58 overflights to peak particle velocity observed on a seismograph oriented radial to the flight track and located on a clay lake bed (position 1) at Edwards Air Force Base

G 3471

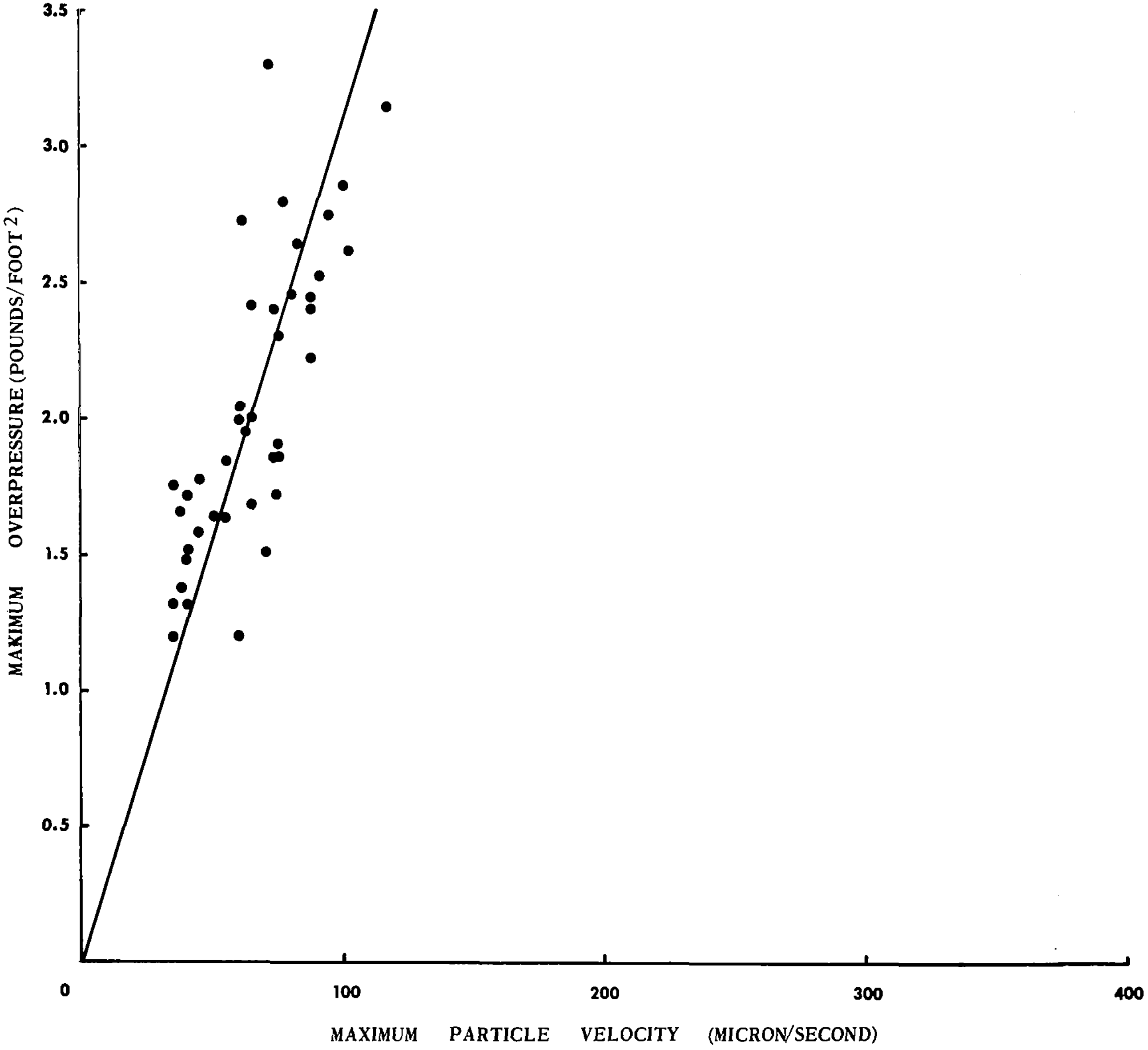

Figure 35. Relation of maximum overpressure for B-58 overflights to peak particle velocity observed on a seismograph oriented transverse to the flight track and located on a clay lake bed (position 1) at Edwards Air Force Base

G 3472

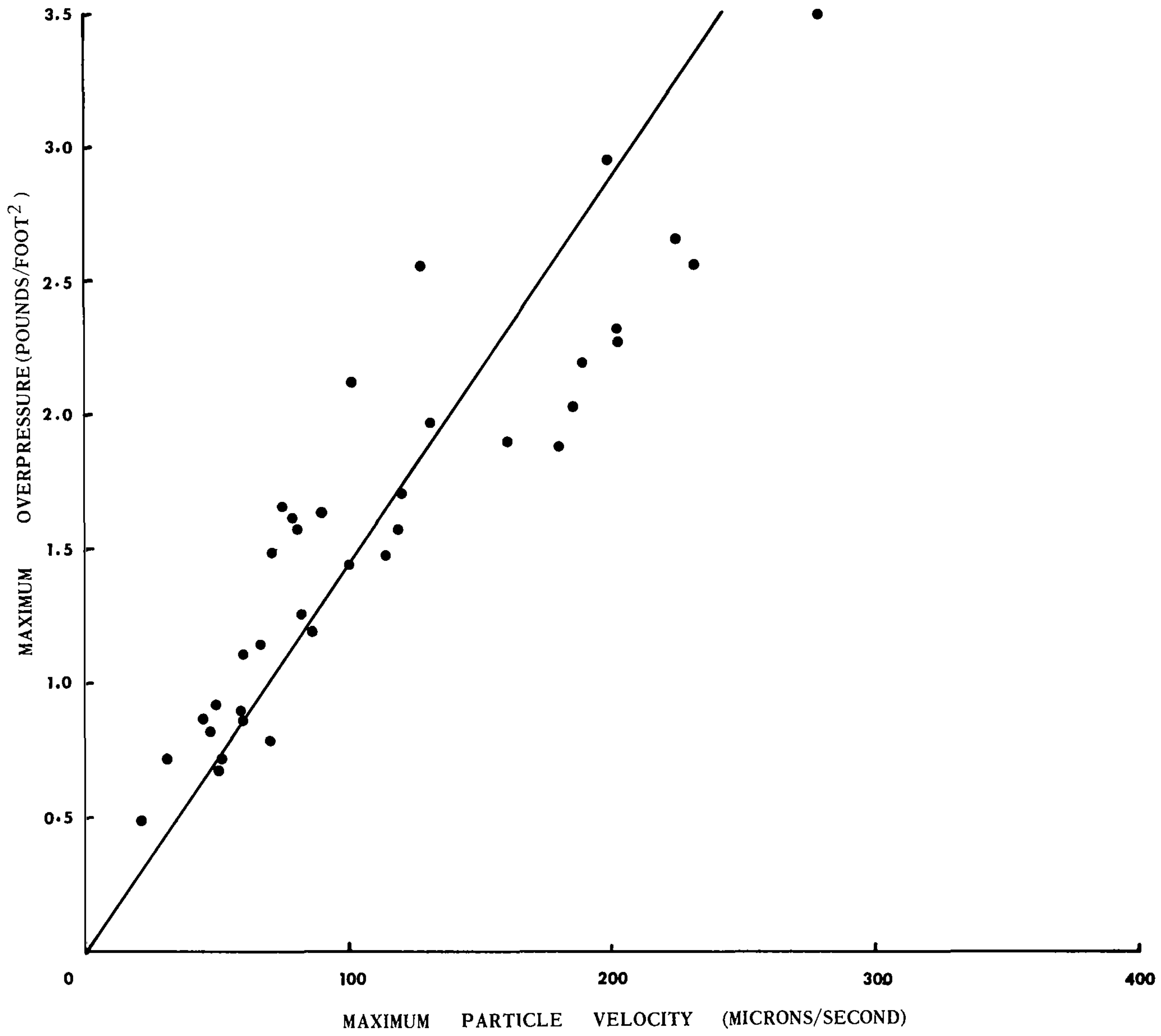

Figure 36. Relation of maximum overpressure for F-104 overflights to peak particle velocity observed on a seismograph oriented radial to the flight track and located on a clay lake bed (position 1) at Edwards Air Force Base

G 3473

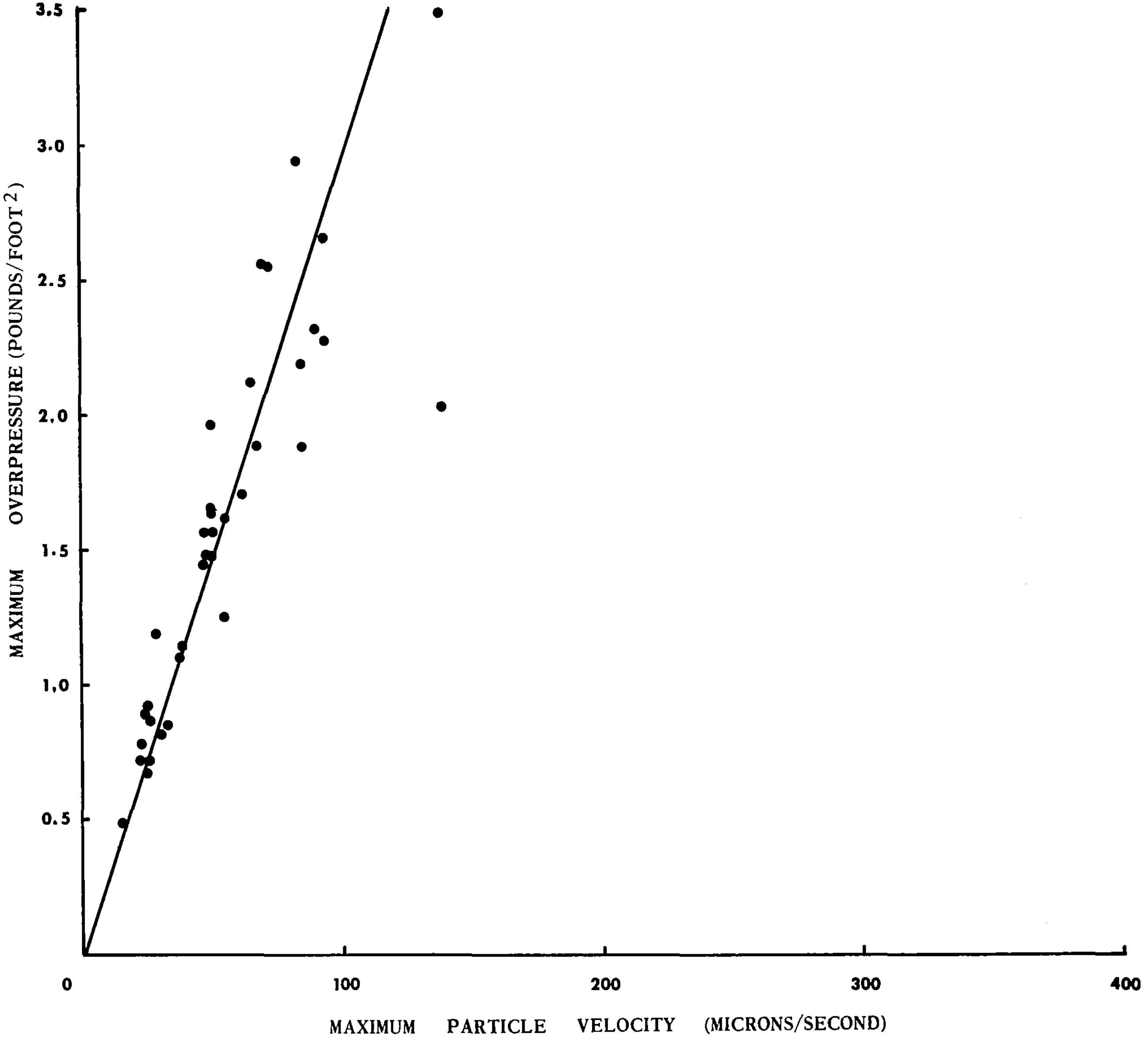

Figure 37. Relation of maximum overpressure for F-104 overflights to peak particle velocity observed on a seismograph oriented transverse to the flight track and located on a clay lake bed (position 1) at Edwards Air Force Base

G 3474

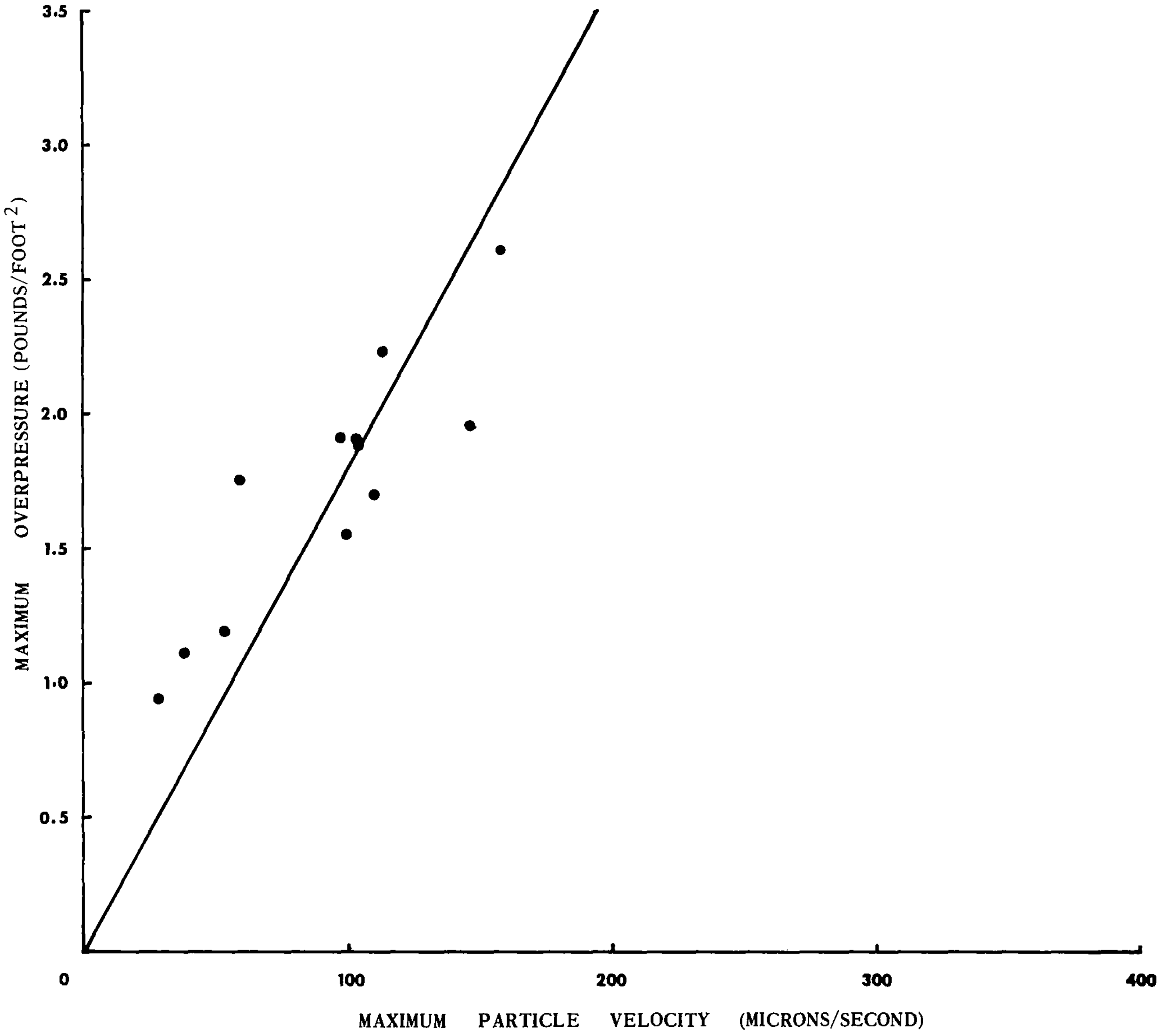

Figure 38. Relation of maximum overpressure for XB-70 overflights to peak particle velocity observed on a seismograph oriented radial to the flight track and located on a clay lake bed (position 1) at Edwards Air Force Base

G 3475

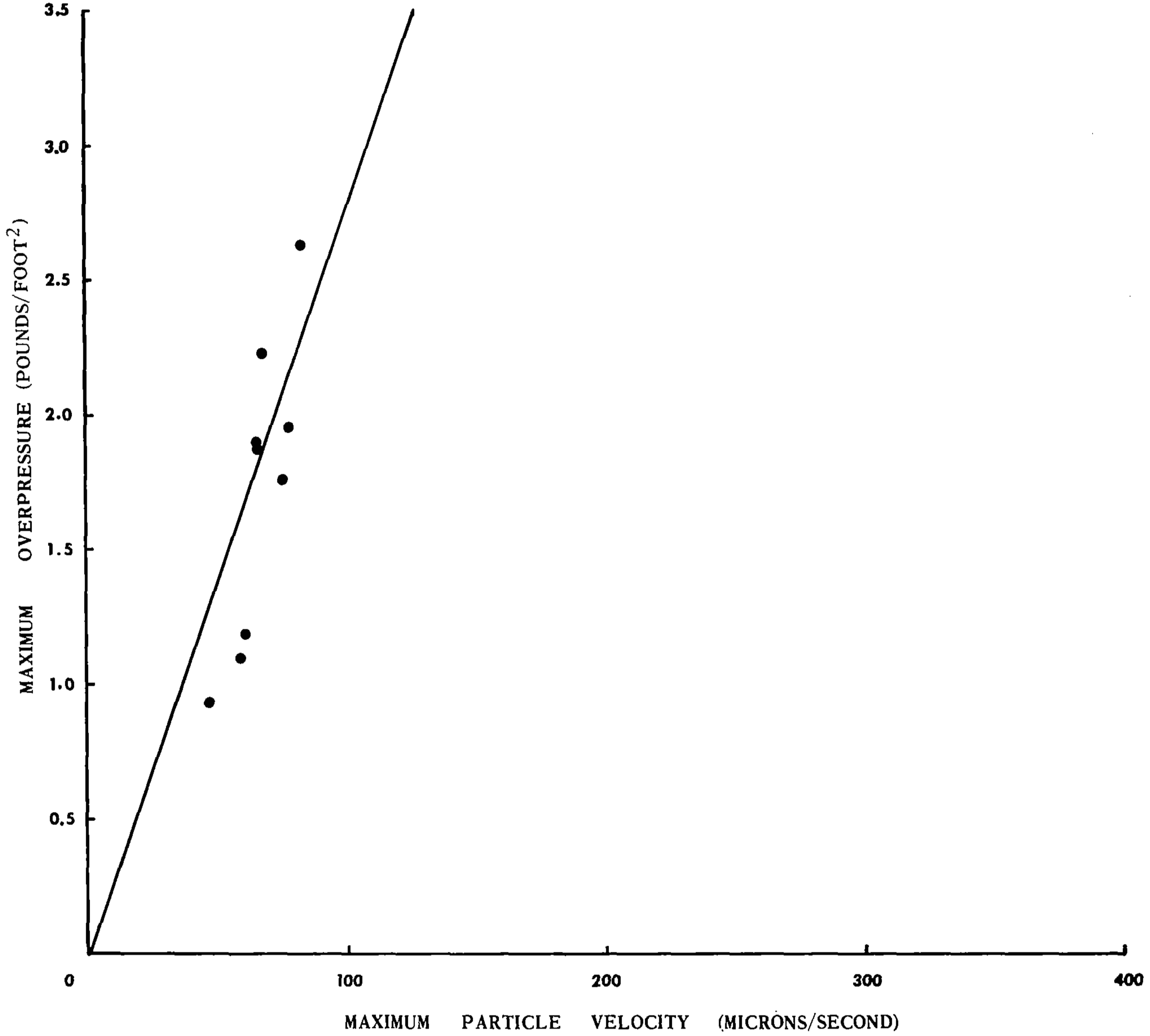

Figure 39. Relation of maximum overpressure for XB-70 overflights to peak particle velocity observed on a seismograph oriented transverse to the flight track and located on a clay lake bed (position 1) at Edwards Air Force Base

G 3476

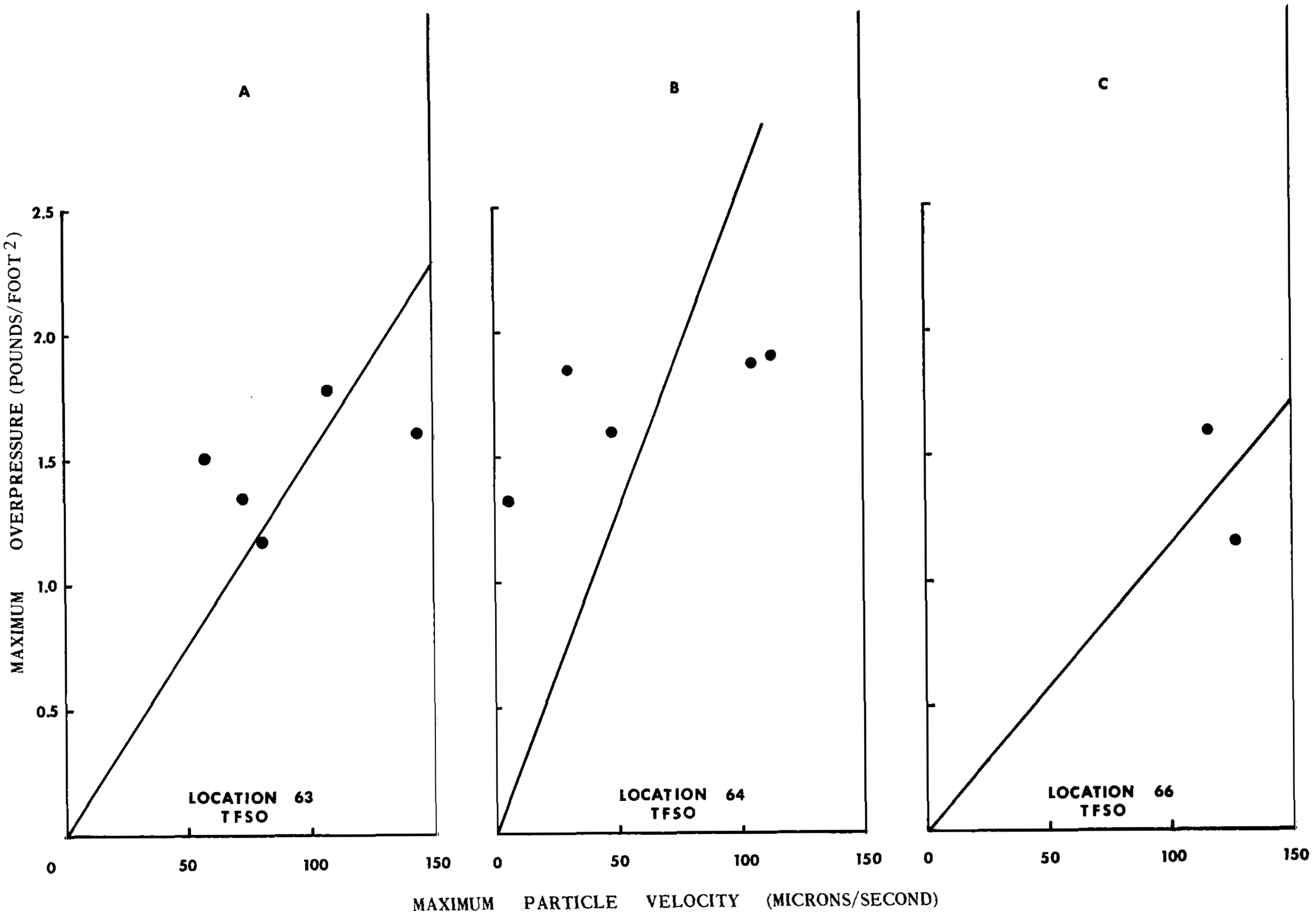

Figure 40. Relation of maximum overpressure for B-58 overflights to peak particle velocity on vertical seismographs at the Tonto Forest Seismological Observatory

G 3477

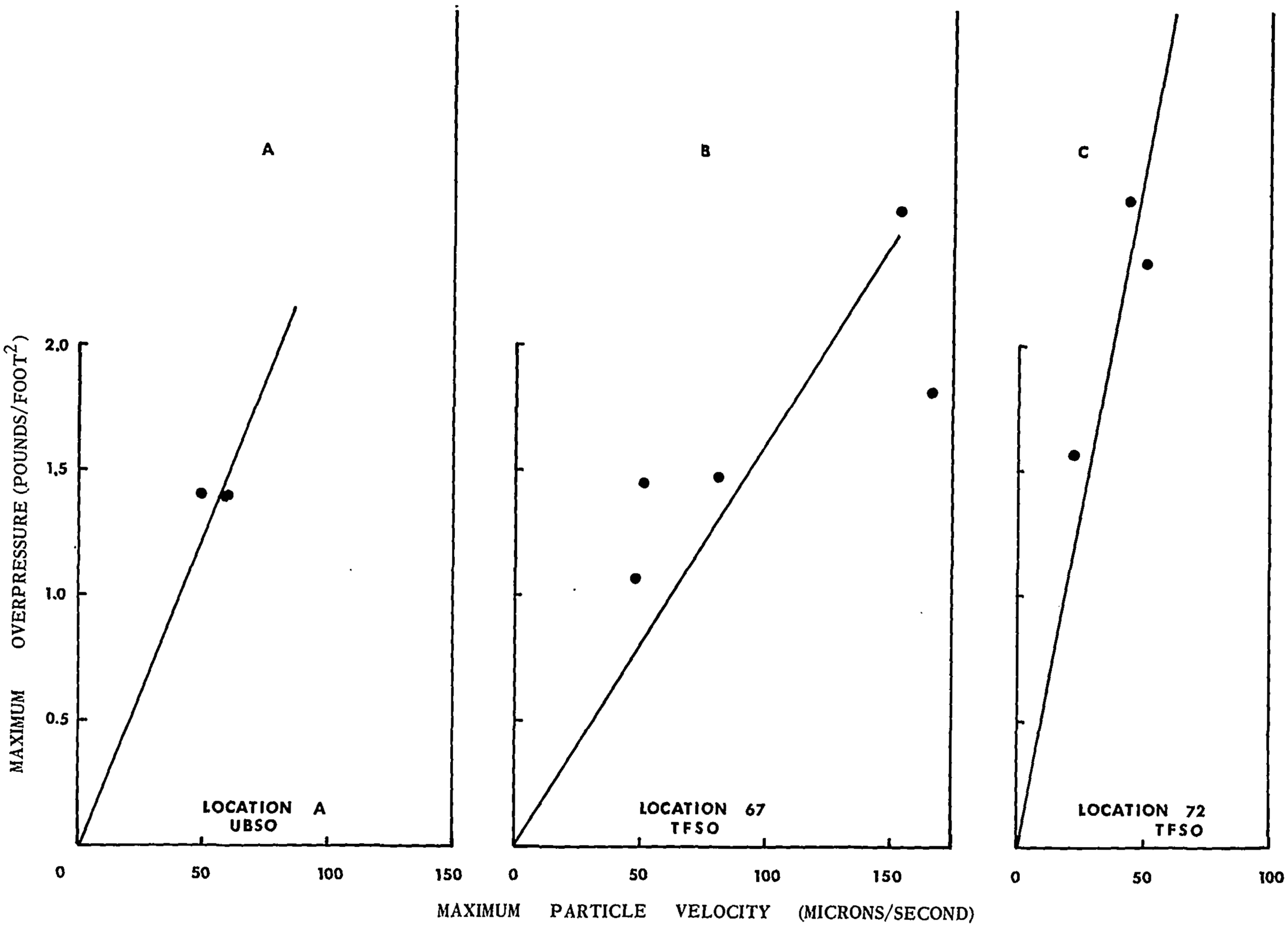

Figure 41. Relation of maximum overpressure for B-58 overflights to peak particle velocity on vertical seismographs at the Tonto Forest Seismological Observatory and the Uinta Basin Seismological Observatory

G 3478

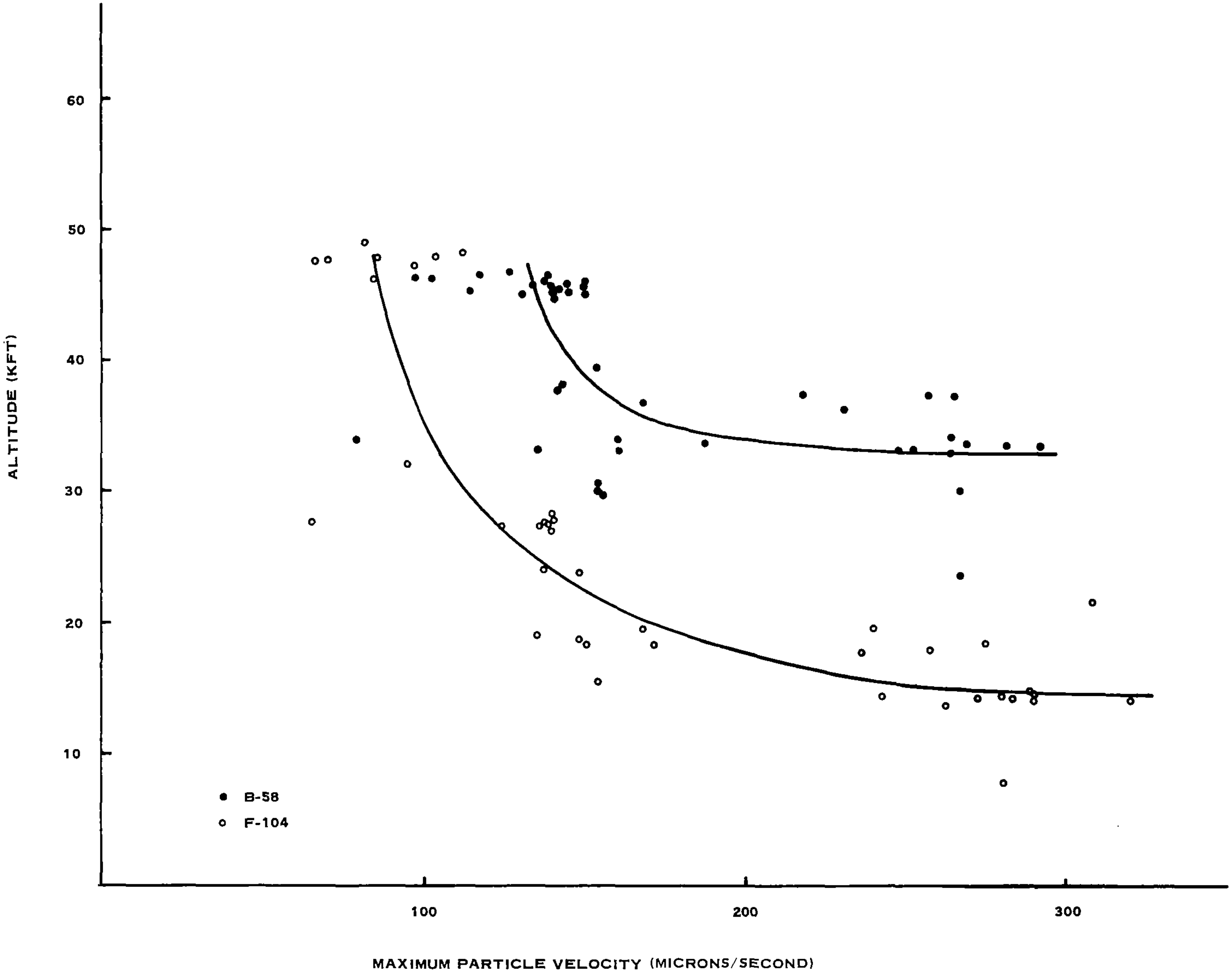

Figure 42. Relation of altitude to peak particle velocity for the B-58 and F-104 for supersonic overflights

G 3479

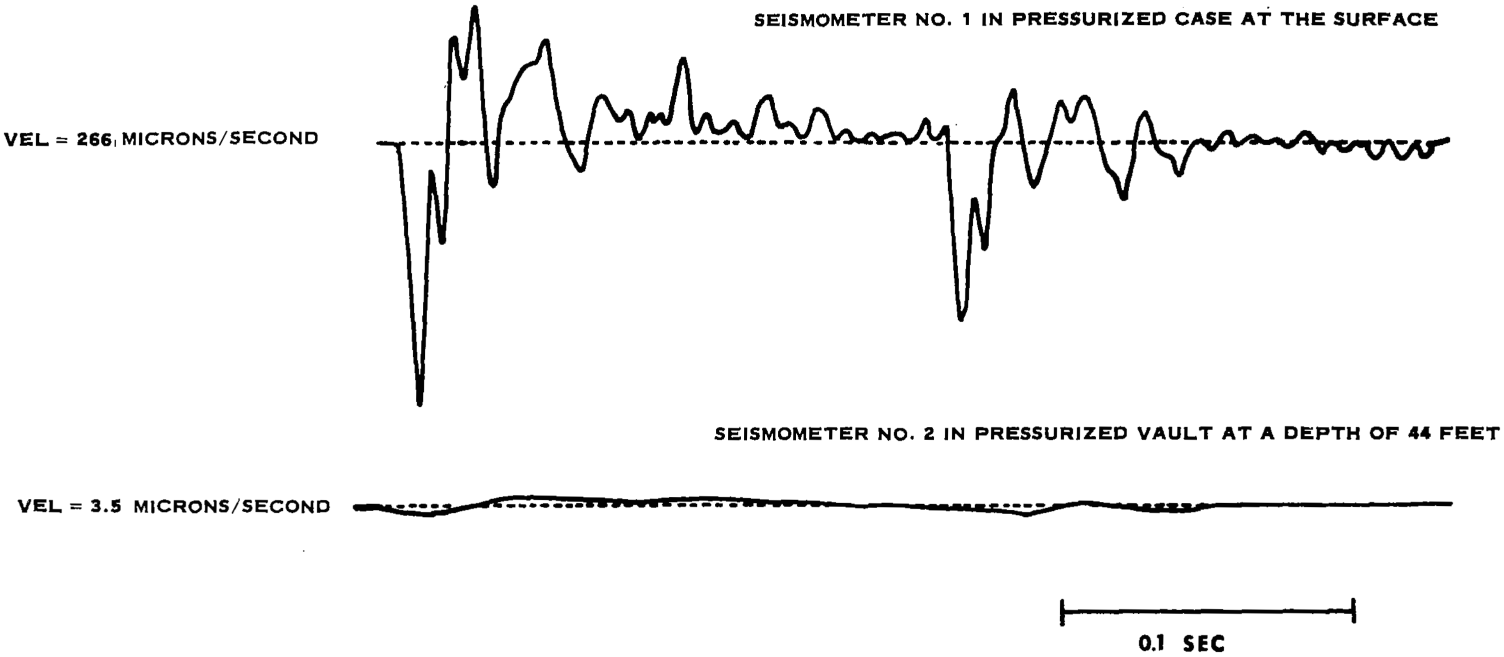

Figure 43. Seismograms showing the attenuation with depth of the ground particle velocity

G 3480

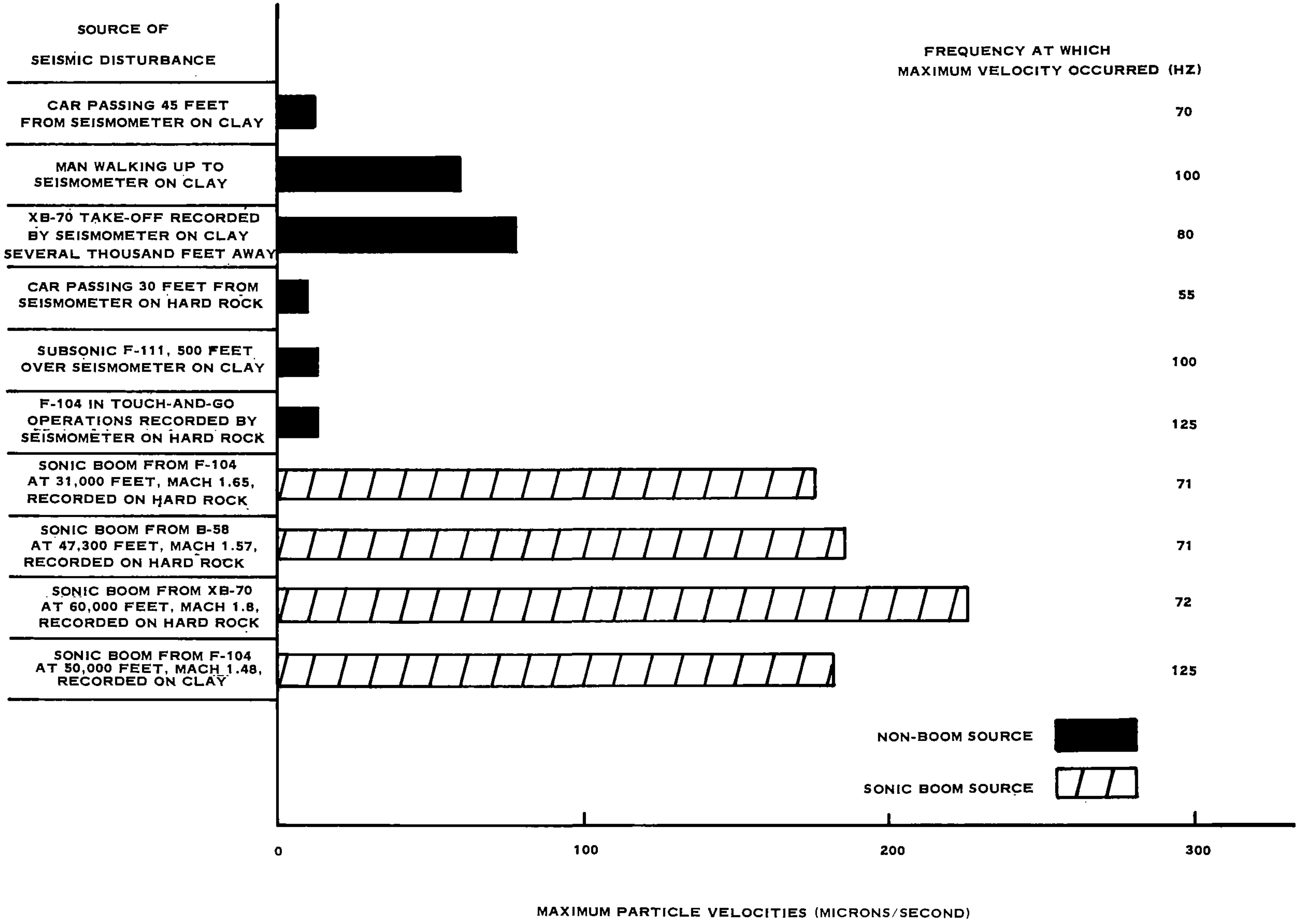

Figure 44. Maximum particle velocities and associated frequencies of various types of cultural noise and selected sonic booms

G 3482

Figure 45. Three-component seismograms recorded for a man walking near seismometers located on the clay lake bed (position 1) at Edwards Air Force Base

G 3482

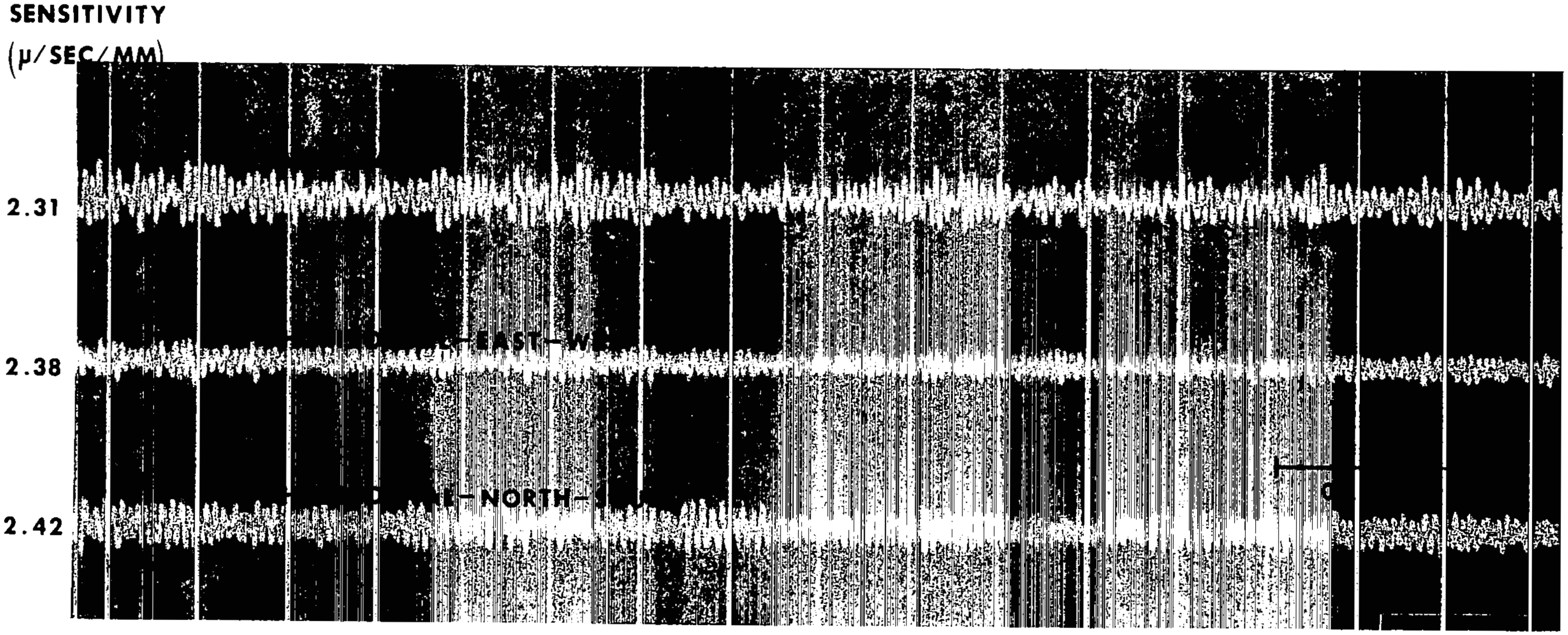

Figure 46. Three-component seismograms recorded for the take-off of an F-104 aircraft two miles from seismometers on the clay lake bed (position 1) at Edwards Air Force Base

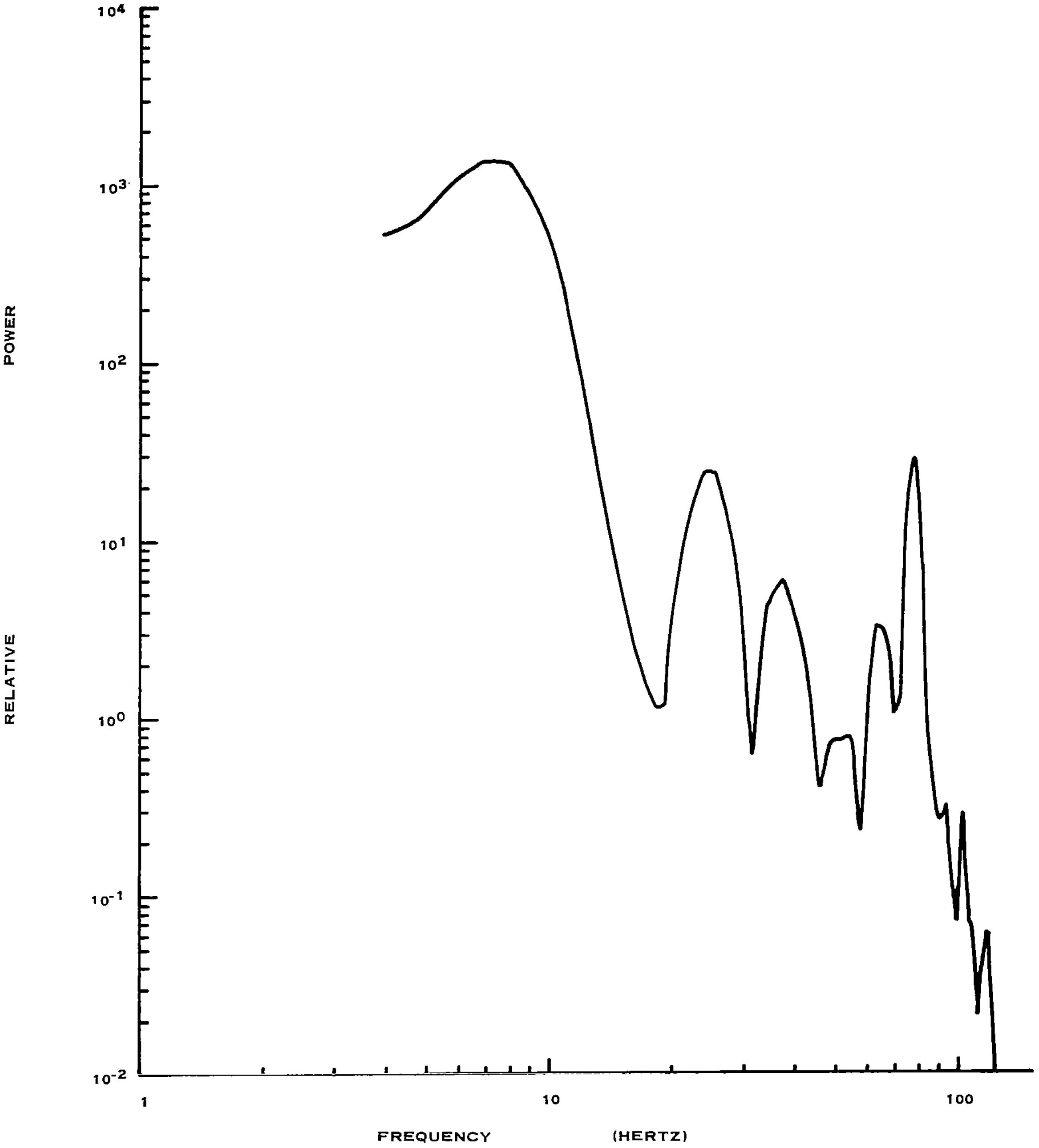

Figure 47. Power spectrum of a seismogram recorded at position 4 on the lake bed at Edwards Air Force Base. The source of the disturbance was an F-104 flying at 20,000 feet and Mach 1.4

G 3484

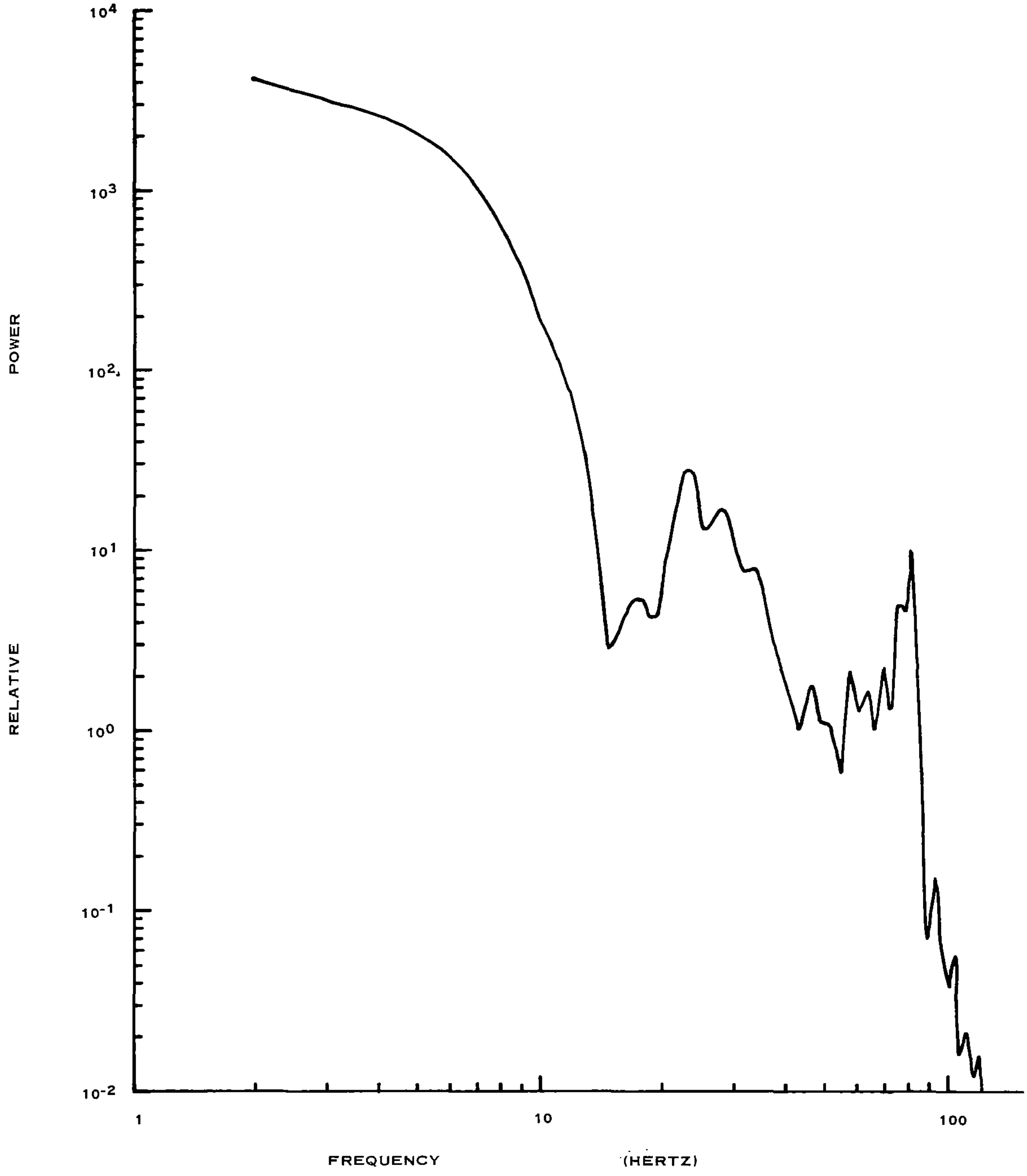

Figure 48. Power spectrum of a seismogram recorded at position 4 on the lake bed at Edwards Air Force Base. The source of disturbance was a B-58 flying at 40,000 feet at Mach 1.65

G 3485

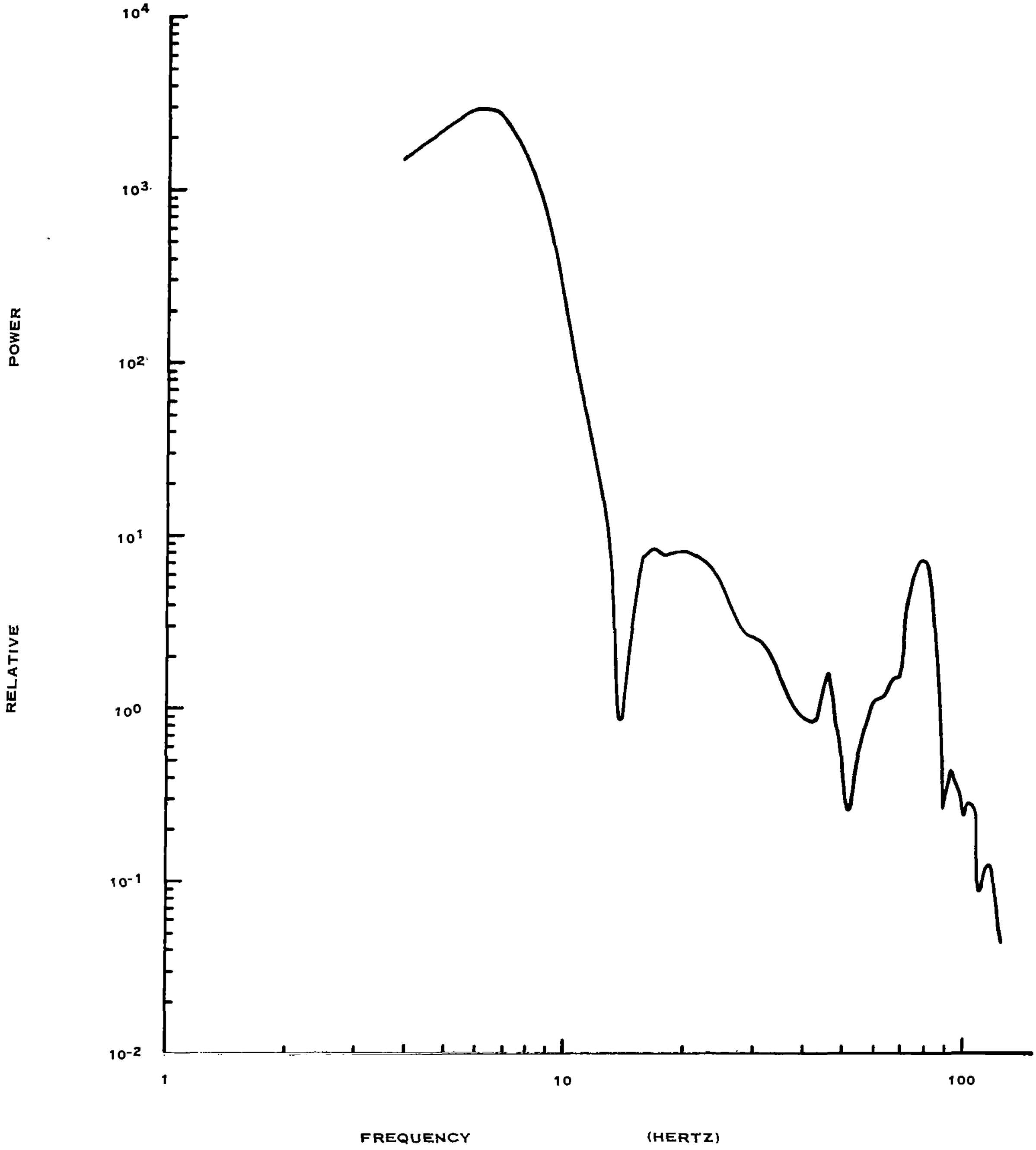

Figure 49. Power spectrum of a seismogram recorded at position 4 on the lake bed at Edwards Air Force Base. The source of the disturbance was an XB-70 flying at 60,000 feet at Mach 1.8

G 3486

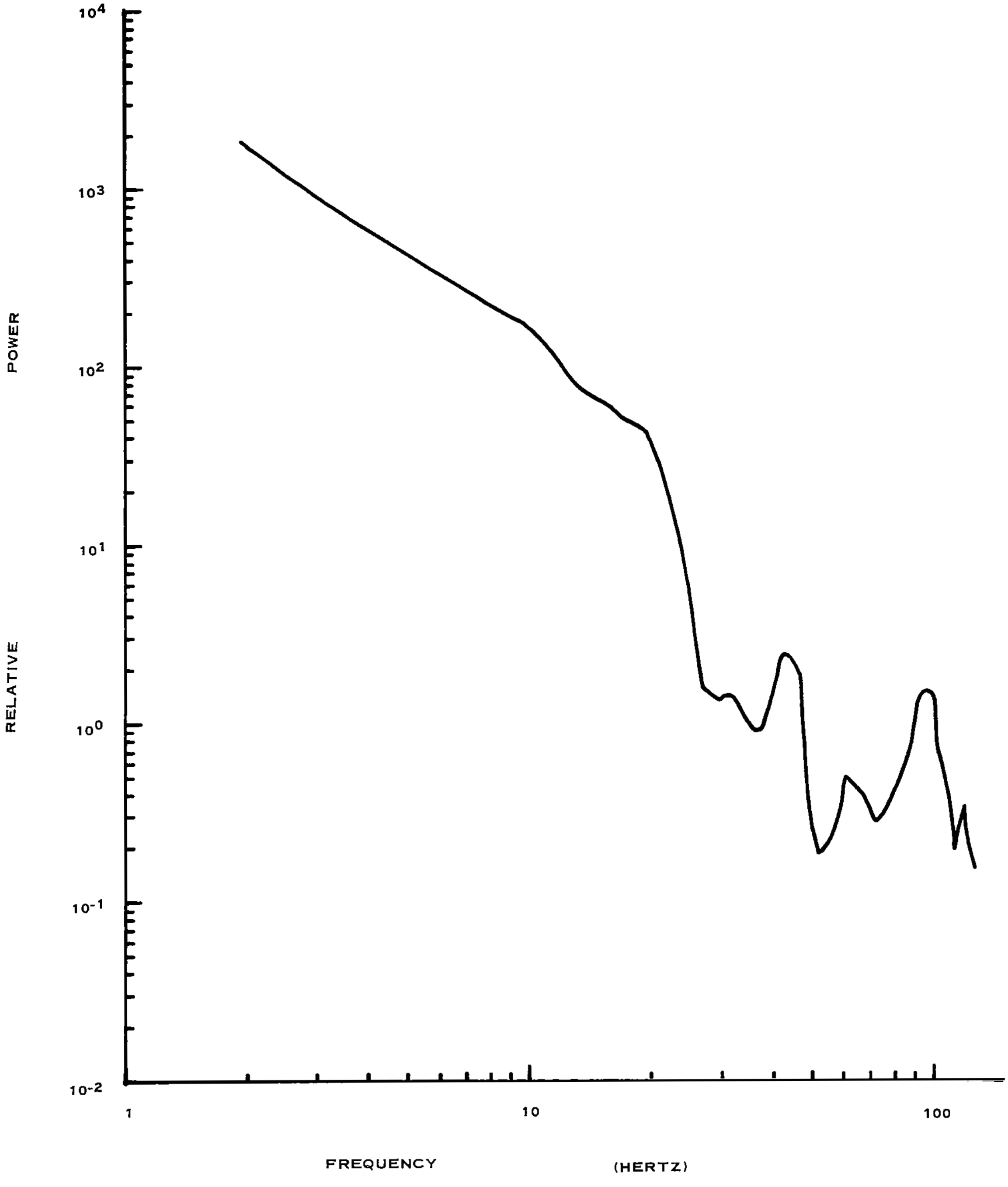

Figure 50. Power spectrum of a seismogram recorded at position 1 on the lake bed at Edwards Air Force Base. The source of the disturbance was an XB-70 flying at 60,000 feet at Mach 1.8

G 3487

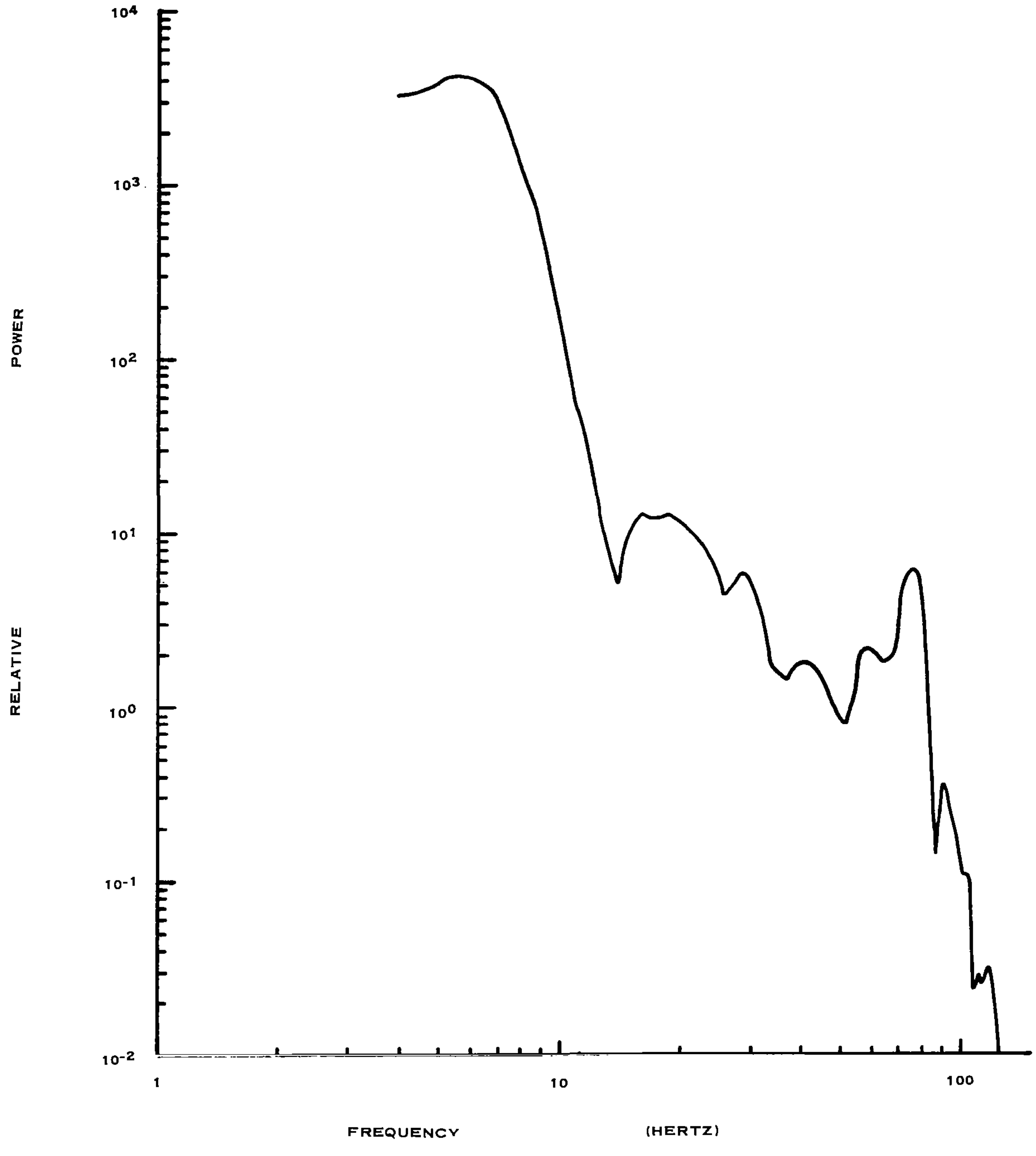

Figure 51. Power spectrum of a seismogram recorded at position 4 on the lake bed at Edwards Air Force Base. The source of the disturbance was an XB-70 flying at 60,000 feet and Mach 1.8

G 3488

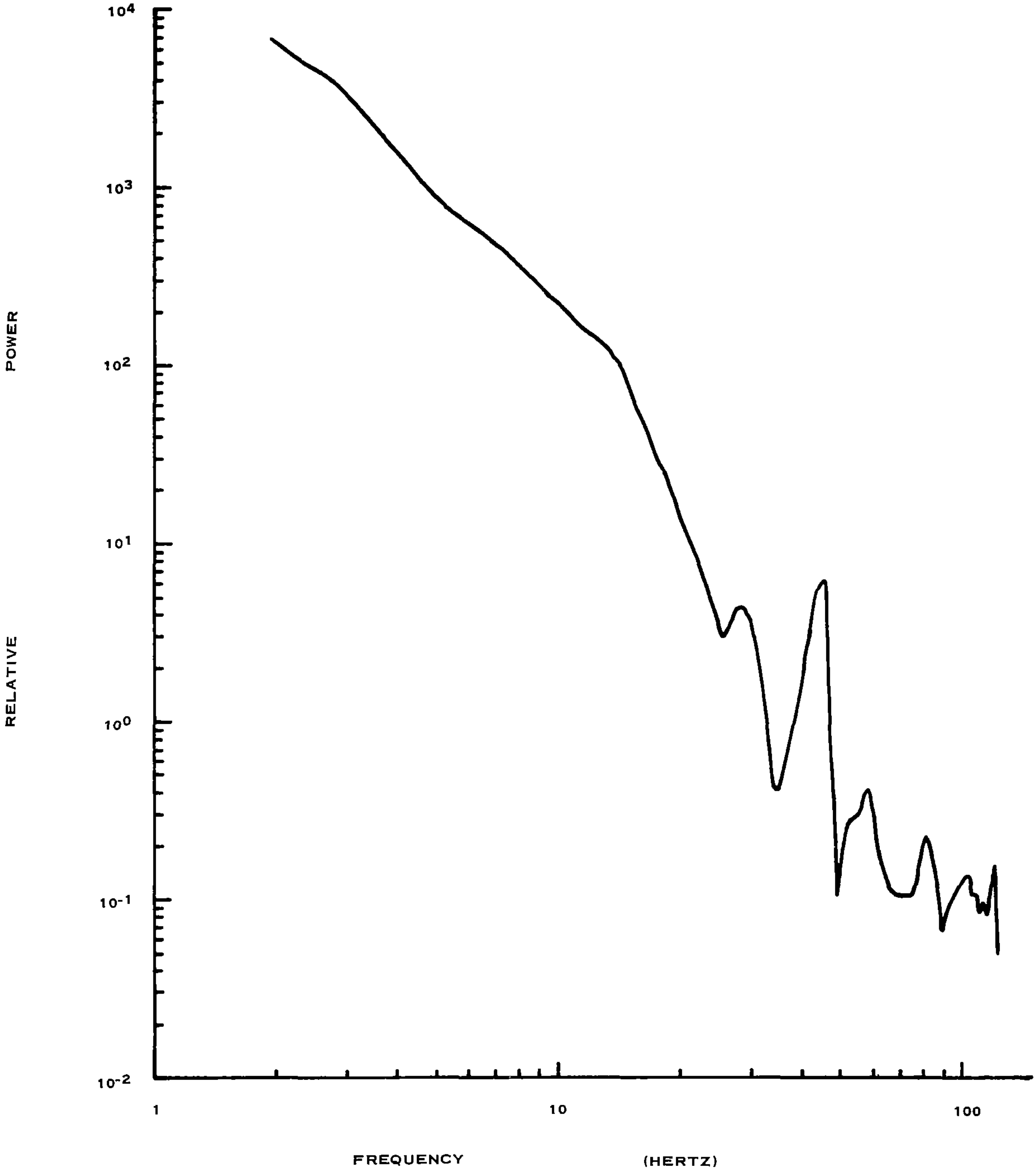

Figure 52. Power spectrum of a seismogram recorded at position 5 at Edwards Air Force Base. The source of the disturbance was an XB-70 flying at 60,000 feet and Mach 1.8

G 3489

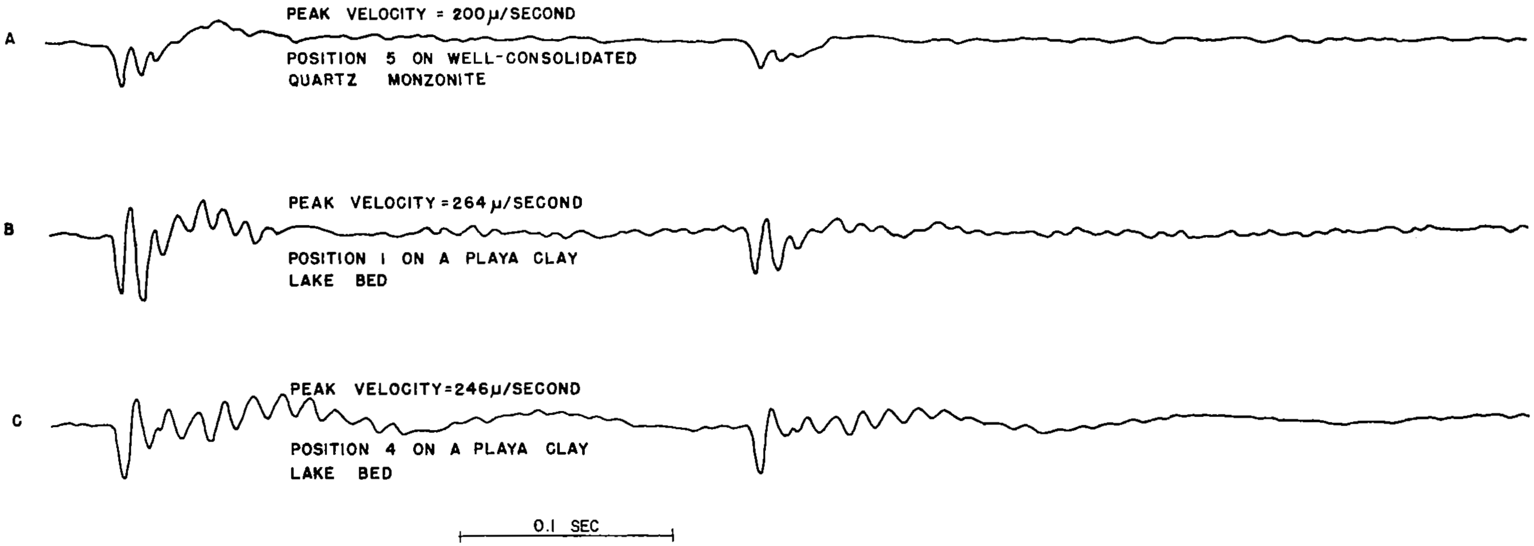

Figure 53. Sonic boom seismic signatures for mission 13-2 (XB-70) recorded at three different positions at Edwards Air Force Base

G 3490

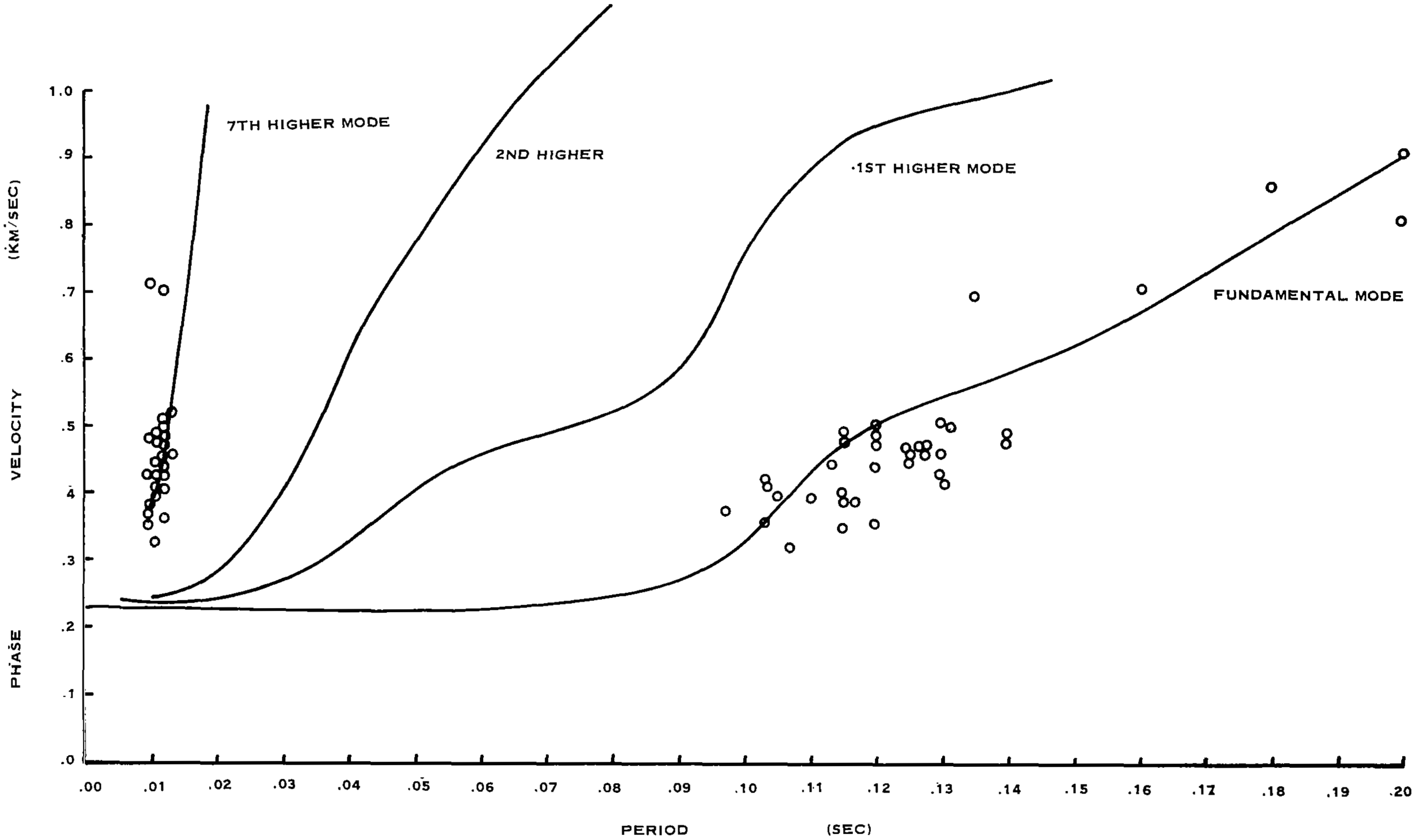

Figure 54. Theoretical Rayleigh wave dispersion curves for the dry lake area at Edwards Air Force Base and the empirical relationship between aircraft velocity and the dominant periods observed on the seismograms

G 3491

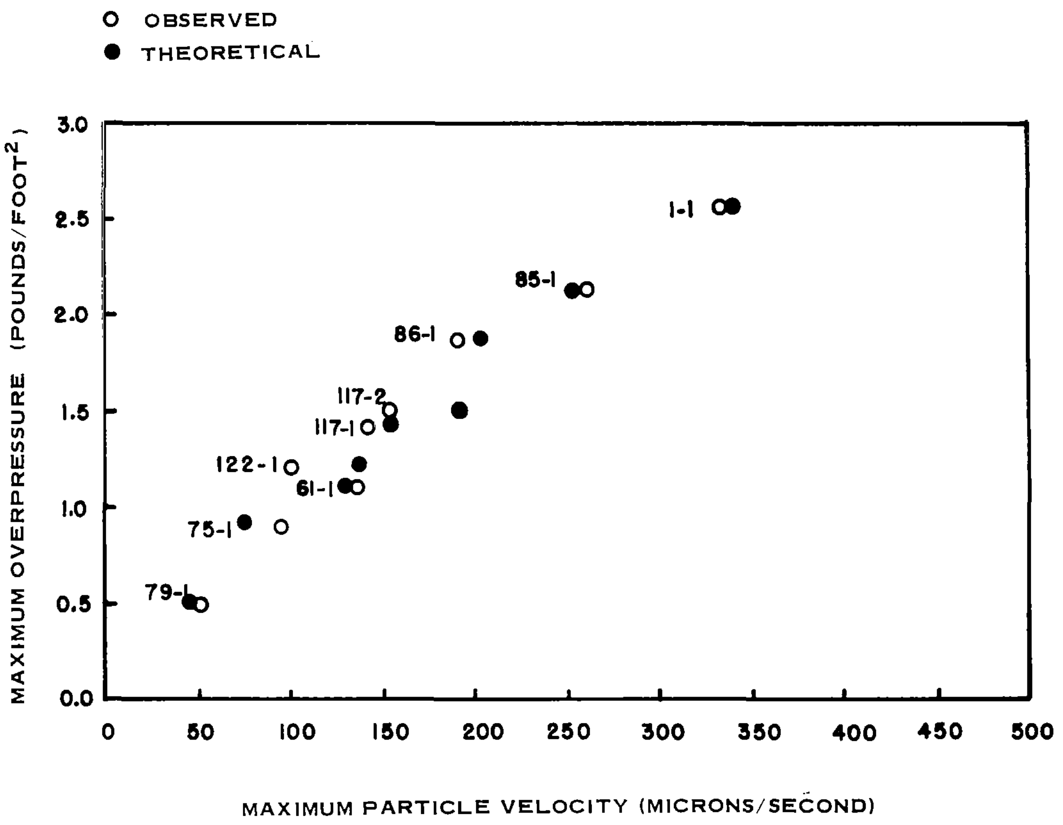

Figure 55. Comparison of maximum particle velocities observed and theoretically predicted for the lake bed at Edwards Air Force Base, as a function of maximum overpressure

G 3492

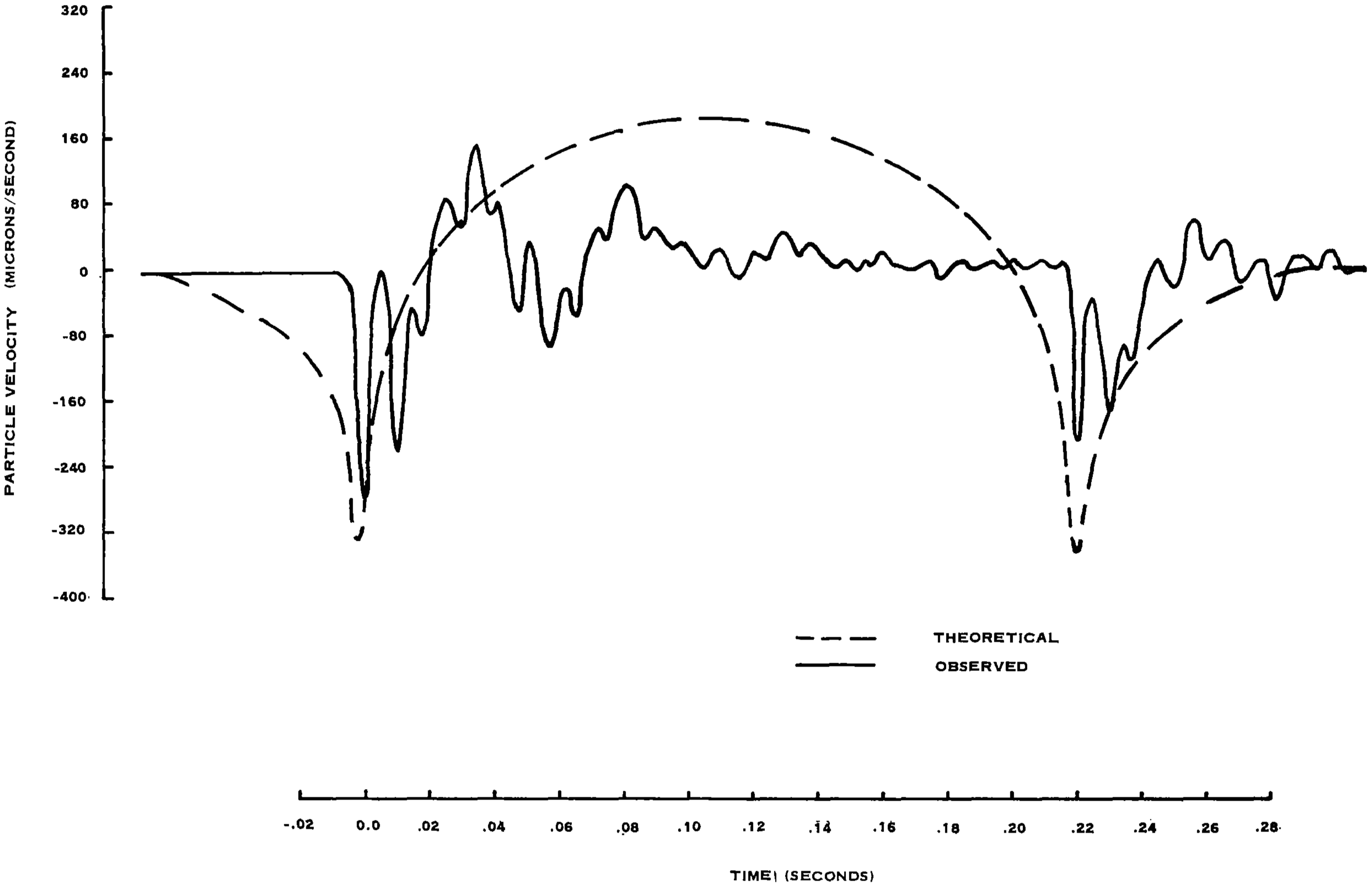

Figure 56. Comparison of the theoretical and the recorded seismograms on the lake bed at Edwards Air Force Base for mission 1-1

G 3493

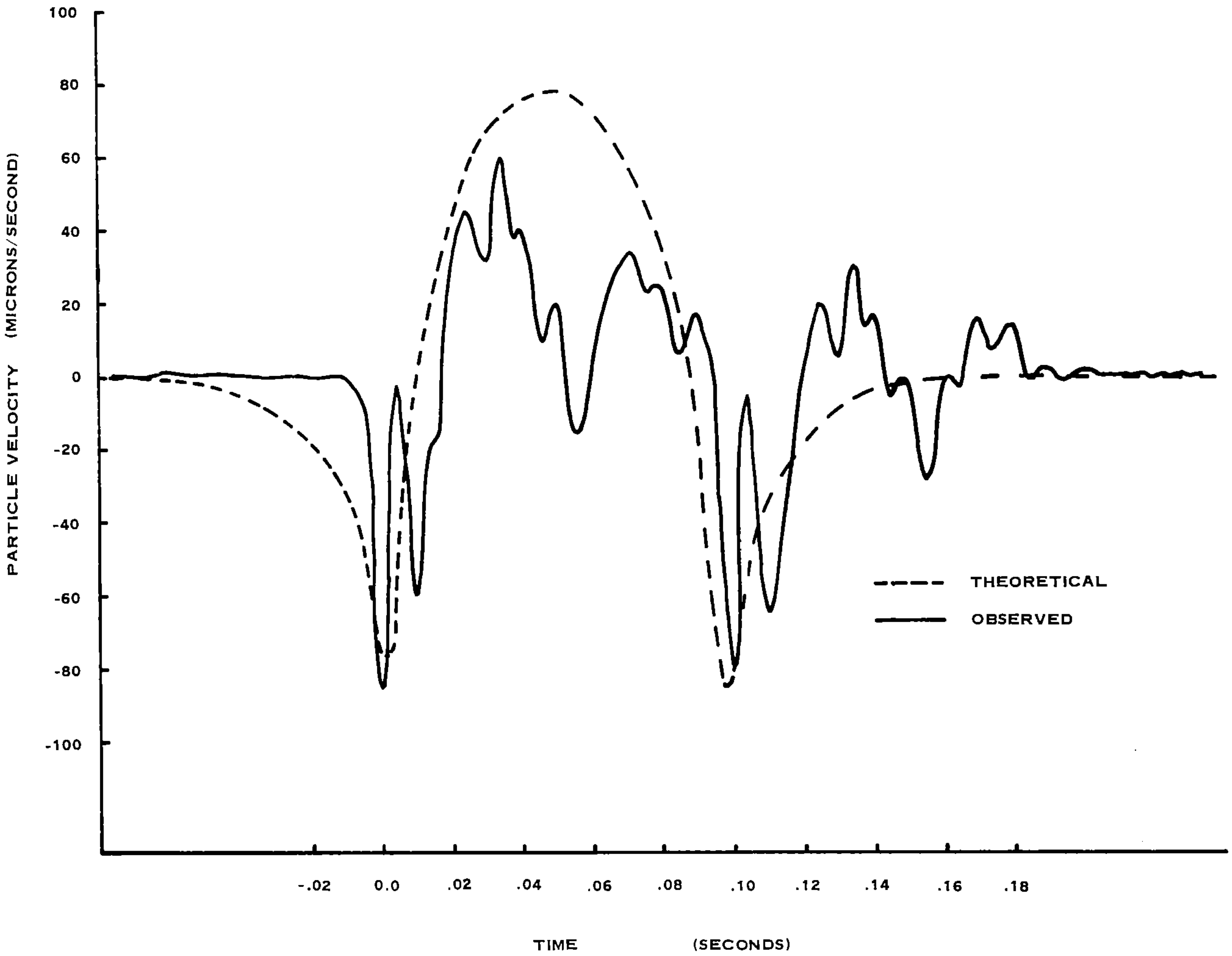

Figure 57. Comparison of the theoretical and the recorded seismograms on the lake bed at Edwards Air Force Base for mission 75-1

G 3494

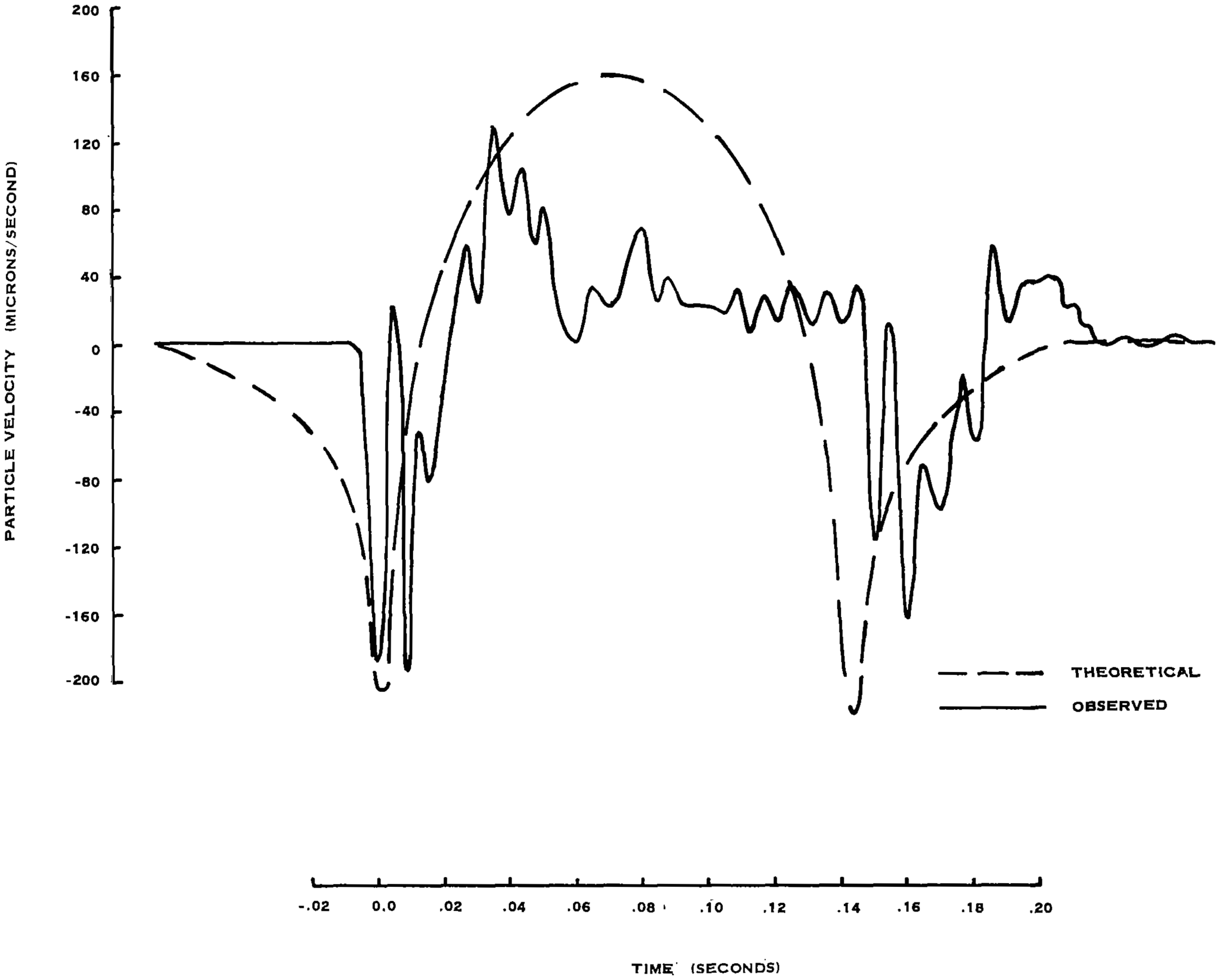

Figure 58. Comparison of the theoretical and the recorded seismograms on the lake bed at Edwards Air Force Base for mission 86-1

G 3495

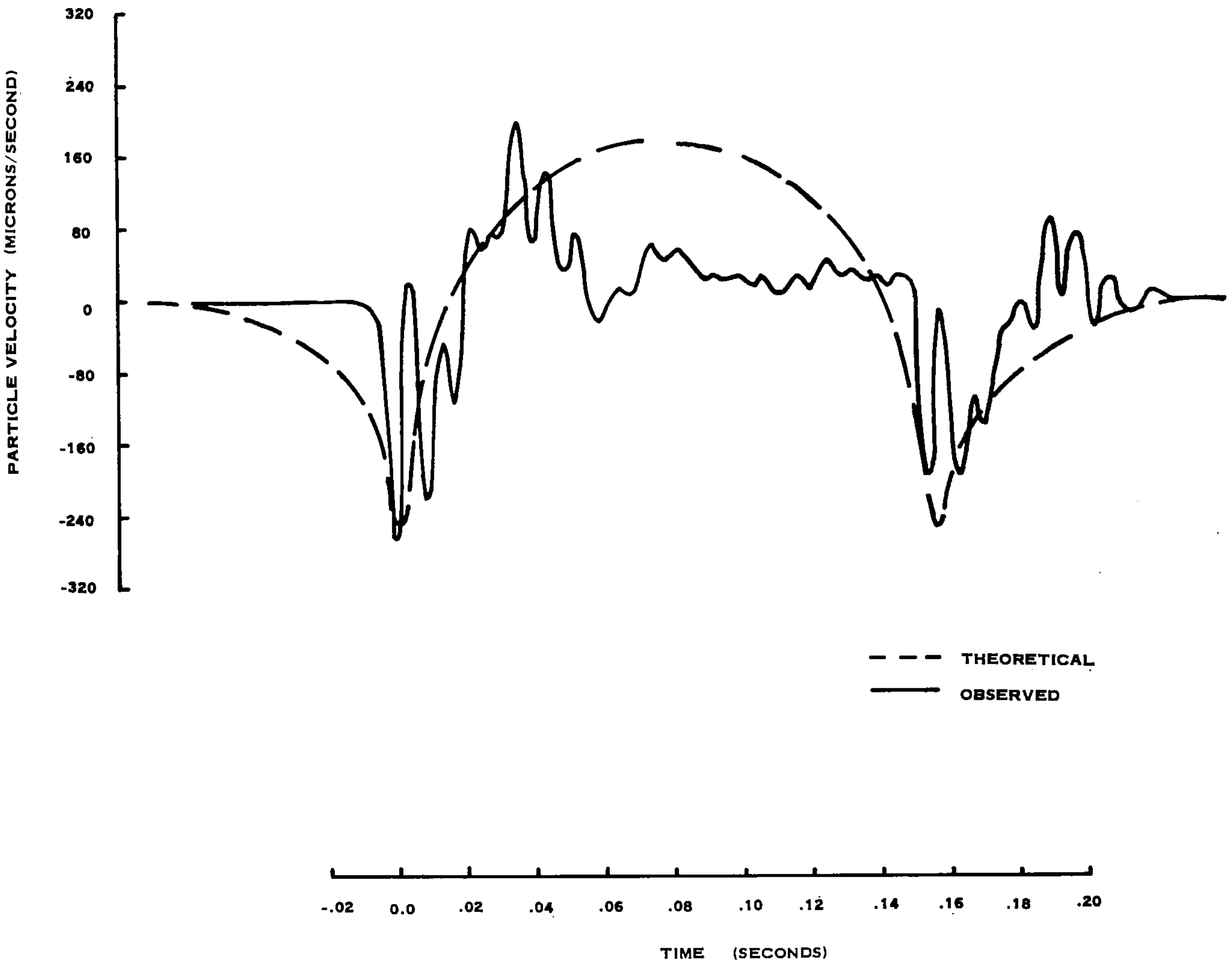

Figure 59. Comparison of the theoretical and the recorded seismogram on the lake bed at Edwards Air Force Base for mission 85-1

G 3496

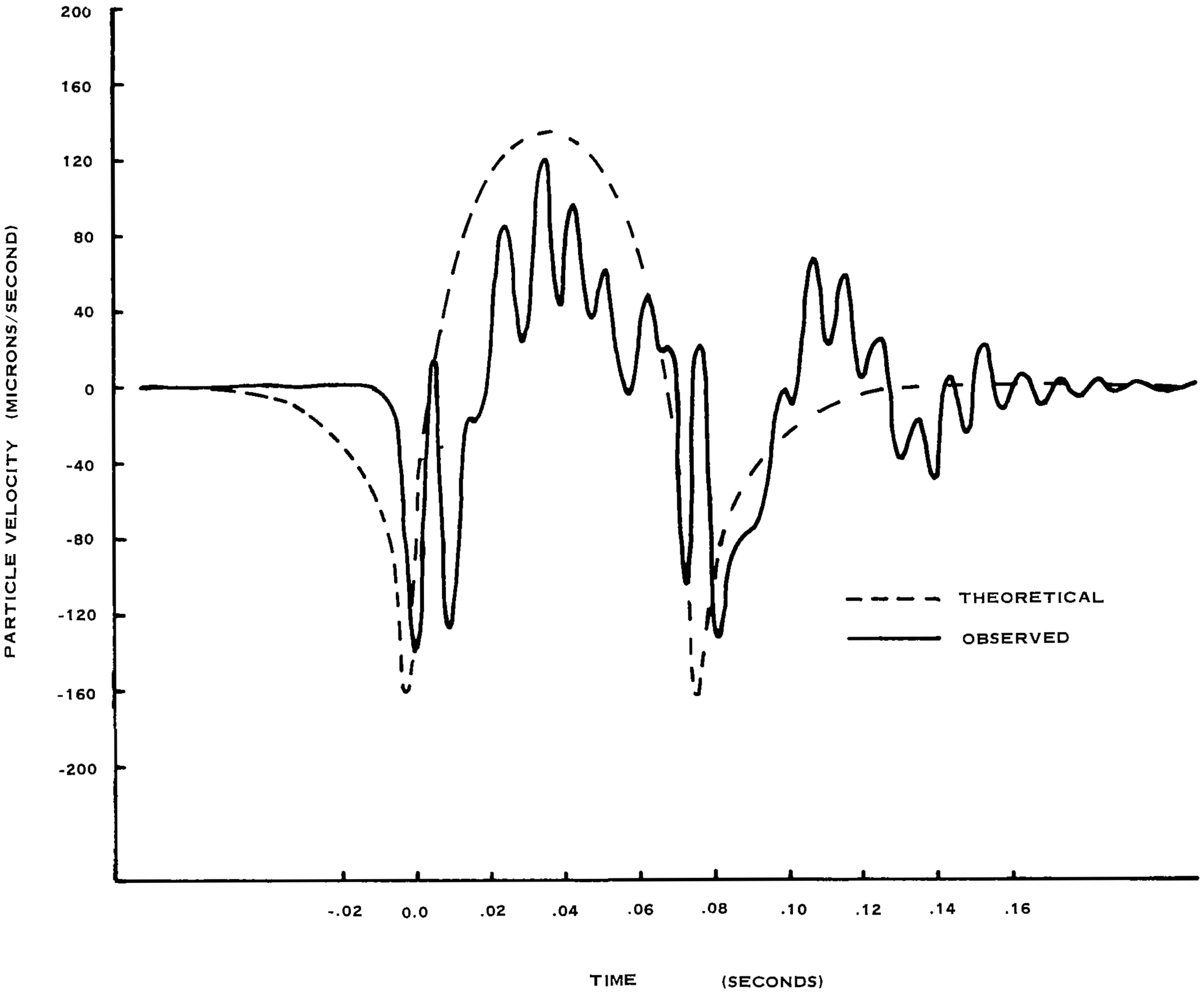

Figure 60. Comparison of the theoretical and the recorded seismogram on the lake bed at Edwards Air Force Base for mission 117-1

G 3497

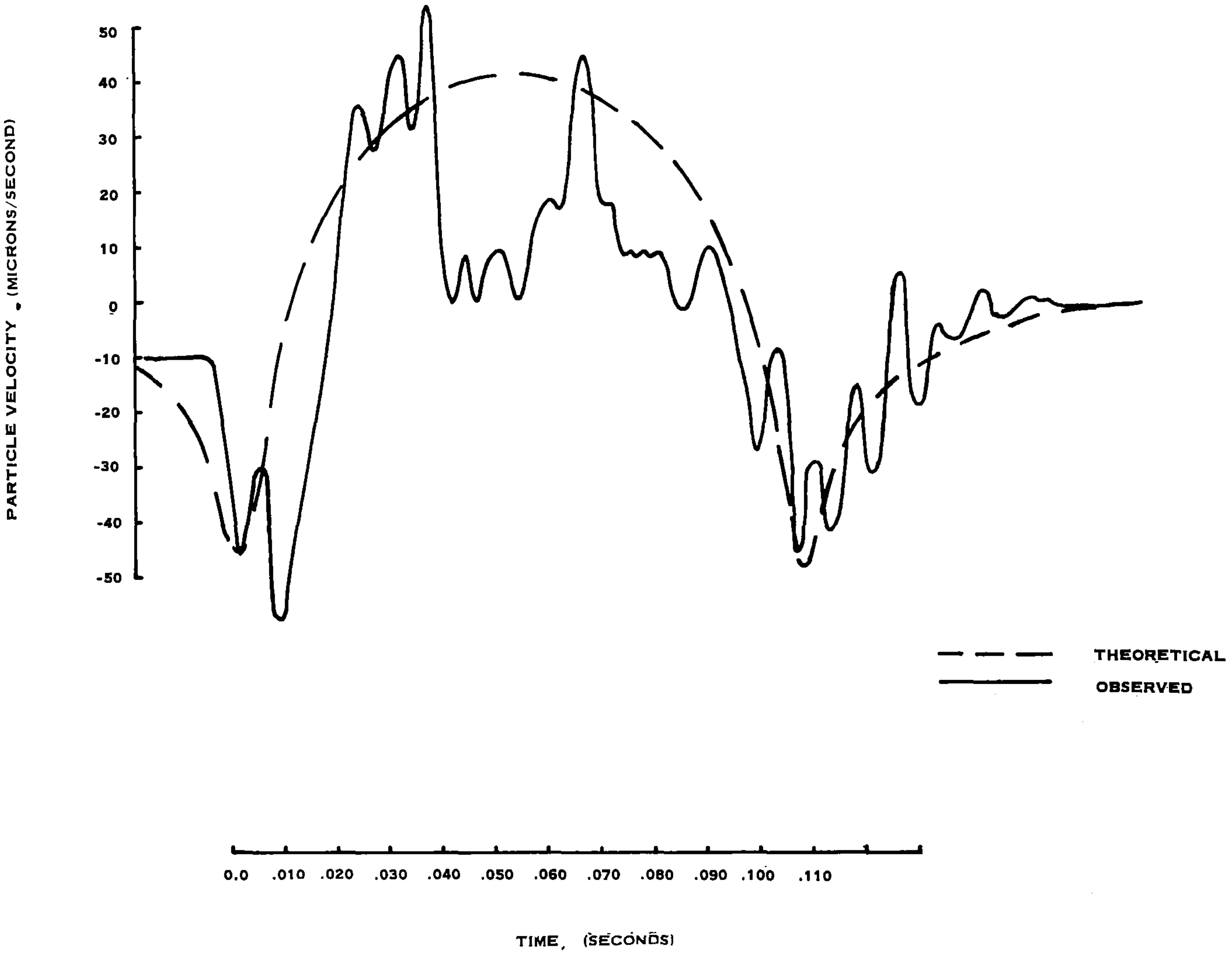

Figure 61. Comparison of the theoretical and the recorded seismogram on the lake bed at Edwards Air Force Base for mission 79-1

G 3498

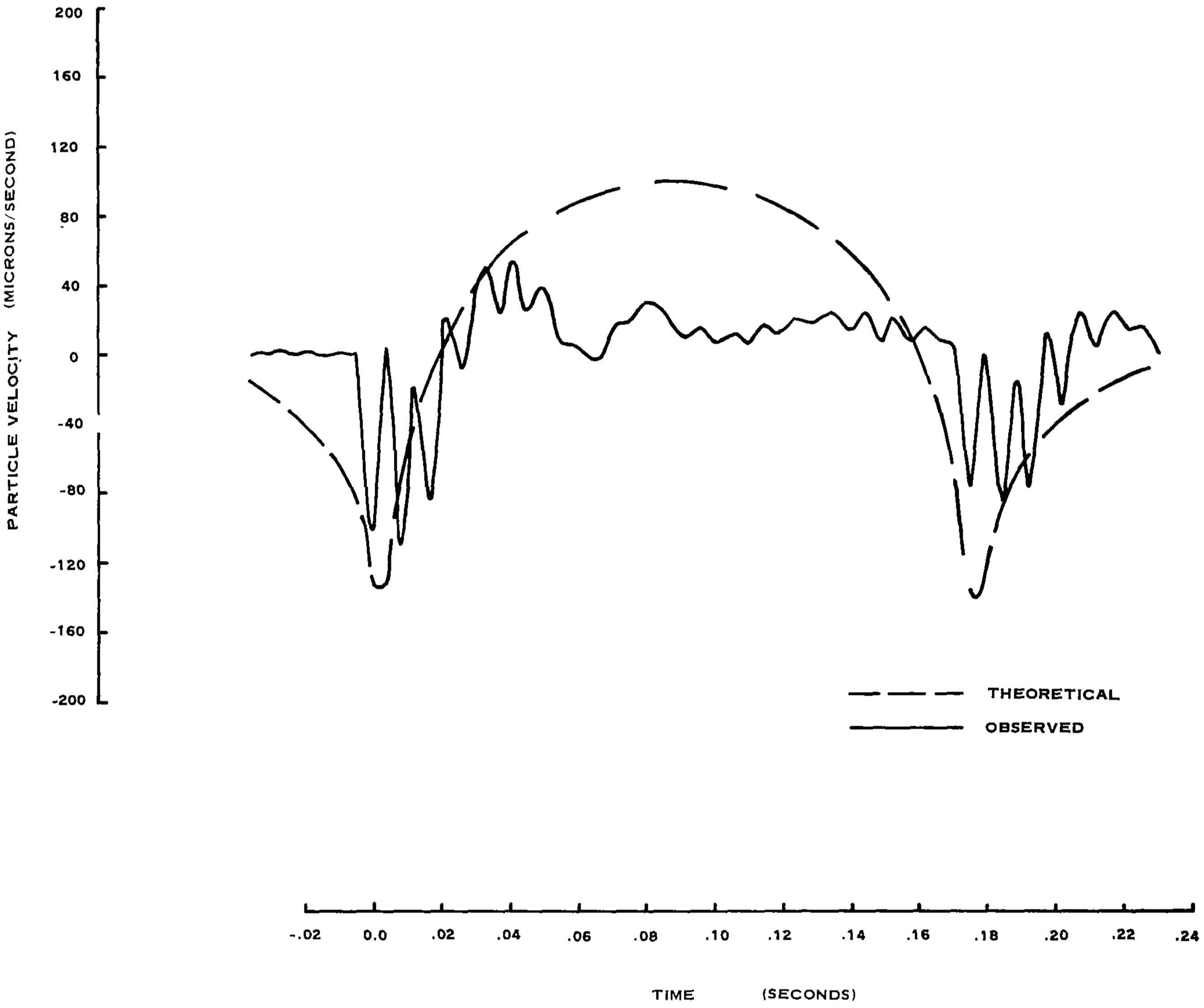

Figure 62. Comparison of the theoretical and the recorded seismogram on the lake bed at Edwards Air Force Base for mission 122-1

G 3499

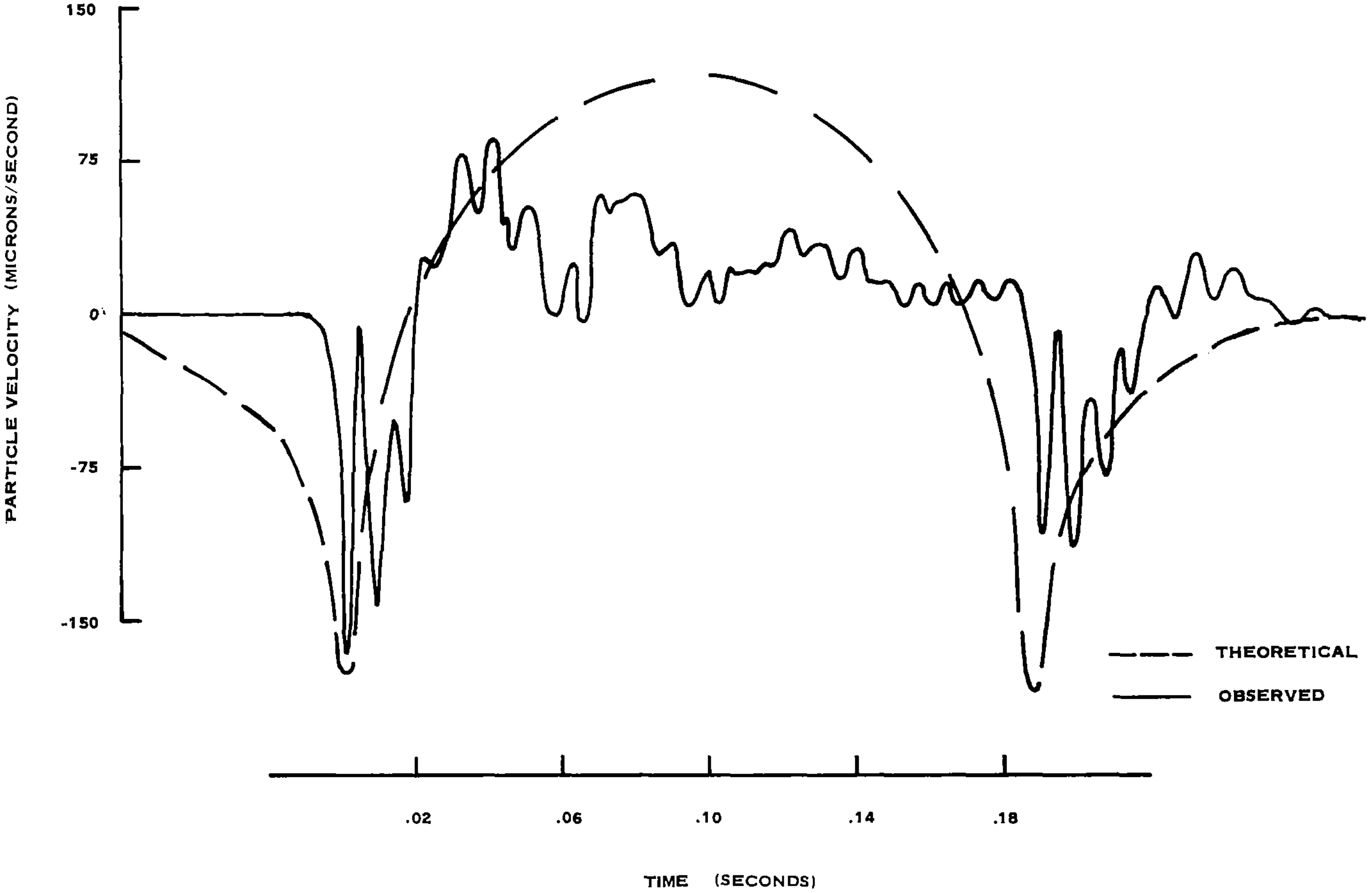

Figure 63. Comparison of the theoretical and the recorded seismogram on the lake bed at Edwards Air Force Base for mission 117-2

G 3500

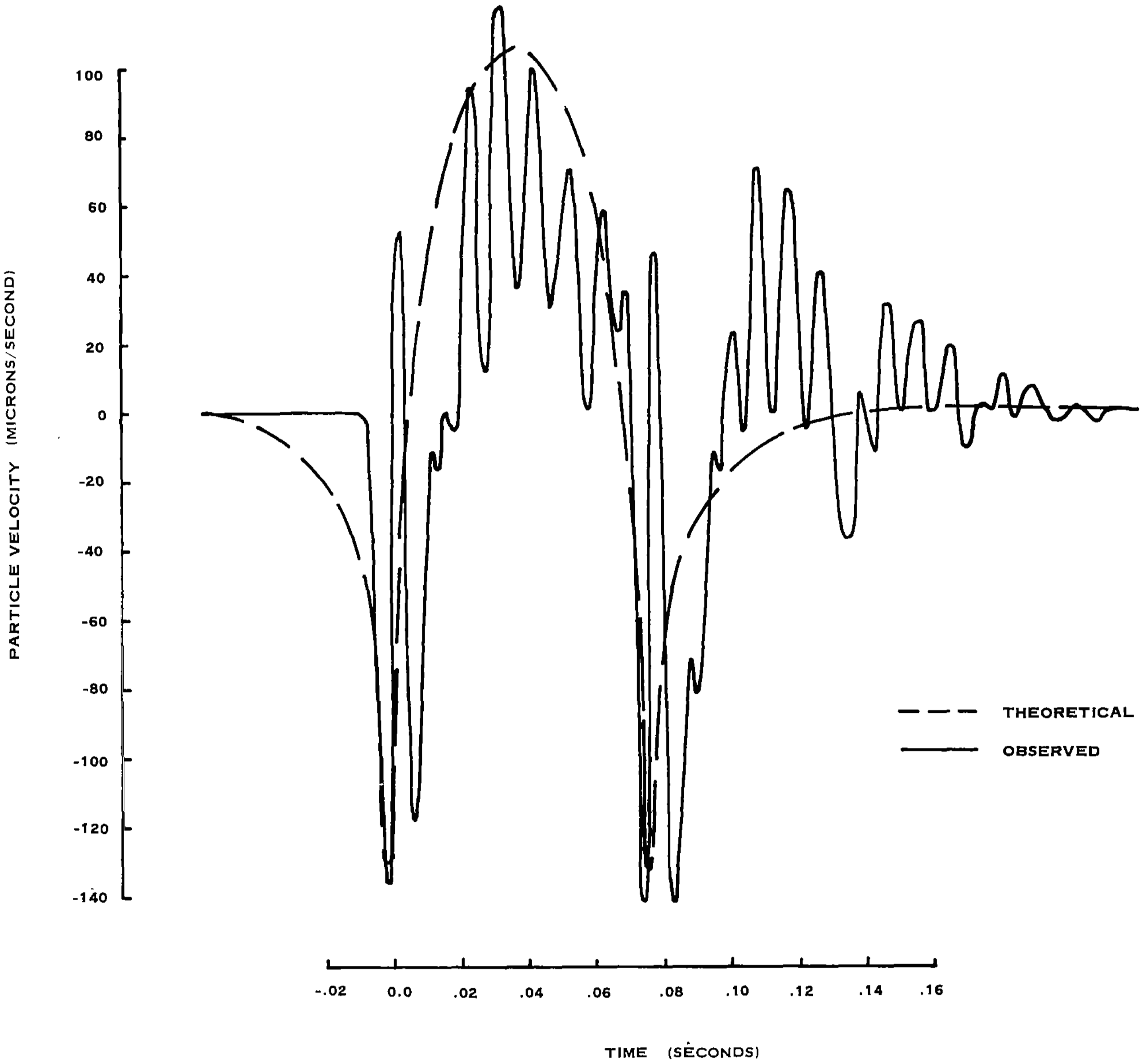

Figure 64. Comparison of the theoretical and the recorded seismogram on the lake bed at Edwards Air Force Base for mission 61-1

G 3501

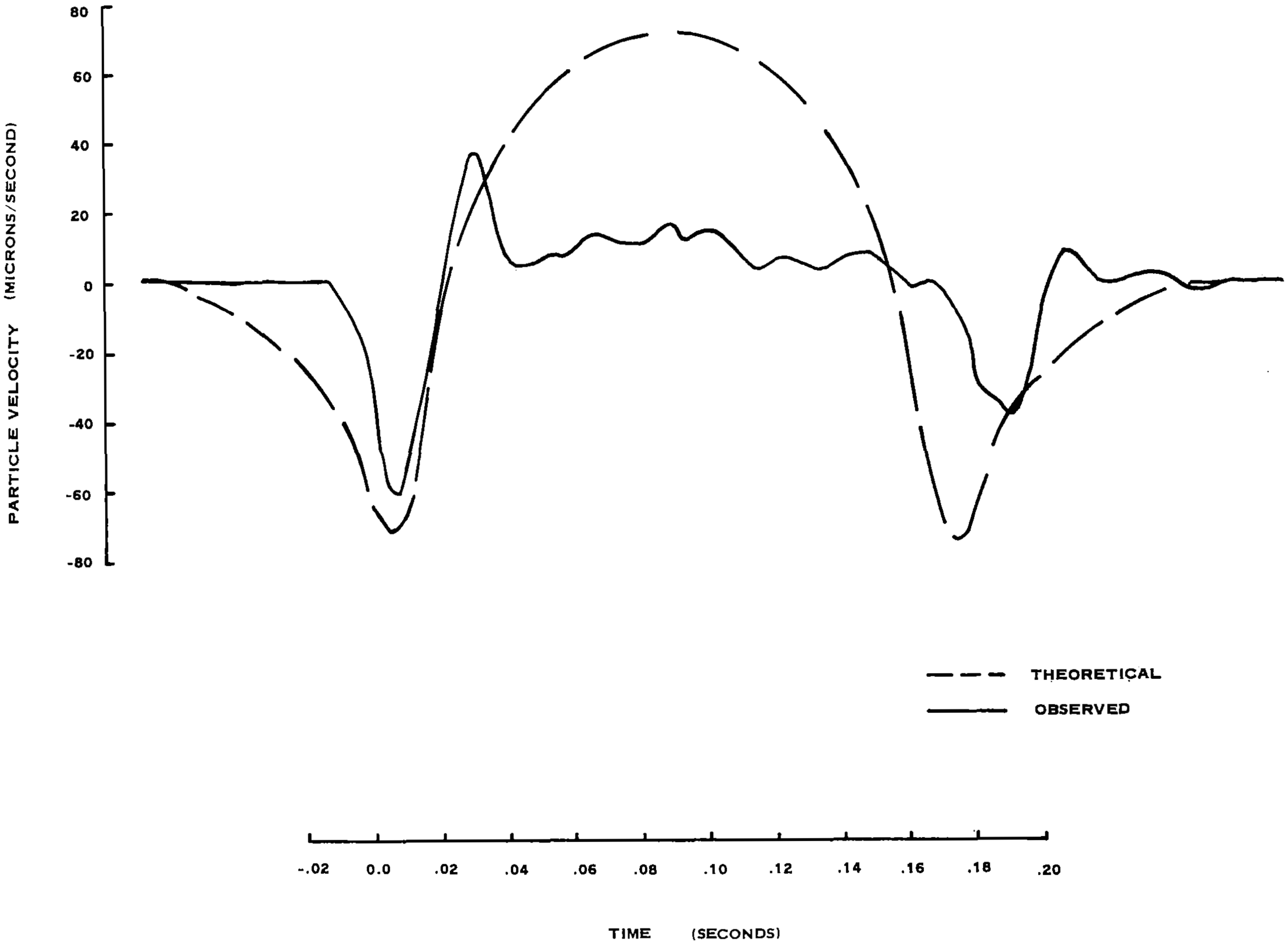

Figure 65. Comparison of the theoretical and the recorded seismogram at position 67 at the Tonto Forest Seismological Observatory for mission Tonto 2

G 3502

NASA-Langley, 1968 — 13 CR-1137